



## **Terms and Conditions of Use of Digitised Theses from Trinity College Library Dublin**

### **Copyright statement**

All material supplied by Trinity College Library is protected by copyright (under the Copyright and Related Rights Act, 2000 as amended) and other relevant Intellectual Property Rights. By accessing and using a Digitised Thesis from Trinity College Library you acknowledge that all Intellectual Property Rights in any Works supplied are the sole and exclusive property of the copyright and/or other IPR holder. Specific copyright holders may not be explicitly identified. Use of materials from other sources within a thesis should not be construed as a claim over them.

A non-exclusive, non-transferable licence is hereby granted to those using or reproducing, in whole or in part, the material for valid purposes, providing the copyright owners are acknowledged using the normal conventions. Where specific permission to use material is required, this is identified and such permission must be sought from the copyright holder or agency cited.

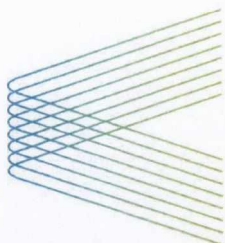
### **Liability statement**

By using a Digitised Thesis, I accept that Trinity College Dublin bears no legal responsibility for the accuracy, legality or comprehensiveness of materials contained within the thesis, and that Trinity College Dublin accepts no liability for indirect, consequential, or incidental, damages or losses arising from use of the thesis for whatever reason. Information located in a thesis may be subject to specific use constraints, details of which may not be explicitly described. It is the responsibility of potential and actual users to be aware of such constraints and to abide by them. By making use of material from a digitised thesis, you accept these copyright and disclaimer provisions. Where it is brought to the attention of Trinity College Library that there may be a breach of copyright or other restraint, it is the policy to withdraw or take down access to a thesis while the issue is being resolved.

### **Access Agreement**

By using a Digitised Thesis from Trinity College Library you are bound by the following Terms & Conditions. Please read them carefully.

I have read and I understand the following statement: All material supplied via a Digitised Thesis from Trinity College Library is protected by copyright and other intellectual property rights, and duplication or sale of all or part of any of a thesis is not permitted, except that material may be duplicated by you for your research use or for educational purposes in electronic or print form providing the copyright owners are acknowledged using the normal conventions. You must obtain permission for any other use. Electronic or print copies may not be offered, whether for sale or otherwise to anyone. This copy has been supplied on the understanding that it is copyright material and that no quotation from the thesis may be published without proper acknowledgement.



CRANN



Fondúireacht Eolaíochta Éireann

Science  
Foundation  
Ireland

Investigation of  $\text{LiMo}_3\text{Se}_3$  nanowires,  
nanowire networks and ion-exchanged  
 $\text{X}^+ \{ \text{Mo}_3\text{Se}_3 \}^-$  networks

John Gerard Sheridan (02174073)

A thesis submitted for the degree of  
Doctor of Philosophy  
at the  
University of Dublin

Supervisor: Prof. John J. Boland  
School of Chemistry  
Trinity College Dublin

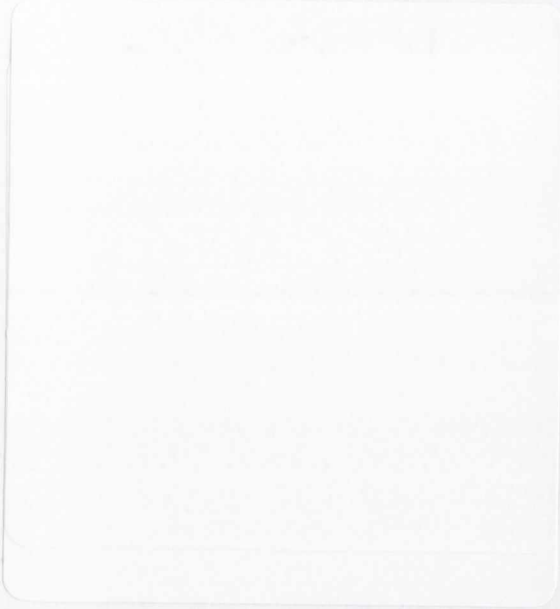
2011



Thesis 9572  
—

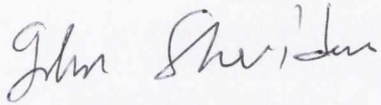
## DECLARATION

This thesis has not been submitted as an exercise for a degree at this or any other university, and, unless stated otherwise, is entirely my own work.



PERMISSION TO LEND AND/OR COPY

I give permission for the Library to lend or copy this thesis upon request.

A handwritten signature in cursive script that reads "John Sheridan". The signature is written in dark ink and is positioned above the printed name.

John Gerard Sheridan

## Summary

With the limits of current silicon processing techniques drawing nearer, the “bottom up” approach for future technologies has become a focus of major research worldwide. This requires detailed studies of possible replacement materials for interconnects and the active components of nanoscale devices. To this end we present results for the inorganic nanowire system,  $\text{Li}^+\{\text{Mo}_3\text{Se}_3\}^-$  and of its ion exchanged network counterparts,  $\text{X}^+\{\text{Mo}_3\text{Se}_3\}^-$ , by a variety of techniques, including Scanning Transmission Electron Microscopy (STEM) and its associated spectroscopies, Atomic Force Microscopy (AFM), rheology and dynamic light scattering of solutions.

$\text{Li}^+\{\text{Mo}_3\text{Se}_3\}^-$  forms quasi-1D crystals that can be dissolved in polar solvents such as DMSO. Dispersing these solutions on surfaces via drop casting or spin coating yields single wires (0.6 nm), bundles of nanowires and nanowire networks. These features are observed using a variety of solvents and substrates and all of these features are seen to coexist. Rheometry solution data is consistent with highly anisotropic particles or wires and light scattering measurements indicate a polydispersed size distribution.

STEM shows that networks of this material are continuous and not comprised of assemblies of individual wires. The mechanism of network formation is discussed based on cryogenic TEM imaging of nanowire solutions and observations of quenched nanowire network formation by AFM.

By replacing the  $\text{Li}^+$  counter ion with a fluorinated organic ligand, dense networks of  $\text{X}^+ \{\text{Mo}_3\text{Se}_3\}^-$  can be obtained. STEM reveals the inter-wire spacing to be ligand dependent and that individual nanowires within these networks persist over large length scales. Electrical measurements of these networks show a thermally activated behaviour with a transition noted at low temperatures which is fitted to a variable range hopping model.

## ACKNOWLEDGEMENTS

I would like to thank Prof. John J. Boland for all his support (scientific and moral) and patience during the course of this work. I am indebted and extremely grateful. I would also like to thank Noeleen Boland for her encouragement and support.

I would like to thank the funding bodies and collaborators:

Science Foundation Ireland

Centre for Research on Adaptive Nanostructures and Nanodevices

ESTEEM

Daresbury SuperSTEM facility (Dr. Andrew Bleoch and staff)

Dr. Peter Nellist for the TEM studies carried out at Daresbury, Oak Ridge and Oxford.

Dr. Richard Langford for his instruction with the FIB instrument and for the TEM imaging of nanowire cross-sections carried out at Hitachi, Japan.

Dr. Dermot Brougham and group at DCU for allowing me access to their Dynamic Light Scattering apparatus and assisting me with the interpretation of the data.

Dr. Dogan Ozkaya at Johnson Matthey, UK for the Cryo-TEM studies.

Prof. Earl Waghorne and Paul McCartin at UCD for access to their rheology equipment.

I would like to thank all the members of the Boland group, past and present, and the group administrators; Tom Bourke, Ger Hanley and Mary McCarthy.

Thanks to all the staff of CRANN and the Schools of Chemistry and Physics. I would also like to thank all the Intel staff involved with CRANN.

I would like to thank all my friends for their patience and encouragement.

I would like to thank my mother and family (in-laws and outlaws) for all their faith and support.

Finally I would like to thank Luci, who I may never be able to thank enough.



## TABLE OF CONTENTS

|  | Page  |
|--|-------|
| Title Page.....  | i     |
| Declaration .....  | ii    |
| Permission to lend and copy.....   | iii   |
| Summary.....   | iv    |
| Acknowledgements .....   | vi    |
| Table of Contents .....  | vii   |
| Glossary.....  | xi    |
| List of Figures.....   | xiii  |
| List of Tables.....  | xviii |
| 1. Introduction .....  | 1     |
| 1.1. Introduction .....  | 1     |
| 1.2. Structure of $\text{LiMo}_3\text{Se}_3$ nanowires.....              | 2     |
| 1.3. Electrical properties of $\text{LiMo}_3\text{Se}_3$ nanowires ..... | 4     |
| 1.4. Thesis Outline.....   | 7     |
| 1.5. References .....  | 9     |
| 2. Experimental Techniques .....   | 12    |
| 2.1. Atomic Force Microscopy .....                                       | 12    |
| 2.2. Electron Microscopy .....   | 14    |
| 2.2.1. Scanning Electron Microscopy.....                                 | 14    |
| 2.2.2. Transmission Electron Microscopy.....                             | 15    |
| 2.2.3. Scanning Transmission Electron Microscopy .....                   | 16    |
| 2.2.4. Energy Dispersive X-ray Analysis .....                            | 16    |
| 2.2.5. Electron Energy Loss Spectroscopy .....                           | 17    |
| 2.3. Viscosity Measurements.....   | 18    |

|   |    |
|---|----|
| 2.4. Dynamic Light Scattering .....   | 19 |
| 2.5. References .....   | 20 |
| 3. Synthesis, characterisation and sample preparation of $\text{LiMo}_3\text{Se}_3$<br>and ion-exchanged $\text{X}^+\{\text{Mo}_3\text{Se}_3\}^-$ ..... | 22 |
| 3.1. Introduction .....   | 22 |
| 3.2. Synthesis of $\text{LiMo}_3\text{Se}_3$ .....  | 22 |
| 3.3. Characterisation of synthesised $\text{LiMo}_3\text{Se}_3$ materials .....   | 25 |
| 3.3.1. PXRD of $\text{LiMo}_3\text{Se}_3$ .....   | 25 |
| 3.3.2. EDX of $\text{LiMo}_3\text{Se}_3$ .....  | 28 |
| 3.3.3. Solutions of $\text{LiMo}_3\text{Se}_3$ .....  | 31 |
| 3.4. Preparation of ion-exchanged $\text{X}^+\{\text{Mo}_3\text{Se}_3\}^-$ using organic ligands.....   | 33 |
| 3.5. Conclusions .....  | 35 |
| 3.6. References .....   | 36 |
| 4. Solution cast $\text{LiMo}_3\text{Se}_3$ nanowires and networks .....  | 38 |
| 4.1. Introduction .....   | 38 |
| 4.2. Sample Preparation .....   | 39 |
| 4.3. Results .....  | 41 |
| 4.3.1. $\text{LiMo}_3\text{Se}_3$ bundles .....   | 41 |
| 4.3.2. $\text{LiMo}_3\text{Se}_3$ networks .....  | 49 |
| 4.4. Conclusions .....  | 56 |
| 4.5. References .....   | 59 |
| 5. Characterisation of solutions of $\text{LiMo}_3\text{Se}_3$ dissolved in dimethyl sulfoxide .  | 61 |
| 5.1. Introduction .....   | 61 |
| 5.2. Characterisation .....   | 62 |
| 5.2.1. Rheometry of $\text{LiMo}_3\text{Se}_3(\text{DMSO})$ solutions.....  | 62 |

|         |   |     |
|---------|---|-----|
| 5.2.2.  | Dynamic Light Scattering.....   | 63  |
| 5.2.3.  | Dynamic Light Scattering comparison of filtered<br>solutions kept in inert atmosphere and filtered solutions<br>exposed to air..... | 68  |
| 5.2.4.  | UV-vis spectroscopy of an air exposed $\text{LiMo}_3\text{Se}_3$ solution .....   | 73  |
| 5.3.    | Discussion and Conclusions .....  | 76  |
| 5.3.1   | Discussion .....  | 76  |
| 5.3.2   | Conclusions .....   | 77  |
| 5.4.    | References .....  | 78  |
| 6.      | Electron Microscopy of frozen and freeze-dried $\text{LiMo}_3\text{Se}_3$<br>nanowire solutions.....                                | 80  |
| 6.1.    | Introduction .....  | 80  |
| 6.2.    | Experimental.....   | 80  |
| 6.3.    | Characterisation.....   | 82  |
| 6.3.1.  | Cryo-TEM of $\text{LiMo}_3\text{Se}_3(\text{DMSO})$ solutions .....   | 82  |
| 6.3.1.a | Freeze-drying of $\text{LiMo}_3\text{Se}_3(\text{DMSO})$ samples .....  | 85  |
| 6.3.2.  | Cryo-TEM of aqueous $\text{LiMo}_3\text{Se}_3$ solutions.....   | 87  |
| 6.3.2.a | Freeze-drying of $\text{LiMo}_3\text{Se}_3(\text{aq})$ samples.....   | 93  |
| 6.3.3   | Electron microscopy of freeze-dried filtered<br>$\text{LiMo}_3\text{Se}_3(\text{DMSO})$ solutions.....                              | 97  |
| 6.4.    | Conclusions .....   | 103 |
| 6.5.    | References .....  | 106 |
| 7.      | Electron Microscopy of ion-exchanged $\text{X}+\{\text{Mo}_3\text{Se}_3\}$ - networks .....   | 108 |
| 7.1.    | Introduction .....  | 108 |
| 7.2.    | Background.....   | 109 |
| 7.3.    | Characterisation.....   | 112 |
| 7.3.1.  | Characterisation of Surf 3 $\{\text{Mo}_3\text{Se}_3\}$ networks .....  | 112 |

|         |  |     |
|---------|--|-----|
| 7.3.1.a | Dependence of parent Li Mo <sub>3</sub> Se <sub>3</sub> solution concentration on Surf3 { Mo <sub>3</sub> Se <sub>3</sub> } network formation..... | 121 |
| 7.3.2.  | Characterisation of X+{ Mo <sub>3</sub> Se <sub>3</sub> } - networks formed from X = Surf 4, Surf 5 and Surf Thio .....                            | 124 |
| 7.4.    | Conclusions.....   | 128 |
| 7.5.    | References.....  | 130 |
| 8.      | Electrical properties of LiMo <sub>3</sub> Se <sub>3</sub> bundles and ion-exchanged X+{ Mo <sub>3</sub> Se <sub>3</sub> } - networks .....        | 131 |
| 8.1.    | Introduction.....  | 131 |
| 8.2.    | Characterisation .....   | 132 |
| 8.2.1.  | Electrical properties of LiMo <sub>3</sub> Se <sub>3</sub> bundle in air.....  | 132 |
| 8.2.2.  | Resistance as a function of temperature of LiMo <sub>3</sub> Se <sub>3</sub> bundle under vacuum.....  | 136 |
| 8.2.3.  | Ion-exchanged X <sup>+</sup> {Mo <sub>3</sub> Se <sub>3</sub> } <sup>-</sup> networks.....   | 141 |
| 8.3.    | Conclusions.....   | 152 |
| 8.4.    | References.....  | 154 |
| 9.      | Conclusions and Outlook.....   | 156 |
| 9.1     | Conclusions.....   | 156 |
| 9.2     | Outlook and Future Work.....   | 158 |
| 9.3     | References.....  | 162 |

## GLOSSARY

|                                 |   |
|---------------------------------|---|
| Å                               | Angstrom                                  |
| AFM                             | atomic force microscopy                   |
| c                               | concentration                             |
| d                               | d-spacing                                 |
| D                               | translational diffusion coefficient       |
| DI                              | deionised                                 |
| DLS                             | dynamic light scattering                  |
| DMSO                            | dimethyl sulfoxide                        |
| dyn                             | dyne (10 micro Newtons)                   |
| EDX                             | Energy Dispersive X-ray analysis          |
| EELS                            | electron energy loss spectroscopy         |
| eV                              | electron volt                             |
| <i>f</i>                        | frictional coefficient of a particle      |
| FIB                             | focused ion beam                          |
| HAADF                           | high angle annular dark field             |
| HOPG                            | highly oriented pyrolytic graphite        |
| HPPS                            | high performance particle sizer           |
| hrs                             | hours                                     |
| I                               | current                                   |
| <i>k</i> , <i>k<sub>B</sub></i> | Boltzmann's constant                      |
| L                               | length                                    |
| <i>l</i>                        | cuvette length                            |
| lhs                             | left hand side                            |
| LN2                             | liquid nitrogen                           |
| M                               | molar                                     |
| m.p.                            | melting point                             |
| N                               | Newtons                                   |
| nm                              | nanometer                                 |
| NMF                             | N-methylformamide                         |
| P                               | poise (equal to 0.1 Pascal*second)        |
| PC                              | propylene carbonate                       |
| PDF                             | Powder Diffraction File                   |
| PTFE                            | polytetrafluoroethylene                   |
| PXRD                            | Powder X-ray Diffraction                  |
| r                               | radius                                    |
| R                               | resistance                                |
| R <sub>g</sub>                  | radios of gyration                        |
| R <sub>H</sub>                  | hydrodynamic Radius                       |
| rhs                             | right hand side                           |
| s                               | seconds                                   |
| SEM                             | scanning electron microscopy              |
| STEM                            | scanning transmission electron microscopy |
| Surf                            | surfactant                                |
| T                               | Temperature                               |
| TEM                             | transmission electron microscopy          |
| t <sub>ox</sub>                 | oxidation time                            |
| UV/vis                          | ultraviolet/visible spectroscopy          |
| V                               | volt                                      |

|               |                        |
|---------------|------------------------|
| VRH           | Variable Range Hopping |
| XRD           | X-ray Diffraction      |
| Z             | atomic mass number     |
| $\epsilon$    | molar absorptivity     |
| $\eta$        | viscosity              |
| $\Theta$      | diffraction angle      |
| $\lambda$     | wavelength             |
| $\mu\text{m}$ | micrometer             |
| $\sigma$      | standard deviation     |
| $\Omega$      | ohm                    |

## LIST OF FIGURES

- Figure 1.1: Structure of  $\text{Mo}_6\text{Se}_8$ ,  $\text{Mo}_9\text{Se}_{11}$ ,  $\text{Mo}_{12}\text{Se}_{14}$ ,  $(\text{Mo}_3\text{Se}_3)_\infty$
- Figure 2.1: Schematic of AFM operation
- Figure 2.2: Schematic of electron interactions with a sample in an electron microscope
- Figure 2.3: EDX Schematic
- Figure 2.4: Schematic of Couette and Die and an image of Rheometric Scientific SR2000
- Figure 2.5: Graph of shear stress vs. shear rate for non-Newtonian liquids and a Newtonian liquid
- Figure 3.1: Schematic of quartz ampoule for materials synthesis
- Figure 3.2: PXRD spectrum of  $\text{InMo}_3\text{Se}_3$  with reference file
- Figure 3.3: PXRD spectra of  $\text{LiMo}_3\text{Se}_3$  and  $\text{InMo}_3\text{Se}_3$
- Figure 3.4: EDX analysis of  $\text{LiMo}_3\text{Se}_3$  material
- Figure 3.5: EDX analysis of  $\text{LiMo}_3\text{Se}_3$  material
- Figure 3.6: UV/vis absorption spectrum of a  $10^{-4}\text{M}$   $\text{LiMo}_3\text{Se}_3(\text{DMSO})$  solution
- Figure 3.7: Ball and stick models of  $\text{LiMo}_3\text{Se}_3$  bundles
- Figure 4.1: Schematic of the structure of  $\text{LiMo}_3\text{Se}_3$
- Figure 4.2: TEM image of  $\text{LiMo}_3\text{Se}_3$  crystallite deposited on holey carbon film from solution
- Figure 4.3: SEM images of  $\text{LiMoSe}$  bundles surrounded by network on  $\text{SiO}_2$
- Figure 4.4: AFM images of  $\text{LiMoSe}$  bundles and network on HOPG
- Figure 4.5: HAADF STEM image and line profile of a  $\text{LiMo}_3\text{Se}_3$  bundle
- Figure 4.6: HAADF STEM image of  $\text{LiMo}_3\text{Se}_3$  bundle and corresponding profiles
- Figure 4.7: HAADF STEM image of  $\text{LiMoSe}$  bundle, corresponding profile and EEL spectra
- Figure 4.8: SEM and STEM images of cross sections of  $\text{LiMo}_3\text{Se}_3$  bundles
- Figure 4.9: AFM image of a network of  $\text{LiMo}_3\text{Se}_3$  cast from DMSO solution onto HOPG with line profiles

- Figure 4.10: EDX spectrum obtained from a LiMoSe network
- Figure 4.11: HAADF STEM images of junctions and corresponding profiles
- Figure 4.12: HAADF STEM images of LiMoSe nanowire network junctions and corresponding profiles
- Figure 4.13: Graph of areas of Li and In edges relative to the normalized Mo edge obtained from EELS data of  $\text{LiMo}_3\text{Se}_3$  network and bundle
- Figure 4.14: AFM images of  $\text{LiMo}_3\text{Se}_3$  networks
- Figure 5.1: Rheology for  $10^{-2}\text{M}$  and  $10^{-4}\text{M}$   $\text{LiMo}_3\text{Se}_3(\text{DMSO})$  solutions showing shear thinning at higher concentrations and shear thickening at lower concentrations
- Figure 5.2: Dynamic light scattering data for  $10^{-4}$  and  $10^{-5}$  M  $\text{LiMo}_3\text{Se}_3(\text{DMSO})$  solutions
- Figure 5.3: STEM image of a network formed from a filtered  $10^{-4}\text{M}$   $\text{LiMo}_3\text{Se}_3(\text{DMSO})$  solution
- Figure 5.4: Normalised correlograms from DLS measurements on a filtered  $10^{-5}\text{M}$   $\text{LiMo}_3\text{Se}_3(\text{DMSO})$  solution stored under glove box conditions
- Figure 5.5: Normalised correlograms of an air exposed, filtered  $10^{-5}\text{M}$   $\text{LiMo}_3\text{Se}_3(\text{DMSO})$  solution
- Figure 5.6: Plot of  $t_{0.5}$  vs. time for air exposed  $10^{-5}\text{M}$  and  $10^{-4}\text{M}$  filtered  $\text{LiMo}_3\text{Se}_3(\text{DMSO})$  solutions
- Figure 5.7: SEM images of  $10^{-4}\text{M}$  (lhs) and  $10^{-5}\text{M}$  (rhs) air exposed  $\text{LiMo}_3\text{Se}_3(\text{DMSO})$  solutions deposited on  $\text{SiO}_2$
- Figure 5.8: UV-vis spectra of an air exposed  $10^{-4}\text{M}$   $\text{LiMo}_3\text{Se}_3$  solution recorded over time
- Figure 5.9: Absorbance (at 479 nm) vs. time for a  $10^{-4}\text{M}$   $\text{LiMo}_3\text{Se}_3(\text{DMSO})$  solution
- Figure 6.1: Gatan Cryoplunge system
- Figure 6.2: Frozen  $\text{LiMo}_3\text{Se}_3(\text{DMSO})$  nanowire solution suspended on a TEM grid carbon film
- Figure 6.3: TEM and STEM images of  $\text{LiMo}_3\text{Se}_3$  particles suspended in the frozen DMSO
- Figure 6.4: STEM image of a dense area of frozen  $\text{LiMo}_3\text{Se}_3(\text{DMSO})$  solution on carbon support film and associated EDX spectra



- Figure 6.5: STEM image of freeze dried  $\text{LiMo}_3\text{Se}_3(\text{DMSO})$  on a lacy carbon film TEM with EDX
- Figure 6.6: STEM images of frozen unfiltered  $\text{LiMo}_3\text{Se}_3(\text{aq})$
- Figure 6.7: STEM images of frozen unfiltered  $\text{LiMo}_3\text{Se}_3(\text{aq})$  solutions on lacy carbon TEM grid
- Figure 6.8: Series of STEM images of a frozen aqueous  $\text{LiMo}_3\text{Se}_3$  solution film (on a lacy carbon TEM grid) sputtering under the electron beam and the resultant agglomeration of nanowire particles
- Figure 6.9: STEM images of frozen aqueous  $\text{LiMo}_3\text{Se}_3$  solution on lacy carbon TEM grid with SEM of oxidized material for comparison
- Figure 6.10: TEM image of freeze dried aqueous  $\text{LiMo}_3\text{Se}_3$  on lacy carbon TEM grid
- Figure 6.11: STEM image of freeze dried aqueous  $\text{LiMo}_3\text{Se}_3$  showing network like material
- Figure 6.12: STEM image of freeze dried aqueous  $\text{LiMo}_3\text{Se}_3$  junction with EDX
- Figure 6.13: STEM images and EDX spectra of freeze dried unfiltered  $\text{LiMo}_3\text{Se}_3(\text{aq})$
- Figure 6.14: TEM images of freeze-dried filtered  $\text{LiMo}_3\text{Se}_3(\text{DMSO})$  solutions on lacy carbon TEM grid
- Figure 6.15: TEM images of freeze-dried  $\text{LiMo}_3\text{Se}_3(\text{DMSO})$  junctions
- Figure 6.16: STEM image of freeze-dried filtered  $\text{LiMo}_3\text{Se}_3(\text{DMSO})$  on lacy carbon TEM grid
- Figure 6.17: STEM image of freeze-dried filtered  $\text{LiMo}_3\text{Se}_3(\text{DMSO})$  solution and corresponding EDX analysis
- Figure 6.18: STEM images of freeze-dried, filtered  $\text{LiMo}_3\text{Se}_3(\text{DMSO})$  solution with EDX linescans
- Figure 7.1: Ball and stick cartoon of ligands attached to a segment of a  $\{\text{Mo}_3\text{Se}_3\}_\infty$  chain) and possible resultant hexagonal and lamellar structures
- Figure 7.2: STEM image of  $\text{Surf}_3\{\text{Mo}_3\text{Se}_3\}$
- Figure 7.3: STEM image of an area of  $\text{Surf}_3\{\text{Mo}_3\text{Se}_3\}$  and EEL spectra
- Figure 7.4: Higher magnification image of the area displayed in figure 7.2.

- Figure 7.5: Magnification of the area in figure 7.4.
- Figure 7.6: EELS spectrum image of figure 7.5.
- Figure 7.7: EEL spectra from various areas of Surf3  $\{\text{Mo}_3\text{Se}_3\}^-$  network
- Figure 7.8: EEL spectrum of a Surf3  $\{\text{Mo}_3\text{Se}_3\}$  network
- Figure 7.9: TEM image of Surf3  $\{\text{Mo}_3\text{Se}_3\}$  prepared from a  $10^{-4}\text{M}$   $\text{LiMo}_3\text{Se}_3$  solution
- Figure 7.10: TEM image of Surf3  $\{\text{Mo}_3\text{Se}_3\}$  prepared from a  $10^{-5}\text{M}$   $\text{LiMo}_3\text{Se}_3$  solution
- Figure 7.11: STEM image of Surf4  $\{\text{Mo}_3\text{Se}_3\}$
- Figure 7.12: STEM image of Surf5  $\{\text{Mo}_3\text{Se}_3\}$
- Figure 7.13: STEM image of SurfThio  $\{\text{Mo}_3\text{Se}_3\}$
- Figure 8.1:  $\text{LiMo}_3\text{Se}_3$  bundle for electrical measurements
- Figure 8.2: Successive I-V plots for a 110 nm diameter  $\text{LiMo}_3\text{Se}_3$  bundle, obtained as the specimen was exposed to air
- Figure 8.3: Resistance vs. time and effective conducting core radius vs. time for  $\text{LiMo}_3\text{Se}_3$  bundle exposed to ambient
- Figure 8.4: Natural logarithm of the conductivity vs. the inverse temperature for a  $\text{LiMo}_3\text{Se}_3$  bundle under vacuum
- Figure 8.5: I-V plots for  $\text{LiMo}_3\text{Se}_3$  bundle under vacuum at different temperatures
- Figure 8.6:  $\ln \sigma$  vs  $T^{-1}$ ,  $T^{-1/2}$ ,  $T^{-1/3}$ ,  $T^{-1/4}$  for a  $\text{LiMoSe}$  bundle
- Figure 8.7: Conduction schematic for  $\text{LiMo}_3\text{Se}_3$  nanowires
- Figure 8.8: Schematic of ion-exchanged samples used for resistance vs. temperature measurements
- Figure 8.9:  $\ln \sigma$  vs  $T^{-1}$  for surf3  $\{\text{Mo}_3\text{Se}_3\}$  (under vacuum)
- Figure 8.10:  $\ln \sigma$  vs  $T^{-1}$  for various ion-exchanged networks under vacuum
- Figure 8.11: Representative plot of  $\ln \sigma$  vs.  $T^{-1}$  showing the straight line regions where energies are calculated and the transition temperatures between these regions

Figure 8.12: Surf3MoSe:  $\ln \sigma$  vs  $T^{-1}$ ,  $T^{-1/2}$ ,  $T^{-1/3}$ ,  $T^{-1/4}$ .

Figure 8.13: Activation energy vs interwire separation for LiMoSe bundle and surfX{MoSe} networks at low ( $< 8$  K) temperatures

Figure 8.14: I-V plots of each of the surfactant {Mo3Se3} samples at various temperatures.

Figure 8.15: Normalised resistance vs. temperature plots for LiMoSe bundle and all ion-exchanged samples

Figure 9.1: Schematic of Conductive AFM and example graph of a two terminal measurement used to estimate the contact resistance

## LIST OF TABLES

- Table 3.1: PXRD experimental and reference d-values for  $\text{InMo}_3\text{Se}_3$
- Table 3.2: Experimental and literature d-values for  $\text{LiMo}_3\text{Se}_3$
- Table 3.3: Ligands, X, used to prepare ion-exchanged  $\text{X}^+\{\text{Mo}_3\text{Se}_3\}^-$
- Table 7.1: Ligands used to prepare ion-exchanged networks
- Table 7.2: Mean interwire spacings
- Table 8.1: Temperature ranges and calculated activation energy for  $\text{LiMo}_3\text{Se}_3$  nanowire
- Table 8.2: Ligands used to form  $\text{X}^+\{\text{Mo}_3\text{Se}_3\}^-$  networks
- Table 8.3: Activation energies for surfactants 3, 4, 5, 6 and thio at each temperature region.

# Chapter 1

## Introduction

### 1.1 Introduction

Since the advent of the integrated circuit, (Kilby 1959)[1] miniaturization of electronic circuits has been instrumental in advancing many kinds of technologies, from medical devices and high performance computers to consumer electronics (mobile phones, flat panel displays, etc.). This trend towards miniaturization coupled with advances in microscopy has opened many new avenues of research. Nano-materials have received much interest due to their unique properties which differ from their bulk counterparts.[2] There has been much research interest in quasi one dimensional materials as interconnects for existing technologies and as devices in their own right.[2-4] This interest is due to the impending limits of conventional lithography techniques which will result in a fall off from the linear Moore's Law which has directed the semiconductor industry for the past 45 years. Moore suggested, in 1965, that the number of transistors on an integrated circuit would double roughly every 24 months.[5] In microelectronics, there has been a constant drive to make circuits and devices increasingly small, resulting in faster, cheaper and more efficient integrated circuits. Already, this industry is beginning to look beyond the current tooling and manufacturing methods to nanoscale and "bottom-up" technologies to facilitate smaller and faster device structures.

To implement new technologies based on these one dimensional materials, a systematic study of their electronic, chemical and mechanical properties is required. Much of the study so far has centered on carbon nanotubes[6, 7] with relatively little research directed to other nanowire systems. However, there are problems with carbon nanotubes such as difficulty in purification and the fact that they are a structurally and electronically diverse material. For one dimensional materials to be implemented in future electronic devices, these difficulties must be overcome, or a material of similar physical properties but less structural diversity must be utilized.

## 1.2 Structure of LiMo<sub>3</sub>Se<sub>3</sub> nanowires

LiMo<sub>3</sub>Se<sub>3</sub> is another example of a quasi one dimensional material.[8-11] Wires formed of this material should be structurally and electronically identical[2] in contrast to carbon nanotubes. LiMo<sub>3</sub>Se<sub>3</sub> dissolves in polar solvents such as DMSO and yields single nanowires (~ 6 Å diameter) and bundles of nanowires (up to 100 nm diameter) when dispersed on substrates (HOPG, SiO<sub>2</sub>). Herein, we will also discuss the formation of nanowire networks, often found surrounding these wire bundles.

The quasi one dimensional compounds of formula MMo<sub>3</sub>X<sub>3</sub> (where M = Na, In, K, Tl and X = Se, Te) were first discovered by Potel, et al.[12] and are structurally related to the Chevrel phases which have a stoichiometry of M<sub>x</sub>Mo<sub>3n</sub>X<sub>3n+2</sub> (n ≥ 2). Crystals of the material contain hexagonal close packed linear chains of Mo<sub>6</sub>X<sub>6</sub>. This Mo<sub>6</sub>X<sub>6</sub> chain is formed by staggered stacking of Mo<sub>3</sub>Se<sub>3</sub> units. They can be thought of as a one dimensional condensation of Chevrel phase octahedral clusters of molybdenum face capped with chalcogen atoms to form linear chains of (Mo<sub>3</sub>X<sub>3</sub>)<sub>∞</sub>.

(figure 1.1A).[13] As this condensation continues to form longer and longer chains, the Mo to X ratio is increased, giving the compound an increasing metallic character.[12] They are ternary molybdenum chalcogenides and their structure can be thought of as infinite alternating stacks of  $(\text{Mo}_3\text{X}_3)^-$  running along the hexagonal c-axis, separated by columns of the ternary element (figure 1.1B). Linear chains of the formula  $\text{MMo}_3\text{X}_3$  display many unique properties; highly anisotropic conductivity, superconductivity and semiconducting behaviour at low temperatures, depending on the chalcogen and the interstitial positively charged ion species between the chains.[14]

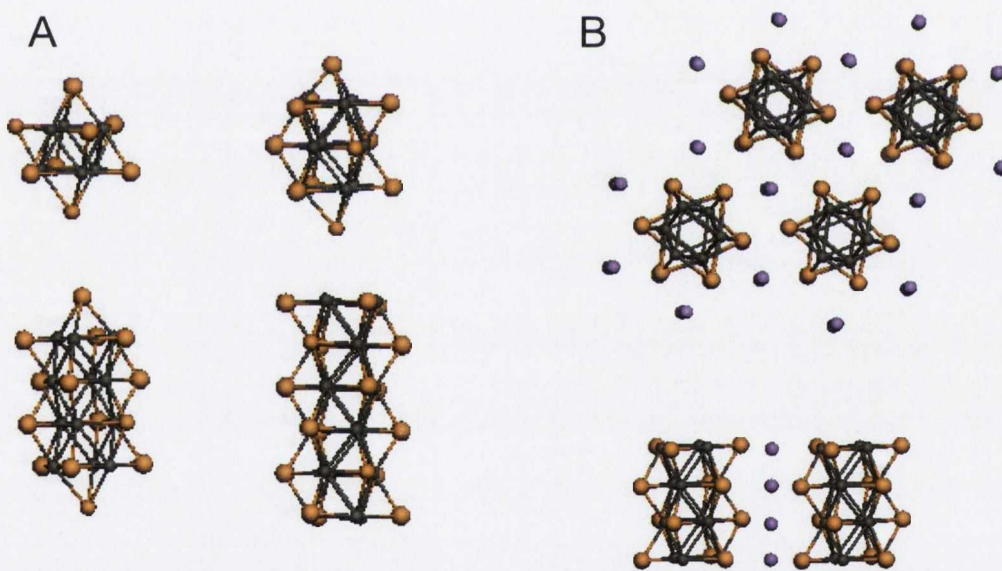


**Figure 1.1:** **A:** structure of  $\text{Mo}_6\text{Se}_8$ ,  $\text{Mo}_9\text{Se}_{11}$ ,  $\text{Mo}_{12}\text{Se}_{14}$ ,  $(\text{Mo}_3\text{Se}_3)_\infty$ . The character of the MoSe molecule becomes more metallic as the Mo:Se ratio increases. **B:**  $\text{LiMo}_3\text{Se}_3$  looking down the wire long axis (top) and side view of the structure. Grey = Mo, orange = Se, purple = Li

For the case of  $\text{LiMo}_3\text{Se}_3$ , these chains are separated by  $\sim 8.5 \text{ \AA}$  making this material strongly anisotropic.[15] The separation between each repeat  $(\text{Mo}_3\text{Se}_3)^-$  unit is  $4.5$

Å. These structures are essentially infinite molybdenum wire cores with a selenium cladding layer. In the crystal, these negatively charged strands are separated by  $\text{Li}^+$  counter ions.

Most  $\text{MMo}_3\text{X}_3$  compounds are insoluble, however, the  $\text{LiMo}_3\text{Se}_3$  compound is of particular interest as it is soluble in polar solvents yielding dark red solutions, which remain stable indefinitely if maintained in an oxygen/moisture free environment. However, the material will oxidise when exposed to air resulting in a precipitate. Previous data shows that when the solid reacts with air  $\text{LiOH}$  is formed, resulting in a decrease of the hexagonal lattice parameter.[15]

From these solutions, both single nanowires (diameter  $\sim 6$  Å) and bundles of nanowires (with diameters up to 100's of nanometers) can be dispersed on substrates, allowing for characterisation of these nanoscale strands and bundles.

### 1.3 Electrical properties of $\text{LiMo}_3\text{Se}_3$ nanowires.

Previously, electrical properties have been obtained for  $\text{LiMo}_3\text{Se}_3$  nanowires by STM (scanning tunnelling microscopy), resistivity measurements on films of ordered  $\text{LiMo}_3\text{Se}_3$  nanowires, four probe measurements of individual nanowire bundles and investigations of ion-exchanged nanowire networks.

Venkataraman et al.[16] performed STM on individual  $\text{LiMo}_3\text{Se}_3$  nanowires. They were able to resolve the individual wires and the repeat  $\text{Mo}_6\text{Se}_6$  unit. Samples were prepared from anhydrous DMSO solutions and deposited on Au(111)/mica and HOPG (highly ordered pyrolytic graphite) substrates. Samples were then transferred



to the STM system without exposure to air. I vs. V and normalised conductance data were obtained. Heidelberg, et al.[17] performed similar STS measurements on small bundles of these nanowires. In both cases, the wires exhibited metallic behaviour and low temperature measurements (to 5 K in the case Venkataraman et al) did not show the formation of a band-gap. However, it should be noted that for these types of measurements only the local conductance is measured and no data for the transport along a wire can be obtained.

Venkataraman et al.[18] also showed that mesoscopic nanowire samples (diameter > 1 $\mu$ m) display metallic behaviour with decreasing temperature, i.e., resistance decreased at lower temperatures, but two probe measurements of smaller wires (diameter 1-15nm) show increased resistance at lower temperatures. In their case, the sharp increase in resistance at low temperatures was attributed to Coulomb blockade and indicated the presence of tunnel junctions, most likely due to defects within the wire.

Heidelberg, et al. performed macroscopic four probe measurements on ion exchanged nanowire networks, where the Li<sup>+</sup> ion was replaced with organic ligands to lessen corrosion in air. They found that these networks conduct via a percolation mechanism and are considerably more stable in air than LiMo<sub>3</sub>Se<sub>3</sub> nanowires.[17]

Golden, et al.[19] performed four probe measurements on films of LiMo<sub>3</sub>Se<sub>3</sub> created by heating spin coated or drop cast layers. They recorded a thermally activated conductivity with a resistivity of  $5 \times 10^{-5} \Omega\text{m}$ . They also noted a semiconducting-

like behaviour of the film that they attribute to the possibility of a one-dimensional Peierls distortion.

Tarascon et al.[20] conducted bulk resistivity measurements on crystals of  $MMo_3X_3$  (such as  $CsMo_3Te_3$ ,  $RbMo_3Te_3$ ,  $RbMo_3Se_3$ ) and again a transition from metallic to semiconducting behaviour at low temperatures (liquid helium) was noted.

The research group of Dr. Peidong Yang at Berkeley has performed four probe measurements on patterned  $LiMo_3Se_3$  nanowires formed by microchannel networks ( $5 \times 10^{-5} \Omega m$ )[21] and on wires dispersed on gold electrode arrays ( $\sim 10^{-6} - 10^{-7} \Omega m$ ).[22] Low temperature resistivity measurements showed a plateau in the resistance around 20 K which they consider an indication of a Peierls distortion leading to a semiconducting ground state. They have also shown that these nanowires may self organise into mesoscopic bundles in solution, replacing the  $Li^+$  ion with positively charged organic surfactants.

Osterloh and group (UC Davis) have shown that films of  $LiMo_3Se_3$  can be used as reversible chemical sensors due to variations in the electrical conductivity of these films upon exposure to a variety of different analytes (e.g. methanol, acetonitrile, THF, hexane).[23-25] They have also shown that films of  $LiMo_3Se_3$  can be used to sense metal ions in water[26] and that  $LiMo_3Se_3$  nanowires can be used to form  $LiMo_3Se_3$ -nanoparticle composites using Au, Ag,  $Fe_3O_4$  and CdSe. [27-29]

## 1.4 Thesis Outline

The primary aims of this work are to;

- Examine the nature of the junctions observed in the large scale  $\text{LiMo}_3\text{Se}_3$  networks
- Propose a mechanism for the formation of these networks in terms of the properties of the solution from which the network was formed
- Develop a method to “Teflon-coat” the bare  $\text{Mo}_3\text{Se}_3$  wires using per-fluorinated organic ligands in order to hinder the oxidation of the material which greatly degrades the electrical transport of these wires
- Examine the effects of coating these wires with organic ligands in terms of the interwire separation and the electrical properties of the ion-exchanged materials compared to the pristine  $\text{LiMo}_3\text{Se}_3$  materials

This work focuses on the nature, formation, structural and electrical characteristics of  $\text{LiMo}_3\text{Se}_3$  and ion-exchanged  $\text{X}^+\{\text{Mo}_3\text{Se}_3\}^-$  networks. To date,  $\text{LiMo}_3\text{Se}_3$  networks of the structure noted herein, have not been reported in the literature. In this work, we investigate and discuss the structural differences between large crystalline  $\text{LiMo}_3\text{Se}_3$  bundles and these 2D  $\text{LiMo}_3\text{Se}_3$  networks. To elucidate the formation of these networks, Dynamic Light Scattering and cryogenic Transmission Electron Microscopy studies were performed. Electron microscopy and conductivity studies of ion-exchanged  $\text{X}^+\{\text{Mo}_3\text{Se}_3\}^-$  networks are also presented where a perfluorinated long chain organic ligand was used to replace the Li ion in an attempt

to retard the corrosion rate of these wires in moist air. More specifically, the following will be presented:

Chapter 3 will discuss the synthesis and characterisation of  $\text{LiMo}_3\text{Se}_3$  and ion-exchanged  $\text{X}^+\{\text{Mo}_3\text{Se}_3\}^-$  networks. The quality of the  $\text{LiMo}_3\text{Se}_3$  materials was investigated using techniques such as powder X-ray diffraction and energy dispersive X-ray analysis, in addition to investigations of the ability of the synthesised product to form stable solutions in inert atmospheres. The formation of  $\text{X}^+\{\text{Mo}_3\text{Se}_3\}^-$  networks by substituting the  $\text{Li}^+$  ion for a positively charged organic ligand will also be addressed.

In chapter 4, detailed analyses of drop cast and spun coated  $\text{LiMo}_3\text{Se}_3$  features on various substrate surfaces is performed using scanning transmission electron microscopy (STEM), transmission electron microscopy (TEM), scanning electron microscopy (SEM), and atomic force microscopy (AFM). Features noted include large crystalline nanowire bundles and nanowire networks. Electron Energy Loss Spectroscopy (EELS) of these features will also be presented.

In chapter 5, rheometry, dynamic light scattering (DLS) and UV-vis spectroscopy studies of the compositions of solutions of  $\text{LiMo}_3\text{Se}_3$  will be reported. These studies were conducted to elucidate the precise contents of material in solution in order to better explain the nature of the observed nanowire networks.

Chapter 6 includes results from cryo-TEM experiments conducted on frozen thin films of  $\text{LiMo}_3\text{Se}_3$  solutions. These studies were also aimed at gaining a better

understanding of the contents of solution and how that related to  $\text{LiMo}_3\text{Se}_3$  nanowires and networks observed on substrate surfaces after deposition via drop or spin coating.

Chapter 7 shows high resolution TEM and STEM images of ion-exchanged  $\text{X}^+\{\text{Mo}_3\text{Se}_3\}^-$  networks and relates the observed increase in interwire distance to the organic ligands ( $\text{X}^+$ ) used.

In chapter 8, the electrical conductivity of  $\text{LiMo}_3\text{Se}_3$  and ion-exchanged  $\text{X}^+\{\text{Mo}_3\text{Se}_3\}^-$  networks is presented at temperatures ranging from room temperature to 7 K. A study of the effect of air exposure on a  $\text{LiMo}_3\text{Se}_3$  bundles is also discussed.

## 1.5 References

- [1] H. Wong, *Physics World* **2005**.
- [2] Y. N. Xia, P. D. Yang, Y. G. Sun, Y. Y. Wu, B. Mayers, B. Gates, Y. D. Yin, F. Kim, Y. Q. Yan, *Advanced Materials* **2003**, *15*, 353.
- [3] C. Lieber, *Solid State Communications* **1998**, *107*, 607.
- [4] C. Dekker, *Physics Today* **1999**, 52.
- [5] G. E. Moore, *Electronics* **1965**, 38.
- [6] T. W. Ebbesen, *Annual Review of Materials Science* **1994**, 24.
- [7] E. T. Thostenson, Z. Ren, T.-W. Chou, *Composites Science and Technology* **2001**, *61*, 1899.
- [8] T. Hughbanks, R. Hoffman, *Inorganic Chemistry* **1982**, *21*, 3578.

- [9] T. Hughbanks, R. Hoffman, *Journal of the American Chemical Society* **1983**, 105.
- [10] B. Messer, J. H. Song, M. Huang, Y. Y. Wu, F. Kim, P. D. Yang, *Advanced Materials* **2000**, 12, 1526.
- [11] J. H. Song, Y. Y. Wu, B. Messer, H. Kind, P. D. Yang, *Journal of the American Chemical Society* **2001**, 123, 10397.
- [12] M. Potel, R. Chevrel, M. Sergent, J. C. Armici, M. Decroux, Ø. Fischer, *Journal of Solid State Chemistry* **1980**, 35, 286.
- [13] J. H. Golden, F. J. DiSalvo, J. M. J. Frechet, *Chemistry of Materials* **1994**, 6, 844.
- [14] J. M. Tarascon, F. J. DiSalvo, C. H. Chen, P. J. Carroll, M. Walsh, L. Rupp, *Journal of Solid State Chemistry* **1985**, 58, 290.
- [15] J. M. Tarascon, G. W. Hull, F. J. DiSalvo, *Materials Research Bulletin* **1984**, 19, 915.
- [16] L. Venkataraman, C. M. Lieber, *Physical Review Letters* **1999**, 83, 5334.
- [17] A. Heidelberg, H. Bloess, J. W. Schultze, C. J. Booth, E. T. Samulski, J. J. Boland, *Zeitschrift Fur Physikalische Chemie-International Journal of Research in Physical Chemistry & Chemical Physics* **2003**, 217, 573.
- [18] L. Venkataraman, Y. S. Hong, P. Kim, *Physical Review Letters* **2006**, 96, 76601.
- [19] J. H. Golden, F. J. DiSalvo, J. M. J. Frechet, *Chemistry of Materials* **1995**, 7, 232.
- [20] J. M. Tarascon, *Solid State Communications* **1984**, 52.
- [21] B. Messer, J. H. Song, P. D. Yang, *Journal of the American Chemical Society* **2000**, 122, 10232.

- [22] J. H. Song, B. Messer, Y. Y. Wu, H. Kind, P. D. Yang, *Journal of the American Chemical Society* **2001**, *123*, 9714.
- [23] X. B. Qi, F. E. Osterloh, *Journal of the American Chemical Society* **2005**, *127*, 7666.
- [24] X. B. Qi, F. E. Osterloh, S. A. Barriga, J. A. Giacomo, S. Chiang, *Analytical Chemistry* **2006**, *78*, 1306.
- [25] X. B. Qi, F. E. Osterloh, J. A. Giacomo, S. Chiang, *Langmuir* **2006**, *22*, 8253.
- [26] M. Allen, E. M. Sabio, X. B. Qi, B. Nwengela, M. S. Islam, F. E. Osterloh, *Langmuir* **2008**, *24*, 7031.
- [27] N. N. Akl, O. Trofymuk, X. B. Qi, J. Y. Kim, F. E. Osterloh, A. Navrotsky, *Angew. Chem.-Int. Edit.* **2006**, *45*, 3653.
- [28] F. E. Osterloh, H. Hiramatsu, R. K. Dumas, K. Liu, *Langmuir* **2005**, *21*, 9709.
- [29] F. E. Osterloh, J. S. Martino, H. Hiramatsu, D. P. Hewitt, *Nano Letters* **2003**, *3*, 125.

## Chapter 2

### Experimental Techniques

#### 2.1 Atomic Force Microscopy

Atomic Force Microscopy (AFM) was first reported by Binnig et al. in 1986.[1] In this technique, a sharp probe attached to a cantilever is raster scanned over a sample and the deflection of the tip due to interactions with the sample allow for an image of the sample topography to be generated.[2] Figure 2.1 shows a schematic of the operation of an AFM. The cantilever deflections are measured by shining a laser on the back of the cantilever and tracking the deflection on a quadrant photodetector. Thus, a combination of the normal and lateral deflections can be measured.

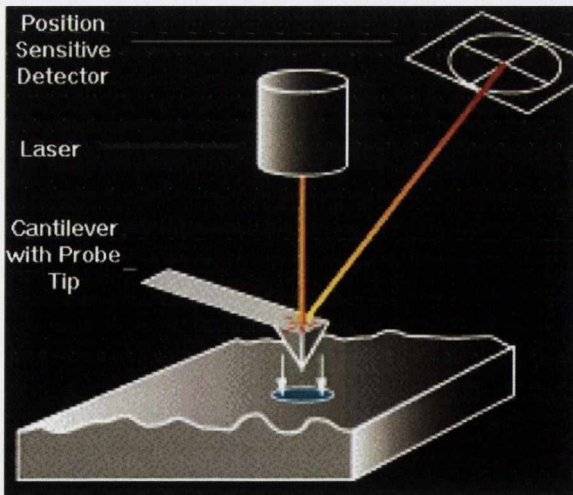


*Figure 2.1: Schematic of AFM operation*



At small tip-surface separations, a repulsive force dominates, while at larger separations the van der Waals force (attractive) dominates. The potential energy as a function of separation can be described by the Lennard-Jones potential:

$$E(r) = 4\varepsilon \left[ \left( \frac{\sigma}{r} \right)^{12} - \left( \frac{\sigma}{r} \right)^6 \right] \quad (2.1)$$

where  $\varepsilon$  and  $\sigma$  are material dependent constants. The rapid increase in  $E(r)$  at low separations (i.e. separations comparable to the size of the atoms) is accounted for by the  $1/r^{12}$  term. The  $1/r^6$  term dominates in the attractive regime.

There are two main modes of operation of an AFM; contact and non-contact. In contact mode, the cantilever is lowered until the tip is touching the sample surface. The force applied to the surface is proportional to the deflection of the cantilever and is pre-set by the user. The cantilever is then rastered back and forth over the sample. With the changing sample topography, the cantilever is deflected up or down. This deflection is sensed by the movement of the reflected laser beam on the photodetector. A feedback loop is used to keep the deflection setpoint of the cantilever constant. By recording the magnitude of the deflection with the position of the tip on the sample, an image of the surface is generated.

One drawback with contact mode AFM is the possibility of damaging the sample. In non-contact AFM, the cantilever is oscillated above the surface and the van der Waals attraction or electrostatic repulsion of the tip and sample is mapped. A feedback loop is employed to vary the height of the cantilever above the sample as the frequency or amplitude of the cantilever oscillation varies with changing topography.

Image quality and sensitivity in AFM is dominated by tip and cantilever geometry. In order to avoid thermal and mechanical fluctuations while scanning, the cantilever must have a high resonant frequency. An overly stiff cantilever will not be sensitive enough to detect many of the surface forces, hence a low spring constant is desirable to obtain a relatively large deflection and therefore a large signal. It can be seen from the equation for the resonant frequency of a spring:

$$f = \frac{1}{2\pi} \sqrt{\frac{c}{m}} \quad (2.2)$$

where  $c$  is the spring constant and  $m$  is the mass, that it is important to have a low mass cantilever to obtain favourable spring constants and resonant frequencies.

## 2.2 Electron Microscopy

### 2.2.1 Scanning Electron Microscopy (SEM)

In scanning electron microscopy, (SEM), electrons are generated from a source (via field emission or thermal emission) and are focussed towards the sample. The electron beam is confined and focused by a series of magnetic lenses and apertures into a monochromatic beam which can be scanned across the sample. It is possible to generate an image of the surface of the material giving topographical and morphological information by using detectors to sense the energies of the emerging electrons (Auger, backscattered, secondary, figure 2.2) and synchronising these signals with the position of the rastering beam.[3] The detected electrons can be either Auger, backscattered or secondary. A backscattered electron is an electron reflected back the same direction as it arrived due to interaction with the nucleus. Secondary electrons are electrons in the sample which have been excited out of their

shells by the incident electron beam. Auger electrons are caused when the incident electron beam removes a core level electron in the sample. A higher level electron may fall to fill this vacancy resulting in a release of energy which may be emitted as an X-ray or this energy may be transferred to another electron causing it to eject from the atom (an Auger electron).

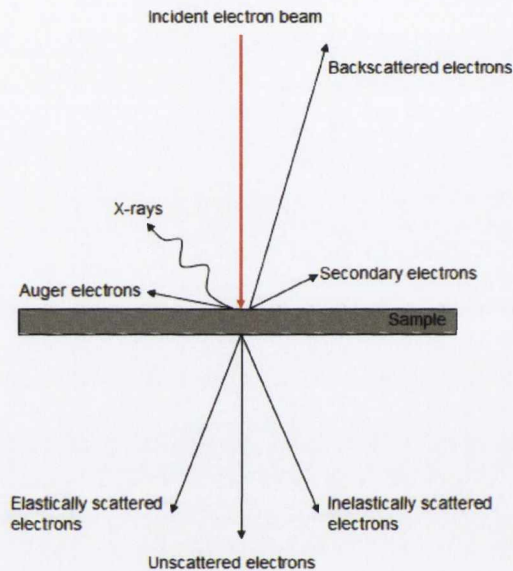


**Figure 2.2:** Schematic of electron interactions with a sample in an electron microscope

### 2.2.2 Transmission Electron Microscopy (TEM)

In TEM, a beam of electrons are focused, by magnetic lenses, on a thin specimen. In this case, the electrons transmitted through the sample are collected. From the unscattered electrons (transmitted without interacting with the atom), elastically scattered electrons (no energy loss) and inelastically (energy loss) scattered electrons, an image of the sample can be obtained which can also give crystallographic information. Because the beam of electrons must pass through the sample, it is important to make the sample as thin as possible. Therefore, sample

preparation is an important aspect of TEM. The resultant image is collected using a CCD camera or on a phosphor screen.[4]

### 2.2.3 Scanning Transmission Electron Microscopy (STEM)

Scanning Transmission Electron Microscopy allows for more detailed images of thin samples to be generated. In STEM, a small electron beam probe (focussed to form an image of the electron gun at the specimen stage) is raster scanned over the sample. The electron beam passes through the sample and is simultaneously detected by the bright field detector (which detects low angle scattering) and the high angle annular dark field (HAADF) detector (which detects at higher angles).[5] The bright field detector forms an image from unscattered electrons or inelastically scattered electrons which have only been scattered through very small angles. The HAADF image contains information on the chemical composition of the sample because the image is formed from high angle inelastically scattered electrons which have lost a characteristic amount of energy during their interaction with the sample. The contrast in HAADF images is a result of the scaling of the measured signal which is proportional to  $Z^2$  (atomic mass).[6]

Both SEM and S/TEM can provide information of the chemical composition of a sample if equipped with suitable detection systems such as EDX and EELS.

### 2.2.4 Energy Dispersive X-ray analysis (EDX)

Energy dispersive X-ray analysis is performed by irradiating a sample with a high energy beam of electrons. This incident beam can excite a core electron, removing it

from the atom. A higher energy electron will then fall to fill this vacancy resulting in a release of energy which may be emitted as an X-ray whose energy is characteristic of the difference between energy levels in the transition, figure 2.3. The number and energy of the X-rays emitted is recorded using an energy dispersive spectrometer.[7] The energy difference between the levels is unique for all elements and so identification of different elemental species present in the sample is possible.

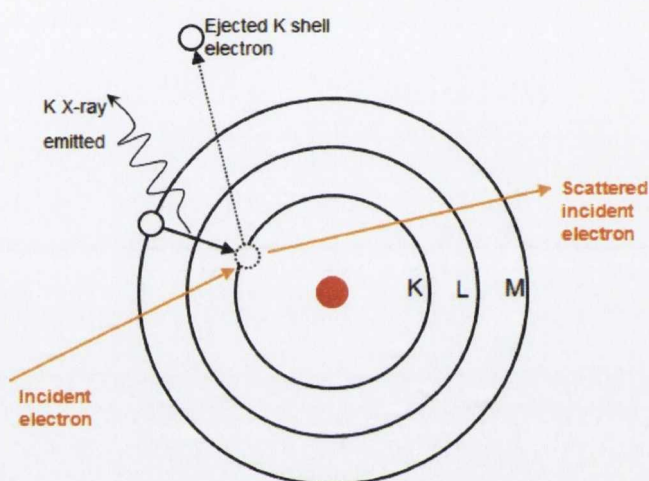


**Figure 2.3:** EDX: ionization of a core electron by a incident beam electron (orange). The atom relaxes to its ground state by an electron falling from a higher energy orbital to a lower energy orbital with the emission of an X-ray or Auger electron

### 2.2.5 Electron Energy Loss Spectroscopy (EELS)

Electron Energy Loss Spectroscopy (EELS) is a process by which characteristic elemental information can be gathered by examining the energy loss of an electron beam as it passes through a thin sample in a TEM. The energy loss occurs by inelastic electron scattering. Following transmission through a sample, a small percentage of the electrons in the beam have lost energy to inelastic scattering events such as plasmon or phonon excitations, or core excitations.[8] The core excitation energy losses can be used to identify chemical species present in the sample. To

measure the difference in energies between the unscattered electron beam and the inelastically scattered electrons, an EEL spectrometer may be mounted after the specimen stage.[6]

### 2.3 Viscosity Measurements.

Viscosity measurements were carried out using a Rheometric Scientific SR 2000 with a rotational coaxial-cylinder viscometer which consisted of a couette and die. This type of viscometer is frequently used for measuring the steady state viscosity and dynamic mechanical properties of low viscosity solutions, polymer solutions, etc. In this instrument, the liquid is placed in the couette and then the die (whose diameter is such that the gap between die and couette is small) is lowered into the couette (figure 2.4). The die is rotated under a constant torque and the speed of rotation is measured using a tachometer. At regular intervals, the torque driving the die was increased, allowing stress creep information to be obtained.[9]

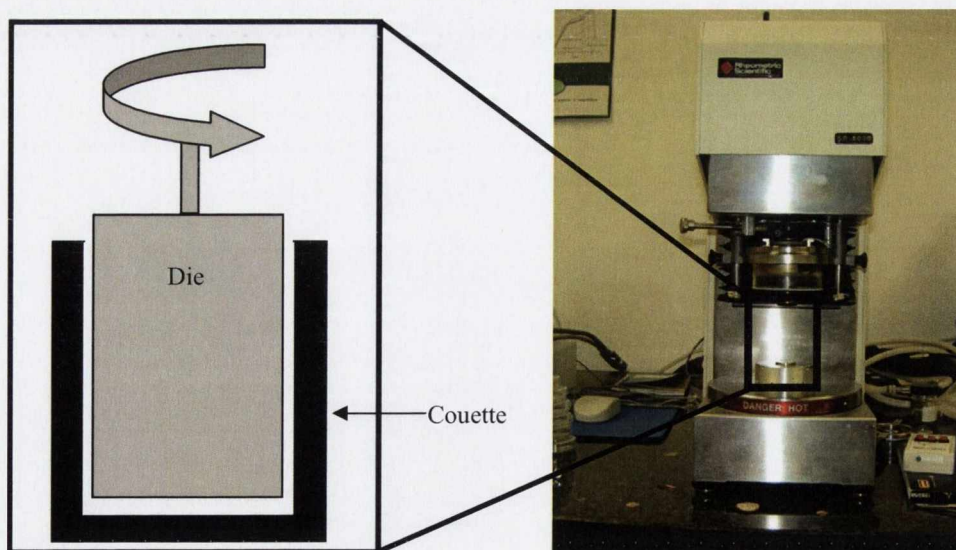


**Figure 2.4:** Schematic of Couette and Die (left) and an image of Rheometric Scientific SR2000 (right)

Liquids subjected to a shear or tensile stress deform. Under shear, the rate of deformation (or shear rate) is proportional to the shearing stress. Newton proposed that the ratio of the stress ( $\tau$ ) to the shear rate ( $\dot{\gamma}$ ) is a constant called the viscosity.[10] The dynamic viscosity ( $\eta$ ) of a liquid is equal to the gradient of the shear stress – shear rate curve (figure 2.5):

$$\eta = \frac{d\tau}{d\dot{\gamma}} \quad (2.3)$$

For “Newtonian” or ideal liquids, the viscosity is independent of the shear rate, however non-Newtonian liquids are classified according to their viscosity behaviour as a function of shear rate and can undergo shear-thickening or shear-thinning.

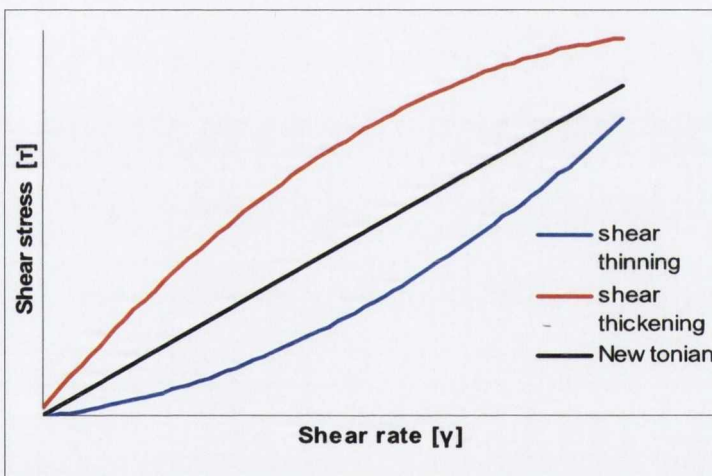


**Figure 2.5:** Shear stress vs. shear rate for non-Newtonian liquids (red and blue) and a Newtonian liquid (black)

## 2.4 Dynamic Light Scattering (DLS)

Dynamic Light Scattering measures Brownian motion and relates this to the particle size in solution. Larger particles diffuse slower than smaller particles. A low power laser is scattered by particles in suspension. In DLS, the speed at which the particles are diffusing is measured by recording the rate of the variation of the intensity of the scattered light.[11] The correlation between measurements in a fluctuating signal is

determined using a correlation function. The correlation of the signal will decay faster for motion due to small particles than for large particles.

The size of the particle is described using the Stokes-Einstein relation [12, 13]:

$$D = \frac{kT}{f} = \frac{kT}{6\pi\eta R_H} \quad (2.4)$$

Where  $D$  is the translational diffusion coefficient,  $k$  is the Boltzmann constant,  $T$  is the absolute temperature,  $f$  is the frictional coefficient of the particle,  $\eta$  is the viscosity and  $R_H$  is the hydrodynamic radius.

## 2.5 References

- [1] G. Binnig, C. F. Quate, C. Gerber, *Physical Review Letters* **1986**, 56, 930.
- [2] N. Spencer, S. P. Jarvis, *Encyclopedia of Chemical Physics and Physical Chemistry, Vol 3 Methods, IOP.*, 3, 1467.
- [3] C. P. Poole, F. J. Owens, *Introduction to Nanoscience*, Wiley-Interscience, **2003**.
- [4] I. M. Watt, *The Principles and Practice of Electron Microscopy*, Cambridge University Press, **1997**.
- [5] M. D. Hornbostel, S. Hillyard, J. Silcox, F. J. Disalvo, *Nanotechnology* **1995**, 6, 87.
- [6] B. Fultz, J. M. Howe, *Transmission Electron Microscopy and Diffractometry of Materials*, Springer, **2008**.
- [7] J. Goldstein, *Scanning Electron Microscopy and X-ray Microanalysis*, Springer, **2003**.



- [8] R. Brydson, *Electron Energy Loss Spectroscopy*, BIOS Scientific Publishers **2001**.
- [9] R. K. Gupta, *Polymer and Composite Rheology*, Marcel Dekker, **2000**.
- [10] H. D. B. Jenkins, Y. M. Marcus, *Chemical Reviews* **1995**, 95, 2695.
- [11] Malvern\_Instruments, *Technical Note*, [www.malvern.com](http://www.malvern.com), *Introduction to Dynamic Light Scattering*.
- [12] N. C. Santos, M. A. Castanho, *Biophysical journal* **1996**, 71, 1641.
- [13] B. R. Jennings, K. Parslow, *Proceedings of the Royal Society of London. A. Mathematical and Physical Sciences* **1988**, 419, 137.

## Chapter 3

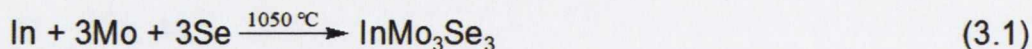
# Synthesis, characterisation and sample preparation of $\text{LiMo}_3\text{Se}_3$ and ion-exchanged $\text{X}^+ \{\text{Mo}_3\text{Se}_3\}^-$

### 3.1 Introduction

$\text{LiMo}_3\text{Se}_3$  can most readily be synthesised via a high temperature ion-exchange reaction.[1] In this chapter, the synthesis and subsequent characterisation of the raw  $\text{LiMo}_3\text{Se}_3$  material by powder X-ray diffraction (PXRD), Energy Dispersive X-ray analysis (EDX) and solubility testing is described. The formation of ion-exchanged  $\text{X}^+ \{\text{Mo}_3\text{Se}_3\}^-$  composites[2], where X is a positively charged organic ligand is also discussed.

### 3.2 Synthesis of $\text{LiMo}_3\text{Se}_3$

The history of the synthesis of  $\text{LiMo}_3\text{Se}_3$  has been described previously (chapter 2). Essentially, an  $\text{InMo}_3\text{Se}_3$  precursor is first formed via the following reaction[3]



Stoichiometric appropriate amounts of the chemicals used<sup>1</sup> were weighed and ground using a pestle and mortar (or cleanly sliced into small pieces using a razor in the case of Indium) before being placed in a quartz ampoule, which was then

---

<sup>1</sup> Aldrich: In (326615) 4N, Mo (366986) 4N, Se (229865) 4N, LiI (62548) > 98% anhydrous

evacuated to approximately  $10^{-5}$  mbar using a rotary-backed turbo pump, which had a cold trap to eliminate any possible back streaming of pump oil into the reaction volume. The ampoule was then sealed under vacuum by heating a constriction in the centre of the glass tubing until the vacuum inside the ampoule caused the neck to gently collapse in on itself (see figure 3.1).

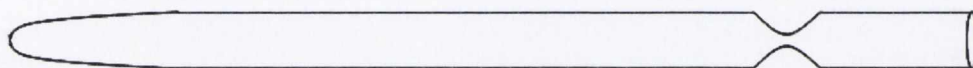
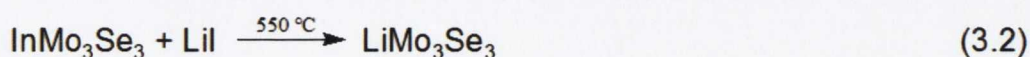


**Figure 3.1:** Quartz ampoule before sealing. Reactants placed at the bottom of the ampoule. Once a suitable vacuum is reached the constriction is heated until it collapses on itself, sealing the ampoule.

The sealed ampoule was then placed in a tube furnace which was heated to 1000 °C at a heating rate of 5 °C per minute and kept at that temperature for 48 hours. After 48 hours the furnace was allowed to cool, the contents thoroughly shaken and was then heated to 1050 °C for a further 24 hours before being allowed to cool slowly over 24 hours.[3] The ampoule was then transferred to a dry Argon glovebox and carefully opened. A small amount of the powder product was removed for analysis and the remainder was weighed and stored in the glovebox. As the  $\text{LiMo}_3\text{Se}_3$  phase is air and moisture sensitive[4, 5] transfer of material to and from the ampoule was all performed within an inert atmosphere (argon) glovebox while all heating was once again performed in evacuated ampoules.

The  $\text{InMo}_3\text{Se}_3$  precursor material was then ion-exchanged via the following reaction to yield  $\text{LiMo}_3\text{Se}_3$ . [3]



The remainder of the  $\text{InMo}_3\text{Se}_3$  was mixed in the glovebox with LiI (in 10% molar excess) using a mortar and pestle. This mixture was then placed in a clean ampoule which was sealed using a quick-fit Teflon valve and removed from the glovebox. The ampoule was evacuated and sealed in the same manner as described above. Once sealed, the ampoule was shaken to ensure all the reactants were at one end and it was placed in a tube furnace with the empty end of the ampoule protruding from the furnace to allow InI and any unreacted LiI to condense. The furnace was heated to 450 °C in 20 minutes and then slowly heated to 550 °C at a rate of 0.1 °C per minute. The reaction was held at 550 °C for seven days, after which it was cooled to room temperature, transferred to the glovebox and then opened. A small amount of the powder product was taken for analysis (PXRD, EDX, solubility). If the product was not deemed to be pure by the analysis methods listed above the ion-exchange reaction (3.2) was repeated. In this case the remainder of the material was mixed with LiI in a 1:1 ratio using a pestle and mortar, placed in an ampoule, the ampoule evacuated and sealed and then refired for a further week. This process was repeated until a satisfactory product was obtained. The product was deemed usable after the following conditions had been met: (1) the XRD lattice parameters matched those reported in the literature, (2) the EDX spectra indicated no, or only trace amounts of, Indium, and (3) stable, deep red solutions were formed when the product was readily dissolvable in polar solvents (e.g. DMSO), without leaving behind particulate deposits. These analyses are described in further detail in the following sections.

The precise yields of  $\text{LiMo}_3\text{Se}_3$  are extremely difficult to establish given that after breaking the ampoule the material must be kept in an oxygen and moisture free environment to avoid oxidation. For one synthesis a yield of approximately 72%

was obtained based on obtaining 0.002069 moles of  $\text{LiMo}_3\text{Se}_3$  (molecular weight 531.64g) product after reacting 0.002869 moles of  $\text{InMo}_3\text{Se}_3$  (molecular weight 639.52g) with LiI.

### 3.3 Characterisation of synthesised $\text{LiMo}_3\text{Se}_3$ materials

#### 3.3.1 PXRD of $\text{LiMo}_3\text{Se}_3$

Powder X-ray diffraction (PXRD) measurements were performed using a Siemens D500 X-ray diffractometer (Cu-K $\alpha$ ,  $\lambda = 1.54178\text{\AA}$ ) to obtain patterns of the  $\text{InMo}_3\text{Se}_3$  intermediate and of the  $\text{LiMo}_3\text{Se}_3$  product. Figure 3.2 shows the diffraction pattern obtained for  $\text{InMo}_3\text{Se}_3$  ( $2\theta$  from  $10^\circ$  to  $60^\circ$ ) compared to the library file for this compound. The d-values of the major peaks are also labeled.

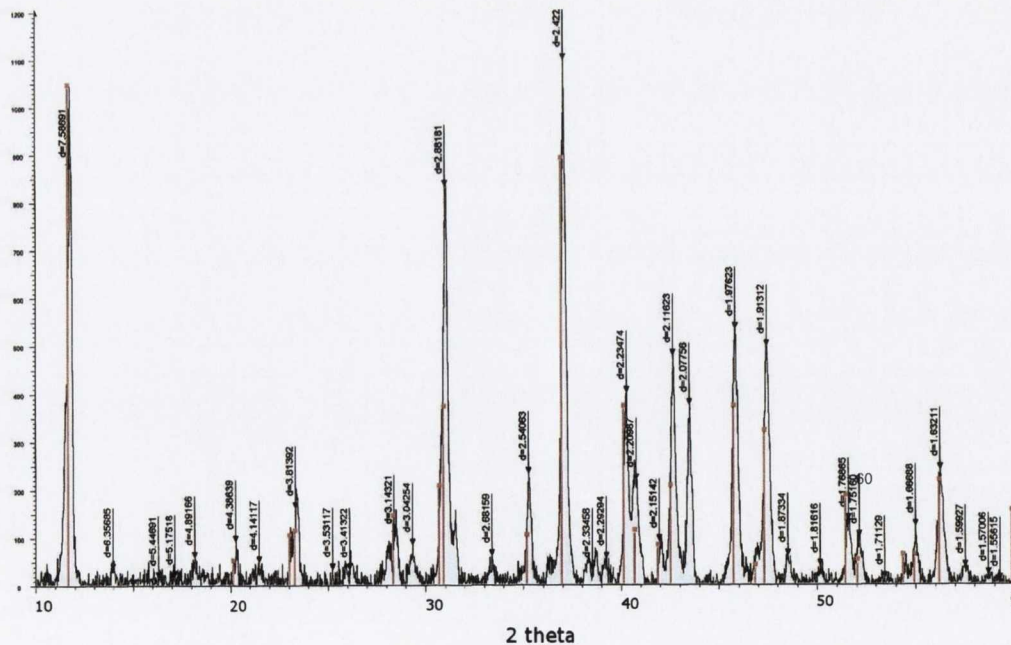


**Figure 3.2:** PXRD pattern of  $\text{InMo}_3\text{Se}_3$  (black) with reference file (red)

The Powder Diffraction File (PDF) 35-1142 was used as the reference.<sup>2</sup>

Table 3.1 below lists the reference and observed experimental d-values for the  $\text{InMo}_3\text{Se}_3$  intermediate. Experimental d-values were calculated using the Bragg scattering equation:

$$n\lambda = 2d \sin \Theta \quad (3.3)$$

| D-values from library file [Å] | Corresponding d-values from observed data[Å] |
|--------------------------------|--|
| 7.62635                        | 7.58691                                      |
| 4.41031                        | 4.38639                                      |
| 3.87643                        | 3.86045                                      |
| 3.82416                        | 3.81392                                      |
| 3.14845                        | 3.14321                                      |
| 2.91429                        | 2.88181                                      |
| 2.88994                        | 2.88181                                      |
| 2.55085                        | 2.54063                                      |
| 2.43062                        | 2.42273                                      |
| 2.24524                        | 2.23474                                      |
| 2.21446                        | 2.20987                                      |
| 2.15552                        | 2.15142                                      |
| 2.12225                        | 2.11623                                      |
| 1.98199                        | 1.97623                                      |
| 1.93751                        | 1.93321                                      |
| 1.91911                        | 1.91312                                      |
| 1.77439                        | 1.76865                                      |
| 1.75590                        | 1.75160                                      |
| 1.68604                        | 1.68108                                      |
| 1.66954                        | 1.66688                                      |
| 1.63479                        | 1.63211                                      |

**Table 3.1:** PXRD experimental and reference d-values for  $\text{InMo}_3\text{Se}_3$

The positions and intensities of the peaks in the experimental pattern match well with the reference. Experimental peaks that lack a counterpart in the library file are

---

<sup>2</sup> Indium Molybdenum Selenide –  $\text{InMo}_3\text{Se}_3$ , Radiation: Cu-K $\alpha$ ,  $\lambda = 1.54178\text{Å}$  (Guinier), System: Hexagonal  $P6_3/m$  (176),  $a = 8.835$  and  $c = 4.492$

likely to result from impurities or unreacted starting materials. However it is apparent that  $\text{InMo}_3\text{Se}_3$  was synthesised due to the good general agreement between the obtained pattern and the library file.

Following from the synthesis of  $\text{InMo}_3\text{Se}_3$ ,  $\text{LiMo}_3\text{Se}_3$  was prepared as summarised above (section 3.2). X-ray diffraction was performed on  $\text{LiMo}_3\text{Se}_3$  in the same manner as for  $\text{InMo}_3\text{Se}_3$ . The experimental pattern for  $\text{LiMo}_3\text{Se}_3$  is shown in red in figure 3.3 below with the  $\text{InMo}_3\text{Se}_3$  pattern (black) included for reference. As there is no PDF file for  $\text{LiMo}_3\text{Se}_3$ , table 3.2 compares our experimentally observed d-spacings to those published by Golden et al.[6] The good agreement between the two sets of values indicates that  $\text{LiMo}_3\text{Se}_3$  was successfully synthesised.

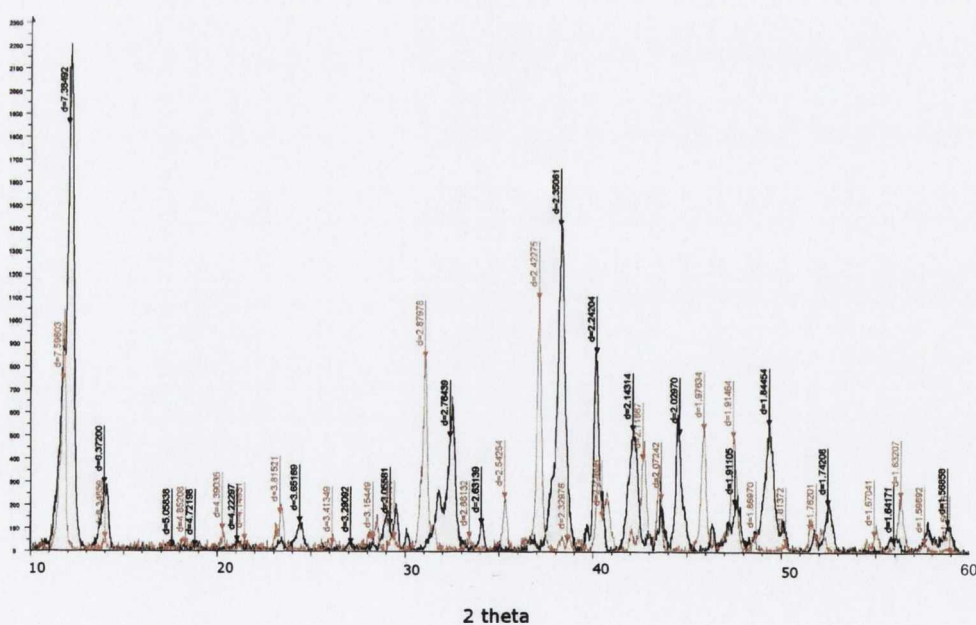


Figure 3.3: PXRD patterns of  $\text{LiMo}_3\text{Se}_3$ (red) and  $\text{InMo}_3\text{Se}_3$ (black)

| D-values from literature[Å] | Observed d-values[Å] |
|-----------------------------|----------------------|
| 7.434                       | 7.38492              |
| 3.705                       | 3.65169              |
| 3.110                       | 3.05581              |
| 2.807                       | 2.76439              |
| 2.376                       | 2.35081              |
| 2.244                       | 2.24204              |
| 2.144                       | 2.14314              |
| 2.053                       | 2.02970              |
| 1.930                       | 1.91105              |
| 1.865                       | 1.84454              |
| 1.752                       | 1.74208              |

**Table 3.2:** *Experimental and literature d-values for  $\text{LiMo}_3\text{Se}_3$  [6]*

### 3.3.2 EDX of $\text{LiMo}_3\text{Se}_3$

To confirm the chemical composition of the synthesised  $\text{LiMo}_3\text{Se}_3$  product, Energy Dispersive X-ray (EDX) analysis was performed using a FEI Strata 235 DualBeam SEM/FIB with EDX. It is important to note that lithium is not observable in either spectrum as a beryllium window is used in the EDX apparatus which prohibits the detection of low Z elements.

A small amount of the  $\text{LiMo}_3\text{Se}_3$  powder product was pressed onto a carbon sticky tab on a SEM sample stub and was taken from the glovebox and transferred to the SEM as quickly as possible to avoid any unnecessary oxidation of the product. EDX analysis of a series of areas was then carried out. Figure 3.4 and 3.5 show the EDX spectra and associated SEM images for two measurements which are representative of all areas examined. The spectrum in figure 3.4 was recorded at a point (labelled with the cross on the image) and the spectrum in figure 3.5 was recorded in the area marked by the red square.



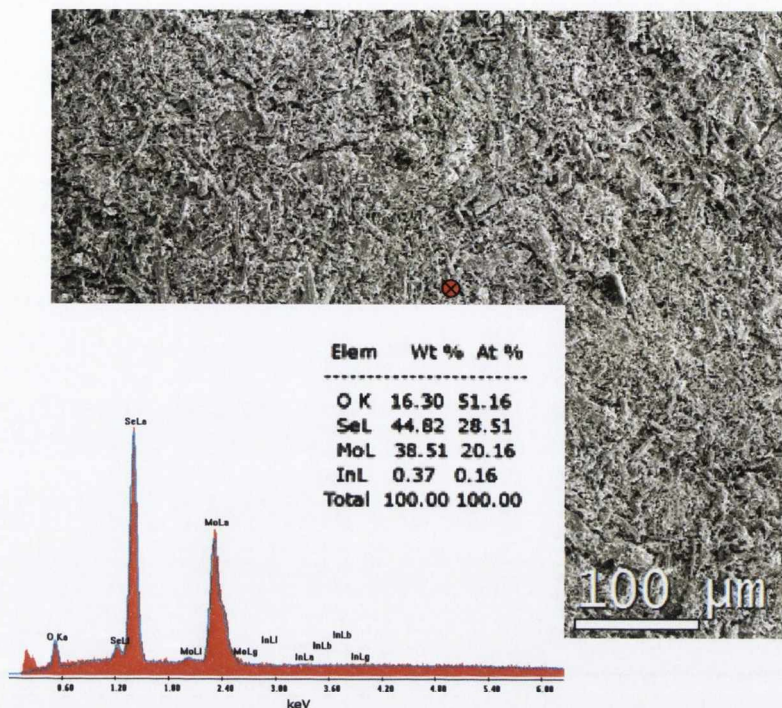


**Figure 3.4:** Inset shows EDX analysis of  $\text{LiMo}_3\text{Se}_3$  material at area marked by the cross on the main SEM image

Low energy peaks in figure 3.4 are due to carbon and oxygen and can both be attributed to the carbon sticky tab. Additionally, some degree of oxidation of the materials during sample transfer may also contribute to the observed oxygen peak. Other than these two peaks, all other peaks correspond to the reactants used and the expected  $\text{LiMo}_3\text{Se}_3$  and InI products. Elemental analysis shows only trace amounts of indium present in the solid material, most likely as a result of InI which is a by-product of the synthesis and is not fully separated from the product at this point. It is possible, however, that this trace In signal is a result of  $\text{InMo}_3\text{Se}_3$  or  $\text{In}_x\text{Li}_{1-x}\text{Mo}_3\text{Se}_3$  which would indicate an incomplete reaction.

Carbon and oxygen are also present in the spectrum taken on the larger area shown in figure 3.5. The SEM image shown is higher resolution than the one presented in figure 3.4 and clearly demonstrates the crystallite nature of the product, shown as

long thick bundles of individual  $\text{LiMo}_3\text{Se}_3$  chains. Elemental analysis shows there to be slightly more indium present in this spectrum than figure 3.4.

It is unlikely that InI is present given the absence of any iodine in the spectra. The presence of  $\text{InMo}_3\text{Se}_3$  is not a major concern given that it is insoluble in polar solvents and no particulate content was noted in solutions of the final product. The possibility of the quaternary phase  $\text{In}_x\text{Li}_{1-x}\text{Mo}_3\text{Se}_3$  is addressed elsewhere in this thesis (section 4.3.2).

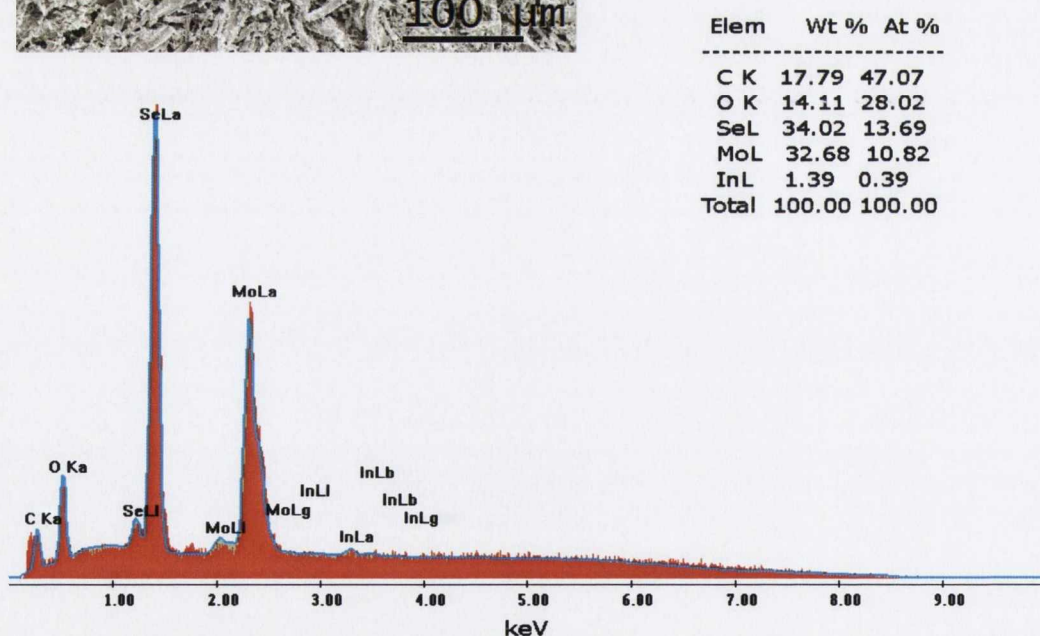
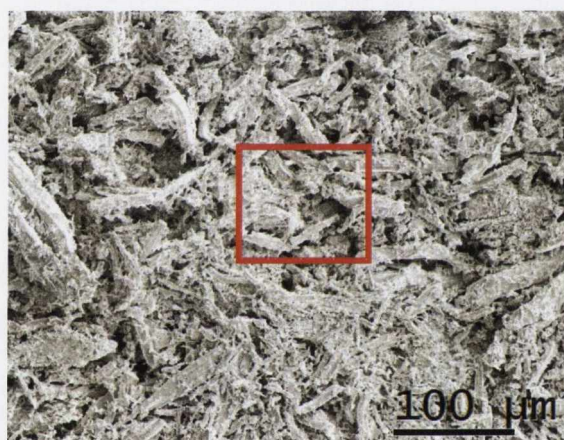
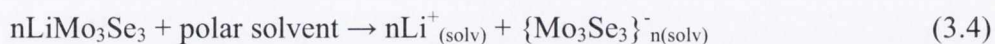


*Figure 3.5 EDX analysis of  $\text{LiMo}_3\text{Se}_3$  material at area marked by the red box on the main SEM image*

### 3.3.3 Solutions of LiMo<sub>3</sub>Se<sub>3</sub>

As mentioned in chapter 1, the lithium phase of the MMo<sub>3</sub>Se<sub>3</sub> compounds is soluble in polar solvents, however the indium phase is not.[4, 7] LiMo<sub>3</sub>Se<sub>3</sub> dissolves in polar solvents due to the high solvation energy of the Li<sup>+</sup> ion, yielding dark red solutions.



In an inert argon atmosphere, a small amount of the solid product from the first exchange reaction of LiI with InMo<sub>3</sub>Se<sub>3</sub> was added to anhydrous dimethyl sulfoxide (DMSO) giving a dark red solution (~10<sup>-4</sup> M). However, small solid particles were seen at the bottom of the vial. This indicated that  $x \neq 1$  for the product In<sub>1-x</sub>Li<sub>x</sub>Mo<sub>3</sub>Se<sub>3</sub> and that further firing with LiI was required. After the second exchange the solubility analysis was repeated. A dark red solution was obtained but with a smaller quantity of solid particles in the bottom of the vial. Once again, more LiI was added and the exchange reaction was repeated. Analysis of this material resulted in a dark red solution in DMSO with no solid present, indicating that the vast majority, if not all, of the indium had been replaced with lithium.

Solutions of different molarities (10<sup>-2</sup> – 10<sup>-6</sup> M) were prepared for successive experiments and stored in the glove box. More concentrated solutions (10<sup>-2</sup>M) have a dark red/brown colour and are highly viscous. Solutions of LiMo<sub>3</sub>Se<sub>3</sub> are highly stable and do not form a precipitate on prolonged storage in an inert atmosphere.

A UV/vis absorbance spectrum of a  $10^{-4}$  M solution in DMSO is shown in figure 3.6. Two absorbance peaks are observed, the maximum absorbance peak with a wavelength of 479 nm and a broader and less intense peak at 317 nm. This is in excellent agreement with the spectrum obtained by Tarascon et al.[4] The dark red colour of  $\text{LiMo}_3\text{Se}_3$  solutions is due to the absorbance of blue light at the wavelengths about the absorbance peaks.

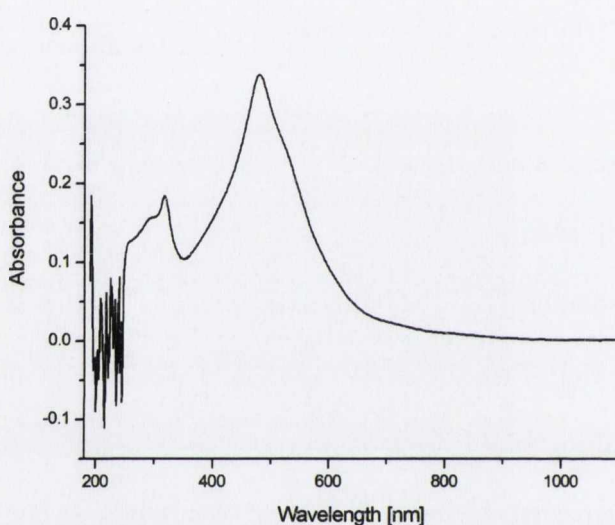


**Figure 3.6** UV/vis absorption spectrum of a  $10^{-4}$  M  $\text{LiMo}_3\text{Se}_3(\text{DMSO})$  solution

While DMSO was the main solvent used during the course of this work, other solvents used to test the solubility of the synthesized compound; including propylene carbonate (PC,  $\text{C}_4\text{H}_6\text{O}_3$ ), N-methylformamide (NMF,  $\text{CH}_3\text{NHCHO}$ ) and water. PC and NMF yield similar solutions to DMSO which remain stable when stored in an argon atmosphere. Water solutions, which were prepared outside the glovebox, were easily formed. However these dark red solutions tended to form precipitates over time due to oxidation between the wire material and the oxygen present in the water.

### 3.4 Preparation of ion-exchanged $X^+ \{Mo_3Se_3\}^-$ using organic ligands

As mentioned in chapter 1, it is possible to replace the  $Li^+$  ion with another cation or positively charged species. The motivation for the preparation of the materials described in this section was to “teflon coat” the  $Mo_3Se_3$  nanowire chains in order to hinder their degradation in moist air.[8] The positively charged ligands used to form ion-exchanged networks are shown with their anion in table 3.3. Their colloquial names (Surf 3, Surf 4, etc. as laid out in the work of Heidelberg et al.[8]) are also listed.

Adding a crown ether (12-Crown-4) and a positively charged ligand ( $X^+$ ) to a  $LiMo_3Se_3$  nanowire solution facilitates the formation of networks of  $X^+(Mo_3Se_3)^-$  nanowire networks.[2] The crown ether and surfactant ligand are added in twofold molar excess relative to the concentration of  $Li^+$  present in the solution. Upon addition, the 12-Crown-4 complexes the  $Li^+$  ion present, removing it from the reaction equilibrium. The positively charged ligands replaces the  $Li^+$  ions on the  $(Mo_3Se_3)^-$  strands (figure 3.7). Once the reaction has completed, the product is removed from its vial, washed in DMSO and stored in a new vial of DMSO.

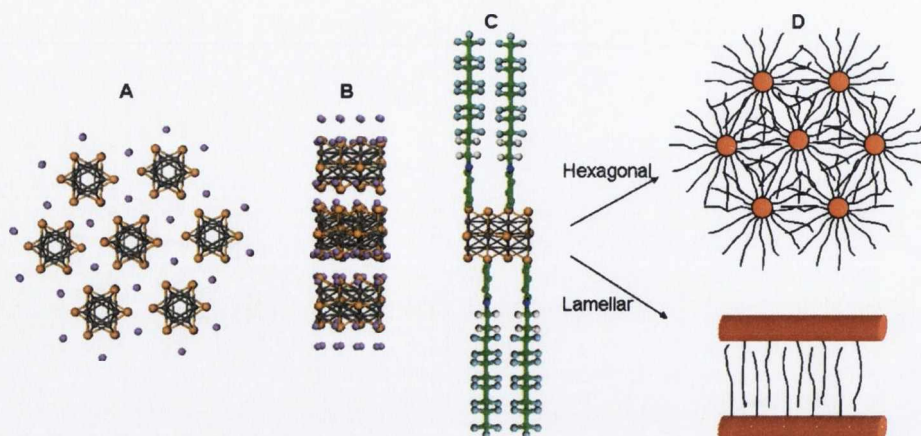
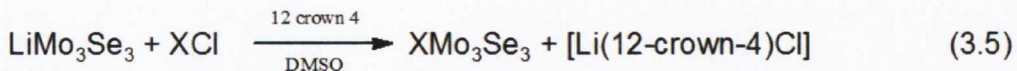


**Figure 3.7:** **A:** Profile view of a ball and stick model of  $\text{LiMo}_3\text{Se}_3$  bundle (Li: purple, Se orange, Mo grey), **B:** Side view of  $\text{LiMo}_3\text{Se}_3$  bundle, **C:**  $\text{Mo}_3\text{Se}_3$  chain after  $\text{Li}^+$  has been complexed by the 12-crown-4. In place of the  $\text{Li}^+$  ion a perfluorinated alkyl chain with a positively charged headgroup (carbon atoms in green) has taken its place on the negatively charged  $\text{Mo}_3\text{Se}_3$ , **D:** resultant hexagonal or lamellar structures

| Name      | Ligand   | Structure |
|-----------|--|-----------|
| Surf 3    | 1-H, 1-H, 2-H, 2-H – Perfluorodecyl-pyridiniumchloride               |           |
| Surf 4    | N', N'- dimethyl – N – (perfluorooctansulfonyl)-piperaziniumchloride |           |
| Surf 5    | 1-(1-Adamntyl)-pyridiniumbromide                                     |           |
| Surf 6    | 1-H, 1-H, 2-H, 2-H, Perfluorooctyl-pyridiniumchloride                |           |
| Surf Thio | 2-Aminoethanthiol Hydrochloride                                      |           |

**Table 3.3:** Ligands, X, used to prepare ion-exchanged  $X^+ \{ \text{Mo}_3\text{Se}_3 \}^-$



This reaction should result in an expansion of the interwire spacing, dependent upon the ligand used, compared to that of a pristine nanowire bundle. Due to the size and low solvation energy of the ligands, the coated nanowire strands no longer remain in solution but instead precipitate, in most cases (bar the thio sample) giving a “seaweed-like” product. The thio samples result in a dense gel, which fully separates from the excess solvent present. This gel can be easily broken apart but, given sufficient time (~1 day), will reform as a dense gel. The detailed characterisation of the ion exchanged materials is described in chapter 7.

### 3.5 Conclusions

LiMo<sub>3</sub>Se<sub>3</sub> was produced by first synthesising an InMo<sub>3</sub>Se<sub>3</sub> intermediate and then performing an ion exchange reaction with LiI. The final product was examined and determined to be LiMo<sub>3</sub>Se<sub>3</sub> by solubility testing, PXRD and EDX analysis.

As per the literature, LiMo<sub>3</sub>Se<sub>3</sub> formed dark red viscous solutions (at higher concentrations) when dissolved in polar solvents. DMSO and PC solutions of the synthesised materials were of the correct colour with no particulate content or precipitate provided the solutions were maintained in an inert atmosphere. However, water solutions degraded over time due to oxidation of the material with the oxygen present in the water.

Powder X-ray diffraction studies show that the intermediate  $\text{InMo}_3\text{Se}_3$  was synthesised due to the good agreement between the experimentally obtained spectrum and the reference Powder Diffraction File. Good agreement was also observed for the d-values of the synthesized  $\text{LiMo}_3\text{Se}_3$  compared to those published by Golden et al.[6]

Energy Dispersive X-ray analysis of the final  $\text{LiMo}_3\text{Se}_3$  product, indicated no impurities present other than carbon and oxygen which were expected. The trace amounts of indium present in the spectra arise from unreacted  $\text{InMo}_3\text{Se}_3$ ,  $\text{InI}$  (a by-product of the synthesis) or an incomplete product, i.e.  $\text{In}_x\text{Li}_{1-x}\text{Mo}_3\text{Se}_3$ .

Ion-exchanged  $\text{X}^+\{\text{Mo}_3\text{Se}_3\}^-$  materials were prepared by replacing the Li counter ions in a  $\text{LiMo}_3\text{Se}_3$  solution with positively charged organic ligands. A crown ether was used to complex the  $\text{Li}^+$  ion to drive the reaction towards the ion-exchanged product. As the organic ligands become inserted into the  $\{\text{Mo}_3\text{Se}_3\}$  nanowire chains the product tends to precipitate. In Chapter 7 we will investigate in detail the structure of these ion-exchanged products

### 3.6 References

- [1] M. Potel, R. Chevrel, M. Sergent, J. C. Armici, M. Decroux, Ø. Fischer, *Journal of Solid State Chemistry* **1980**, *35*, 286.
- [2] B. Messer, J. H. Song, M. Huang, Y. Y. Wu, F. Kim, P. D. Yang, *Advanced Materials* **2000**, *12*, 1526.
- [3] J. M. Tarascon, G. W. Hull, F. J. DiSalvo, *Materials Research Bulletin* **1984**, *19*, 915.



- [4] J. M. Tarascon, F. J. DiSalvo, C. H. Chen, P. J. Carroll, M. Walsh, L. Rupp, *Journal of Solid State Chemistry* **1985**, *58*, 290.
- [5] J. K. Vassiliou, R. P. Ziebarth, F. J. Disalvo, *Chemistry of Materials* **1990**, *2*, 738.
- [6] J. H. Golden, F. J. Disalvo, J. M. J. Frechet, *Chemistry of Materials* **1995**, *7*, 232.
- [7] R. Dronskowski, R. Hoffmann, *Inorganic Chemistry* **1992**, *31*, 3107.
- [8] A. Heidelberg, H. Bloess, J. W. Schultze, C. J. Booth, E. T. Samulski, J. J. Boland, *Zeitschrift Fur Physikalische Chemie-International Journal of Research in Physical Chemistry & Chemical Physics* **2003**, *217*, 573.

## Chapter 4

### Solution cast $\text{LiMo}_3\text{Se}_3$ nanowires and networks

#### 4.1 Introduction

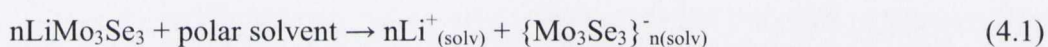
This chapter includes studies of  $\text{LiMo}_3\text{Se}_3$  dissolved in a range of polar solvents, e.g. Dimethyl sulfoxide ( $\text{DMSO}$  ( $\text{CH}_3)_2\text{SO}$ )), N-Methylformamide (NMF ( $\text{CH}_3\text{NHCHO}$ )), deposited onto substrates and studied using a suite of characterization tools (principally atomic force microscopy AFM and electron microscopy). Previous studies of  $\text{LiMo}_3\text{Se}_3$  have reported regular discrete single wires (strands) and nanowire bundles deposited on substrate surfaces from solution [1-6] as well as dense  $\text{LiMo}_3\text{Se}_3$  nanowire mats.[7-10] However, it is important to note that these previous studies do not discuss the precise nature of the wire junctions observed in these as-deposited films.

For the studies described herein, samples were formed by depositing  $\text{LiMo}_3\text{Se}_3$  solutions on a variety of substrates ( $\text{SiO}_2$ , graphite (HOPG), carbon film TEM grids) via drop casting or spin coating followed by vacuum pumping the substrate to evaporate the non-volatile solution. The structure of the deposited nanowire materials were examined by a variety of techniques including AFM and electron microscopy (scanning electron microscopy SEM, scanning transmission electron microscopy STEM, electron energy loss spectroscopy EELS). Cross-sections of  $\text{LiMo}_3\text{Se}_3$  nanowire bundles were prepared by focused ion beam (FIB) milling and

imaged by STEM. Unlike previous reports, the specific attributes of the resultant nanowire junctions are also discussed.

## 4.2 Sample Preparation

$\text{LiMo}_3\text{Se}_3$  is known to dissolve in polar solvents.[11]  $\text{LiMo}_3\text{Se}_3$  crystals are essentially long strands of  $\{\text{Mo}_3\text{Se}_3\}^-$  which is offset by its counter ion,  $\text{Li}^+$ . Furthermore, it has been reported that nanowire diameter is dependent on solution concentration i.e. degree of debundling, and nanowire length is determined by the size of the crystallite prior to dissolution.[12] Figure 4.1 shows a schematic of the structure of  $\text{LiMo}_3\text{Se}_3$  crystals.



For the studies described herein, solutions of  $\text{LiMo}_3\text{Se}_3$  were prepared in an argon environment (glovebox), typically in a 1 mg : 1 ml, material : solvent ratio, yielding a concentration of ~1.8 mM, colloquially referred to as  $10^{-3}\text{M}$ . Lower concentrations ( $10^{-4}\text{M}$ ,  $10^{-5}\text{M}$  etc.) were obtained by dilution of the  $10^{-3}\text{M}$  solution.

Samples were prepared on substrate surfaces by depositing a small amount of solution (typically between 20 and 100  $\mu\text{l}$ ) by drop casting or spin coating. Drop casting was performed by dropping a predefined amount of solution onto the substrate, allowing it a brief period of time (normally two minutes) to stand before vacuum pumping in the glovebox antechamber ( $< -30$  inHg) for at least two hours (but preferably overnight) to remove the non-volatile solution. Deposition by spin coating was performed in the glovebox using a home-built spin coater monitored by

an optical tachometer. Solution volumes of 20  $\mu\text{l}$  - 100  $\mu\text{l}$  were used for spin coating. These samples were also allowed to stand for two minutes and then vacuum pumped overnight in the glovebox antechamber. Any variations to these procedures are directly outlined in the text. The substrates used were highly ordered pyrolytic graphite (HOPG), and  $\text{SiO}_2$ . HOPG was cleaned prior to use by cleaving to reveal a fresh surface layer.  $\text{SiO}_2$  was cleaned by ultrasonic agitation in DI water, acetone and isopropyl alcohol.

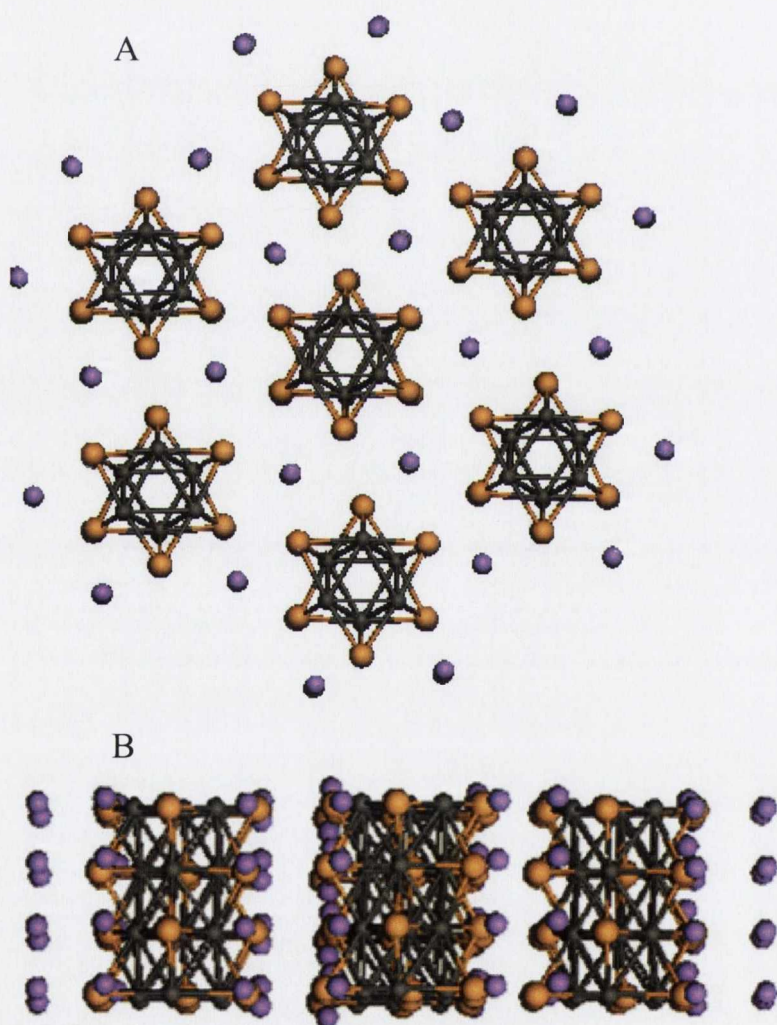


**Figure 4.1:** Schematic of the structure of  $\text{LiMo}_3\text{Se}_3$ , Li: purple, Se: orange, Mo: grey. **A:** profile view of a 7 strand bundle. **B:** side view of the same bundle. Each  $\text{Mo}_3\text{Se}_3$  unit has a charge of -1 which is balanced by the  $\text{Li}^+$  ion. Solid crystals of  $\text{LiMo}_3\text{Se}_3$  are essentially long strands of negatively charged  $\text{Mo}_3\text{Se}_3$  and their counter ions

## 4.3 Results

### 4.3.1 LiMo<sub>3</sub>Se<sub>3</sub> bundles

Figure 4.2A is a TEM image of a large bundle deposited on a holey carbon TEM grid from a  $10^{-3}$  M LiMo<sub>3</sub>Se<sub>3</sub>(DMSO) solution. This is a crystallite which has exfoliated in solution, yielding smaller diameter bundles, and the length of all bundles appears constant. Figure 4.2B is a magnified view of the smaller diameter bundles in figure 4.2A. As these bundles exfoliate from the larger crystallite they overlap and, while there is some entanglement, these bundles are all discrete from one another.

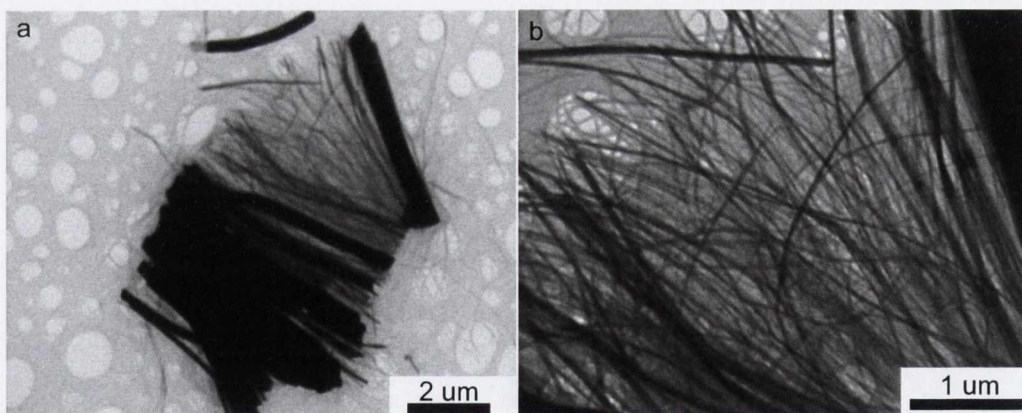


**Figure 4.2:** *A:* TEM image of LiMo<sub>3</sub>Se<sub>3</sub> crystallite deposited on holey carbon film from solution. This crystallite has partially exfoliated in solution. *B* Magnification of image A

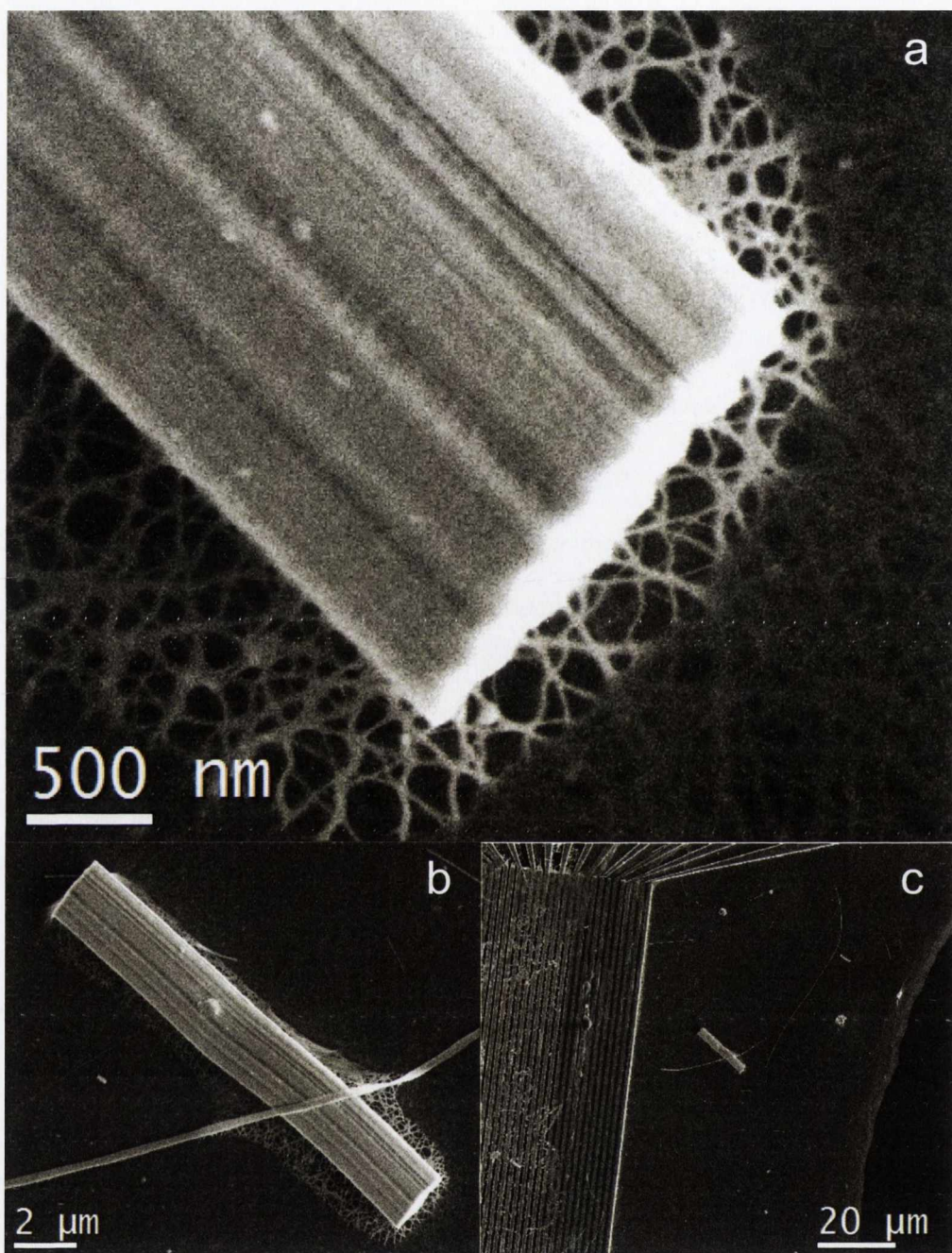


**Figure 4.3:** SEM images of LiMoSe bundles surrounded by LiMo<sub>3</sub>Se<sub>3</sub> network on SiO<sub>2</sub> prepatterned with Au electrodes

Figure 4.3 is a series of SEM images of a large bundle and nanoscale network deposited from a  $10^{-3}$  M LiMo<sub>3</sub>Se<sub>3</sub>(DMSO) solution onto a SiO<sub>2</sub> substrate prepatterned with gold electrodes. Figure 4.3a shows the end of the bundle surrounded by a nanoscale network. Closer examination of the image shows that the network is

present throughout the image, and although low in contrast, the network can be seen spanning over the large bundle. The bright areas of network in the immediate vicinity of the bundle appear bright as they are being raised off the surface by the large bundle beneath them and thus are prone to charging by the electron beam. This indicates that the bundle deposits on the surface first and over time a network is laid down. As the network flattens against the substrate, most of the contrast is lost, however the basic structure of the network can be made out in these areas. Figures 4.3b and 4.3c are demagnified images of the area shown in figure 4.3a. Along the right hand side of figure 4.3c a darker region is visible, this is the bare SiO<sub>2</sub> surface. The droplet of solution deposited on the substrate was centered on the electrode array, and the edge of the droplet “stain” is where the contrast changes on the right hand side of the image. Given the change in contrast and the visible bundles, LiMo<sub>3</sub>Se<sub>3</sub> material is deposited everywhere within this “stain”.

Figure 4.4a is an AFM image (Veeco Dimension 3100 AFM) of large bundles surrounded by network. This sample was formed from 10<sup>-3</sup>M LiMo<sub>3</sub>Se<sub>3</sub>(DMSO) solution spun cast on HOPG, thus demonstrating that the network is present regardless of the substrate. Figure 4.4b is a magnified view of figure 4.4a and more clearly shows the network. Figures 4.4c and 4.4d are similar images of LiMo<sub>3</sub>Se<sub>3</sub> material on HOPG obtained from solutions prepared with NMF as a solvent.

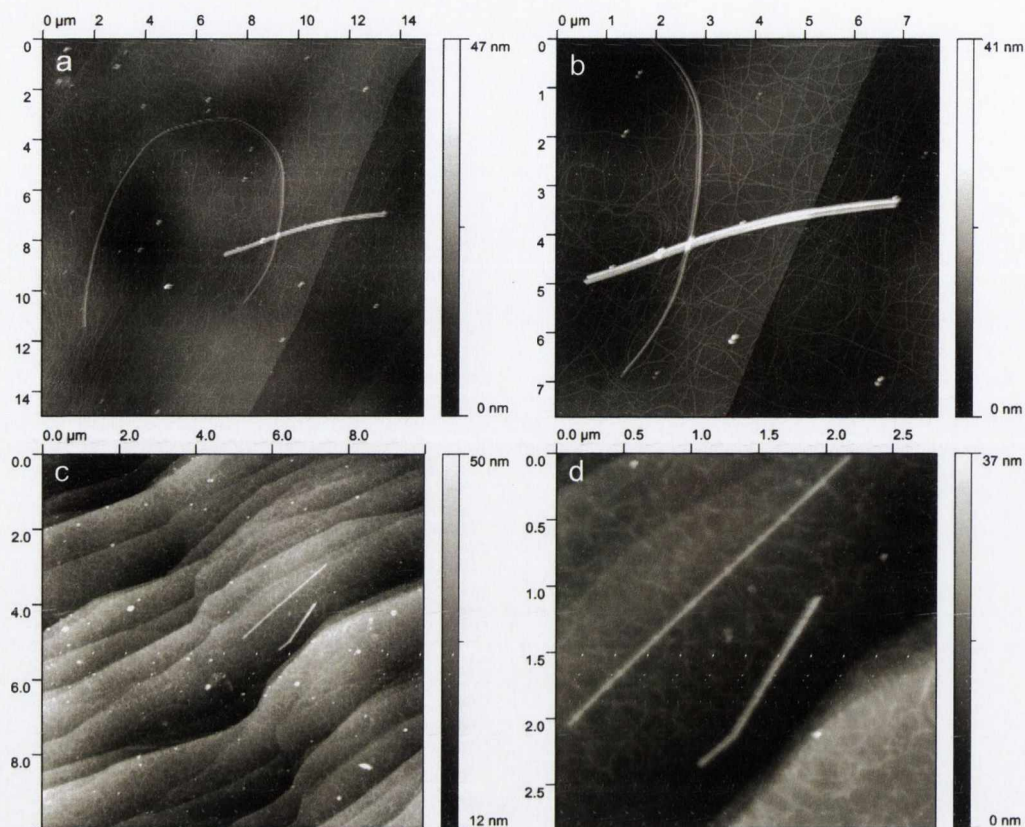


**Figure 4.4:** AFM images of LiMoSe bundles and network on HOPG. *a* and *b*; DMSO solution, *c* and *d*; NMF solution

LiMo<sub>3</sub>Se<sub>3</sub> bundles deposited on Cu grids were also investigated using the SuperSTEM1 system at the Daresbury National Labs, U.K. with Dr. P. Nellist. SuperSTEM1 is a modified VGHB501STEM with a NION Cs corrector, cold field emission filament operating at 100 keV and a Gatan Enfina EEL spectrometer.

Figure 4.5 is a HAADF (high angle annular dark field) STEM image showing a pristine bundle running top to bottom. Seven individual LiMo<sub>3</sub>Se<sub>3</sub> strands are visible along the length of the bundle. The blue rectangle in the image corresponds to the intensity profile shown below the image, and from this, a separation of ~0.75 nm was found.



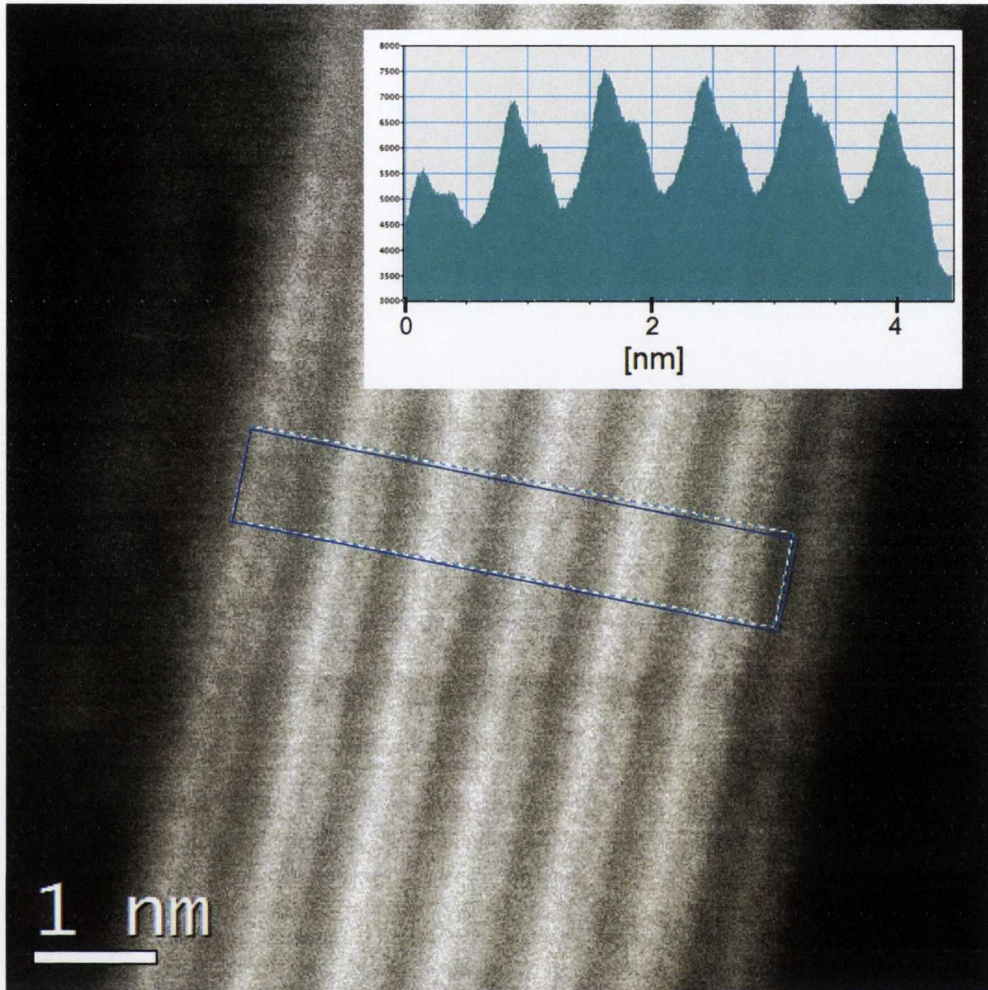


**Figure 4.5:** HAADF STEM image of a  $\text{LiMo}_3\text{Se}_3$  bundle. Profile corresponds to blue box on image. Plane separation is  $\sim 0.75$  nm.

Given the geometry of  $\text{LiMo}_3\text{Se}_3$  bundles (figure 4.1, looking down the bundle axis, strands are stacked ABAB)

$$d = \frac{\sqrt{3}}{2} a \quad (4.2)$$

Where  $a$  is the centre to centre distance, 0.85 nm[13], and thus the estimated values of  $d = 0.736$  nm based on (4.2) above agrees very well with the STEM image.

The HAADF STEM image shown in figure 4.6a was recorded on a 11.2 nm wide  $\text{LiMo}_3\text{Se}_3$  bundle. In this image, the bundle is orientated such that the planes between the  $\text{Mo}_3\text{Se}_3$  units are visible. Figure 4.6b, the intensity profile

corresponding to the larger blue rectangle on the image, gives a separation between these planes of 0.24 nm. From the literature the separation between these planes is 0.25 nm.[13] Figure 4.6c is the profile associated with the smaller blue rectangle on the image. In this instance, individual “dots” are visible along the  $\text{Mo}_3\text{Se}_3$  planes. The separation of these dots is  $\sim 0.25$  nm. From the work of Dronskowski and Hoffman[13] two of the interatomic distances that closely match this number are Mo-Mo = 0.256 nm and Mo-Se = 0.251 nm. The Se-Li interatomic distance is ruled out as at 0.328 nm it is too large and the contrast in HAADF images is based on atomic mass (approximately  $Z^2$ ), therefore Li would not give the degree of contrast seen in the image.

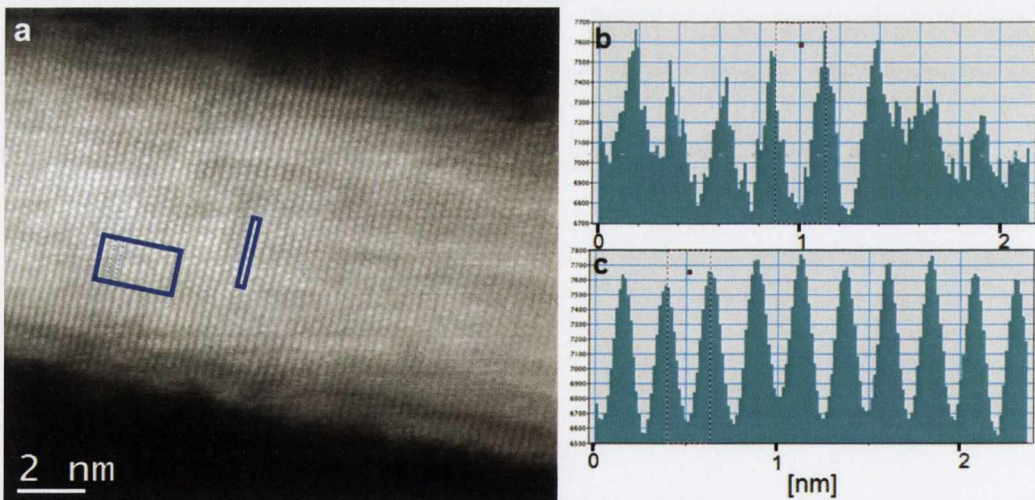


**Figure 4.6:** HAADF STEM image of  $\text{LiMo}_3\text{Se}_3$  bundle. Profiles (b and c) correspond to blue boxes on image

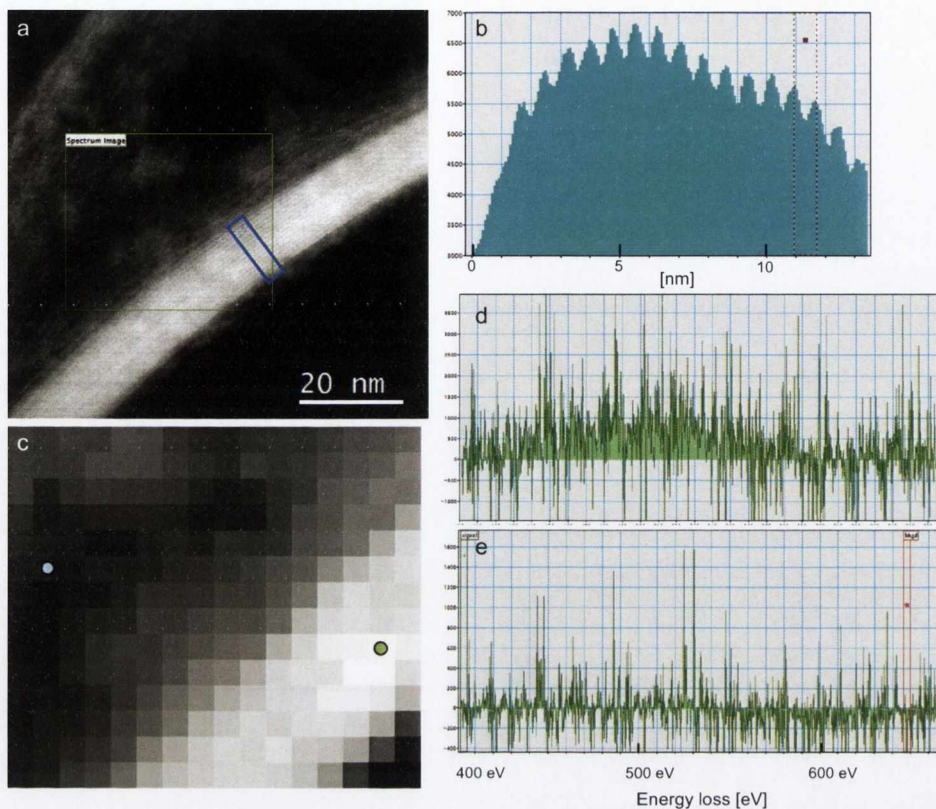


**Figure 4.7a:** HAADF STEM image of LiMoSe bundle, **b:** profile corresponds to blue box on image, **c:** spectrum image corresponding to the green box on the image, **d** and **e:** EEL spectra corresponding to the green and blue dots respectively

Figure 4.7a is a HAADF STEM image of a  $\text{LiMo}_3\text{Se}_3$  bundle flanked by some  $\text{LiMo}_3\text{Se}_3$  network. The blue rectangle corresponds to the profile (figure 4.7b) and yields a separation of 0.79nm which agrees with the value for the separation of wire planes of 0.74nm obtained from equation (4.2). Figure 4.7c is an EEL spectrum image which corresponds to the green rectangle on the image. Each pixel of the spectrum image represents the area under the curve of the EEL spectrum in the energy range 490-530 eV. This energy range was chosen since the Mo M1 edge is located at 505 eV. Figure 4.7d and 4.7e are the spectra corresponding to the pixels marked with green and blue dots, respectively. The contrast in the spectrum image is thus correlated to the presence of Mo in the area of the STEM image bordered by the green rectangle.

To further investigate the difference between large pristine bundles and the surrounding network material, cross-sections of a  $\text{LiMo}_3\text{Se}_3$  bundle were prepared by deposition on a  $\text{SiO}_2$  substrate from a  $10^{-3}\text{M}$  solution. Following deposition, the sample was coated with 50 nm of  $\text{SiO}_2$  and 50 nm of Au in a high-vacuum sputter coater. Thin ( $< 100$  nm thick) sections were prepared in a dual-beam SEM/FIB by first depositing a thin Pt band and then milling pits on either side of the band. Once the sections were sufficiently thin, they were transferred to a TEM grid using an in-situ Kliendiek micromanipulator system. These sections were imaged in SEM mode in the dual-beam system and high resolution S/TEM measurements were carried out on a Hitachi HD-2300 by Dr. Richard Langford during an evaluation visit to Hitachi Japan.

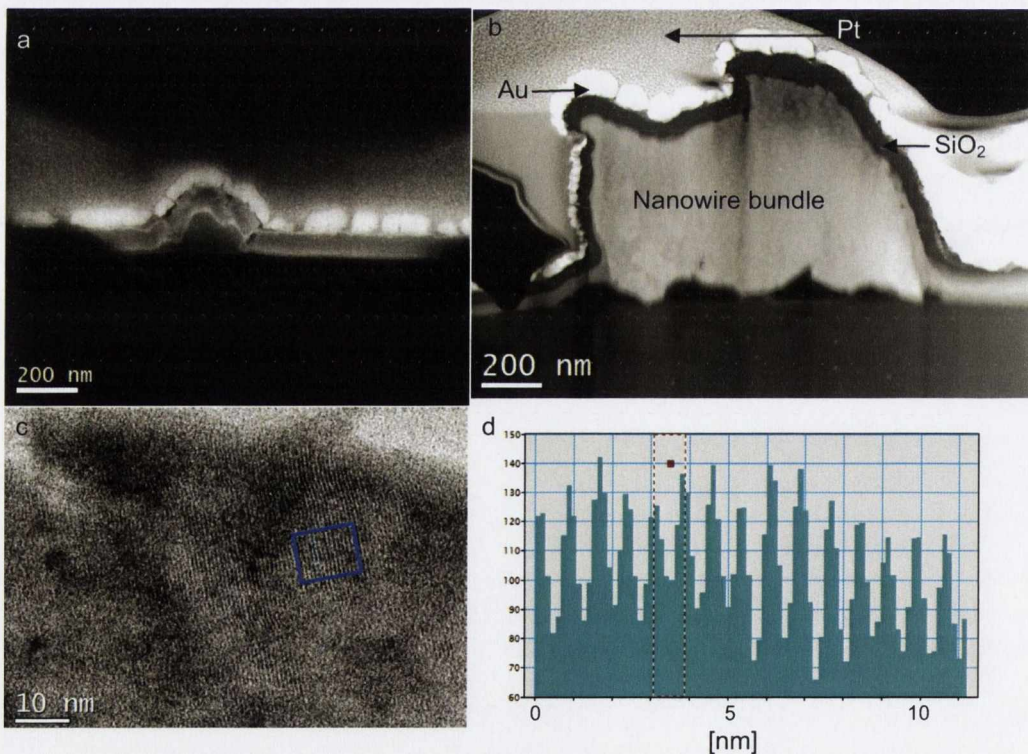


**Figure 4.8a:** SEM image, **b** and **c:** Z contrast STEM images, of cross sections of  $\text{LiMo}_3\text{Se}_3$  bundles. Protective Pt, Au and  $\text{SiO}_2$  layers are labeled on **b**. **d:** Profile corresponds to blue box on image

Figure 4.8 shows two cross-sections of two different bundles prepared in this manner. The smaller bundle (figure 4.8a) is imaged in SEM mode and the larger bundle (figure 4.8b) imaged in Z contrast STEM mode (HAADF). It is apparent that these large bundles do not display a cylindrical cross-section. The presence of voids between the bundle and the substrate should also be noted. Figure 4.8c shows a magnified view of figure 4.8b in which the planes of the  $\text{LiMo}_3\text{Se}_3$  strands in the bundle are visible. The profile (figure 4.8d) corresponds to the blue rectangle and gives a separation of 0.8 nm (c.f. 0.74 nm, equation 4.2)).

In summary large bundles deposit from the  $\text{LiMo}_3\text{Se}_3(\text{DMSO})$  solution onto substrate surfaces. These bundles are highly crystalline and STEM imaging shows that the  $\text{Mo}_3\text{Se}_3$  unit separation and interwire separation in these bundles agrees well with the literature. The cross-sectional analysis shows these bundles have a non-cylindrical geometry with voids present between the bundle and the substrate. This indicates that these highly crystalline bundles are present in the solution as small pieces of the original material. Networks are also observed with large crystalline bundles, often coating them, indicating that networks are laid down over time whereas the large crystallites deposit quickly.

### 4.3.2 $\text{LiMo}_3\text{Se}_3$ networks

Figure 4.9 shows a representative AFM image of a  $\text{LiMo}_3\text{Se}_3$  nanowire network on a HOPG substrate surface. The sample was formed by spin-coating a  $\text{LiMo}_3\text{Se}_3(\text{DMSO})$  solution onto a freshly exposed graphite layer in a glovebox. The sample was vacuum pumped overnight and then imaged with a Veeco Dimension 3100 AFM system using Tapping Mode<sup>TM</sup> in ambient conditions. The image shows a flat two

dimensional network which spans the entire of the area of the image (networks with areas of up to 100  $\mu\text{m}$  per side have been observed). The image shows  $\text{LiMo}_3\text{Se}_3$  nanowires ranging in height from 0.7 nm (a single wire strand) to 5 nm. Line-profile 1 shows a distribution of wires from  $\sim 1$  nm to  $\sim 4$  nm in the centre of the image. There are no large bundles apparent in this network. Junctions do not appear to show a marked increase in height, however some lateral spreading can be seen in the image. The junction in the centre right of the image (inset shows an enlarged view) shows eight wires converging to a single junction point. As can be seen from line profiles 2-5, the junction height is  $\sim 5.2$  nm and the surrounding wires have heights of 3.6 nm, 2.6 nm, 2.1 nm, 4.9 nm, 3.9 nm, 2.8 nm, 4.3 nm and 3.8 nm. It is immediately apparent that, even if the junction is formed from four overlapping wires (thus 8 wires extending out from the junction point) and all four wires had a height equivalent to the smallest wire measured, the height of the junction should considerably exceed the observed height of 5.2 nm.

Energy-dispersive X-ray spectroscopy (EDX) measurements of a  $\text{LiMo}_3\text{Se}_3$  networked material recorded using a FEI F20 are shown in figure 4.10. The red dot on the image corresponds to the location at which the measurement was taken. The EDX spectrum shows the presence of selenium and molybdenum. Carbon and copper peaks are due to the TEM grid. A trace amount of indium peaks are visible (the L series lines for indium are between 3.3 and 4.1 eV).

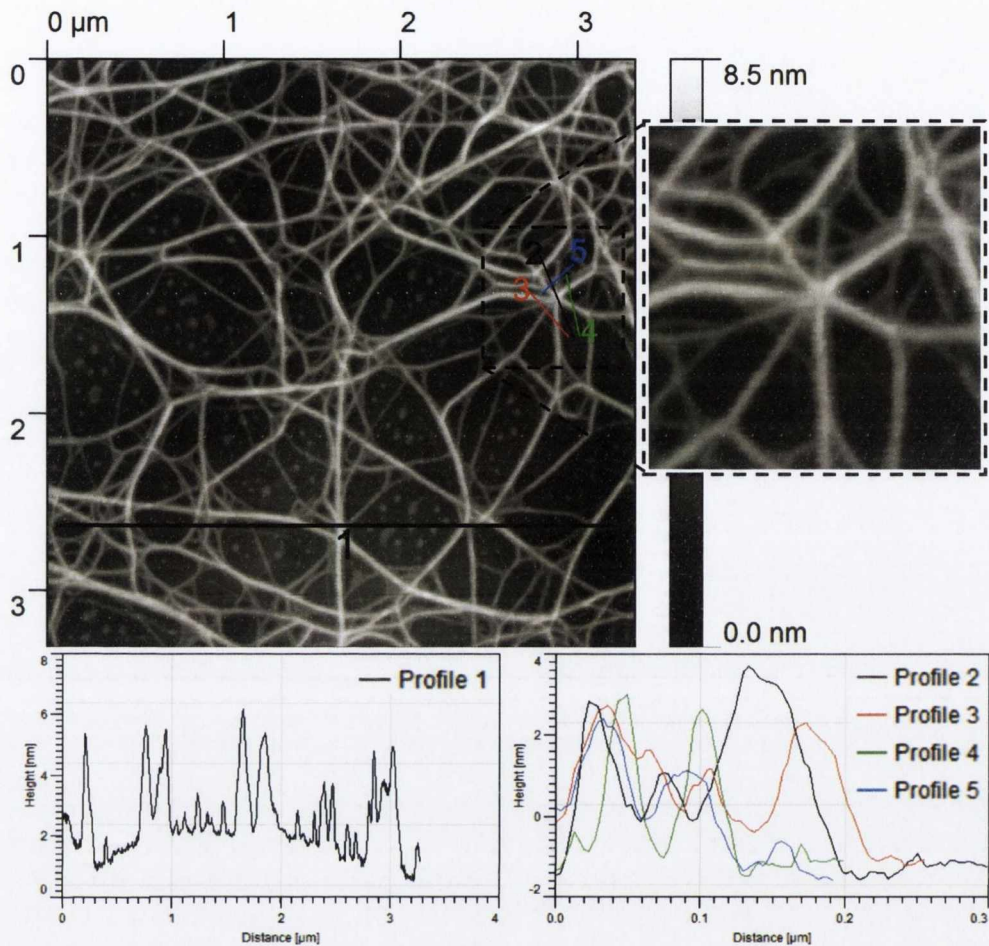


**Figure 4.9:** AFM image of a network of  $\text{LiMo}_3\text{Se}_3$  cast from DSMO solution onto HOPG with line profiles.

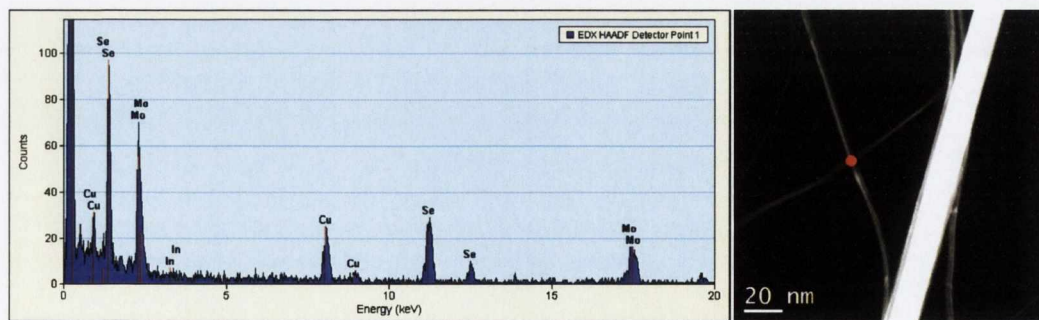


**Figure 4.10:** EDX spectrum obtained from a  $\text{LiMo}_3\text{Se}_3$  network marked by the red dot on the image

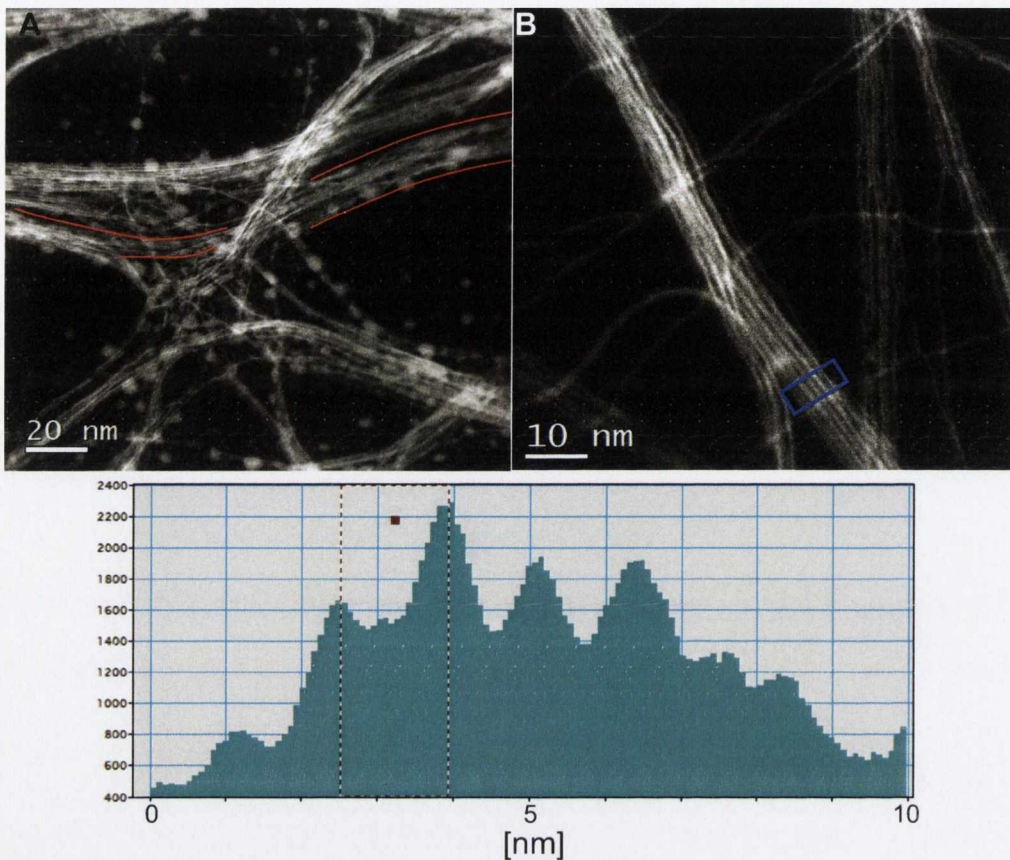


**Figure 4.11:** HAADF STEM images of a network junction (a) and a forking nanowire junction (b) Profile corresponds to blue box on image

Figure 4.11a is a STEM image which confirms that network junctions do not consist of nanowires bridging or running side by side before diverging again. Rather, junctions form an “inter-exchange”, i.e. strands from one wire entangle with strands from another wire forming a junction. The wire in figure 4.11a framed by the orange lines is a good example of this as the portion of the wire to the left of the junction does not have as many constituent strands as the portion to the right. The image in figure 4.11b shows a small wire which forks at the bottom of the image, a feature often observed in these network junctions. From the profile, corresponding to the blue box in figure 4.11b, the measured separation of individual strands in this section of the network is 1.18 nm indicating that the constituent strands that make up networked materials are not as strongly coupled as they are in large crystalline



bundles such as those seen in figure 4.5 where the separation is  $\sim 0.75$ nm. This may also indicate that the networks assemble on surfaces (after the deposition of larger crystalline bundles, figure 4.3) from individual  $\text{LiMo}_3\text{Se}_3$  wires, rather than the case where these networked materials are present fully formed in solution.

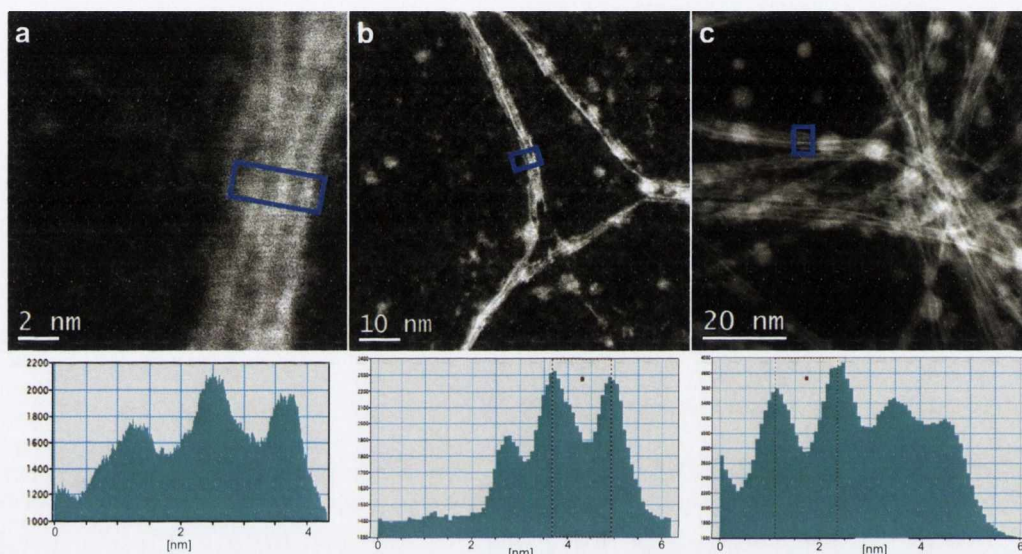


**Figure 4.12a-c:** HAADF STEM images of  $\text{LiMo}_3\text{Se}_3$  nanowire network junctions. Profiles correspond to blue boxes on image

Figure 4.12a-c shows STEM images of  $\text{LiMo}_3\text{Se}_3$  wires which are part of networks. This is most clearly seen in figures 4.12b and 4.12c where junctions can be seen. It is apparent that the junctions in figure 4.12b are not formed of overlapping wires. The spots on the network in figure 4.12c are similar to those seen by Qi et al[14] and are caused by solvent. Below each image is the profile obtained from the areas shown by the blue rectangles. The wire separations for figures 4.12a, 4.12b and 4.12c are 1.14 nm, 1.25 nm and 1.25 nm respectively.

Electron Energy Loss Spectroscopy (EELS) was recorded for both network and crystalline bundle samples at the SuperSTEM facility. As previously discussed

$\text{LiMo}_3\text{Se}_3$  is synthesized by first preparing  $\text{InMo}_3\text{Se}_3$  and then performing an ion exchange reaction with  $\text{LiI}$  (Section 3.2).

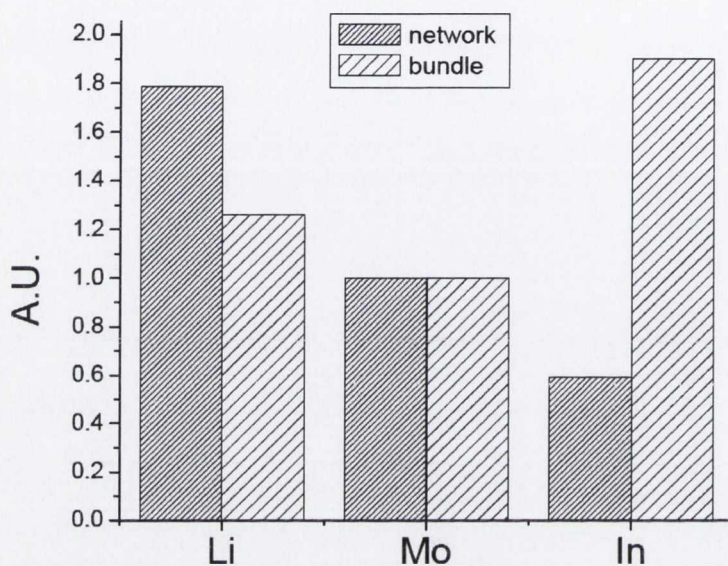
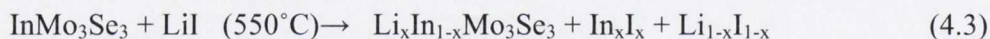


**Figure 4.13:** areas of Li and In edges relative to the normalized Mo edge obtained from EELS data of  $\text{LiMo}_3\text{Se}_3$  network and bundle



For a single  $\{\text{Mo}_3\text{Se}_3\}$  unit with a charge of -1, the concentrations of Mo and Se are constant. The negatively charged  $\{\text{Mo}_3\text{Se}_3\}$  unit is balanced by a positive ion, either Li or In. From the EELS spectra, the areas beneath the Mo, Li and In edges were obtained and normalized relative to  $\text{Mo} = 1$  for both large crystalline bundles and networks. Figure 4.13 shows a histogram of these electron energy loss edge areas. It is apparent that both bundles and networks are still of the form  $\text{Li}_x\text{In}_{1-x}\text{Mo}_3\text{Se}_3$ , with the large crystallites being In “rich” and the network material being much more reacted and closer to pure  $\text{LiMo}_3\text{Se}_3$ . These observations can be attributed to the fact

that the  $\text{InMo}_3\text{Se}_3$  phase is not soluble, therefore these larger crystallites are not fully dissolved

(for pure  $\text{LiMo}_3\text{Se}_3$  in solution;  $n\text{LiMo}_3\text{Se}_3 + \text{polar solvent} \rightarrow n\text{Li}^+ + \{\text{Mo}_3\text{Se}_3\}^-_n$ ).

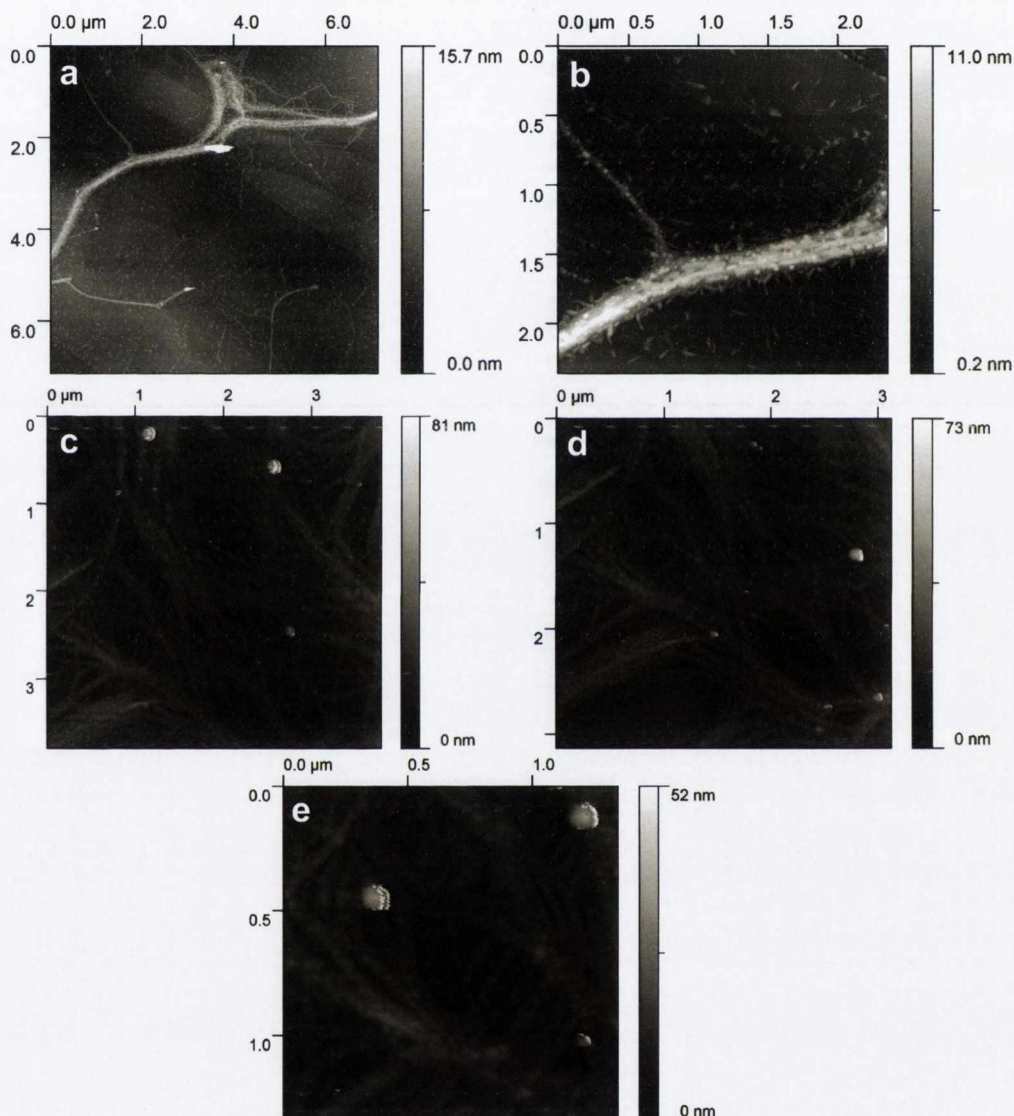


**Figure 4.14a-e:** AFM images of  $\text{LiMo}_3\text{Se}_3$  networks with small wire fragments due to rapid vacuum pumping of sample

Figures 4.14a-e show AFM images of  $\text{LiMo}_3\text{Se}_3(\text{DMSO})$  cast onto HOPG substrates. However in this case, rather than allowing the sample time to stand after the solution was deposited, the sample was immediately vacuum pumped following solution

application. In these images, in addition to wires and junctions, it is observed that the substrate surface is highly speckled. Figure 4.14b is a zoom in on the junction in figure 4.14a and shows small fragments ( $\sim 100$  nm long,  $\sim 2$  nm high) scattered about the wire junction in the centre of the image. They are most concentrated about the edge of the wire itself, and appear to be aligning with the wire junction. Figures 4.14c,d and e, are similar images from a different sample prepared in the same manner. Again small fragments are observed surrounding the nanowire junctions.

## 4.5 Conclusion

The combination of AFM, SEM, and STEM data presented herein shows the formation of  $\text{LiMo}_3\text{Se}_3$  nanowires and nanowire networks when solutions of  $\text{LiMo}_3\text{Se}_3$  dissolved in DMSO or NMF, are deposited on  $\text{SiO}_2$ , HOPG and carbon film TEM grids. STEM analysis of the large crystalline bundles shows that the synthesis of the nanowire material was successful and that the interwire distances and inter  $\text{Mo}_3\text{Se}_3$  planar distances are consistent with the literature. TEM imaging of FIB prepared cross-sections revealed that nanowire bundles exhibit a non-cylindrical cross-sectional geometry with voids between the bundle and substrate. This observation indicates that the large crystalline bundles are not formed on the substrate surfaces in which case it would be expected that the bundle would be flush with the surface. This observation further suggests the possibility that these large bundles are present in solution as small pieces of the original materials.

Large crystalline bundles and nanowire networks are seen to coexist side by side. As seen in figure 4.3, the network spans the crystalline bundle, indicating that large

bundles settle on the surface first and that networks are then laid down on top of them.

The characteristics of nanowire networks and junctions within these networks were also analysed. AFM studies of nanowire networks showed that network height displays a high degree of monodispersity and that junctions are not formed from overlapping wires. STEM imaging of nanowire networks showed that junctions in these networks are formed by the constituent strands splaying out in different directions forming a nanowire “interexchange” rather than overlapping wires giving rise to junctions. Individual strands in these network “arms” are separated by distances on the order of 1.2nm, which has not been observed previously, indicating a structural difference between bundles and networks in terms of how their component  $\text{LiMo}_3\text{Se}_3$  strands stack next to each other.

A comparison of EELS data of both nanowire network and nanowire bundles was undertaken to investigate any difference between the two. This showed that crystalline bundles contain more In than the material which forms network. This indicates that in the case of large bundles, the ion exchange reaction was incomplete and these bundles have a stoichiometry of  $\text{Li}_x\text{In}_{1-x}\text{Mo}_3\text{Se}_3$ . From this it seems likely that large crystallites exist as undissolved or partially dissolved species in solution (as the In phase is insoluble), resulting in large bundles which deposit on substrate surfaces. This is further supported by the voids apparent between the substrate surface and bundle in the cross-sectional images.

To investigate the effect of solvent evaporation on network formation, experiments conducted by decreasing the length of time the solutions were allowed to stand on the substrate by vacuum pumping immediately following application in order to remove the non-volatile solvent. This yielded AFM images of network with small fragments ( $\sim 100$  nm long,  $\sim 2$  nm high) speckling the surface. These fragments appear to line up along the nanowire network indicating that networks may be actually formed by small wires and fragments aligning on the network “skeleton”. This “skeleton” is formed by small wires splaying out and forming inter-exchanges.

These conclusions raise the important question of what is actually present in a  $\text{LiMo}_3\text{Se}_3$  solution? It seems likely that large ( $> 50$  nm laterally) bundles are present as undissolved or partially dissolved crystallites. Smaller wires which exfoliate from these larger crystallites may also be present (figure 4.2). Networks consist of small ( $< 10$ nm laterally) wires which splay out and form network junctions over large areas. It also seems likely that small ( $\sim 100$  nm long,  $\sim 2$  nm high) fragments, seen when the solution is immediately vacuum pumped following drop casting, are also present in solution and ultimately align with these small wires. These resulting networks are highly uniform, have a small distribution of heights of the constituent wires, and show lateral spreading of the junction rather than a marked increase in junction height as demonstrated by the AFM data (figure 4.9). It is unclear whether these networks are fully formed in solution (in which case they would just lay down on the surface), or if they form when the solution is deposited on a surface. Given that the inter-wire separation in a network is greater than that of a large crystalline bundle these structures are unlikely to be present in solution and it would seem that solvent evaporation on substrate surfaces drives the assembly.

Networks of discrete nanoscale objects can assemble upon solvent evaporation as seen in the case of isotropic nanoparticles[15, 16] and anisotropic nanowires[17]. An important distinction to be drawn between the MoSI nanowire networks of Mihalovic et al and the  $\text{LiMo}_3\text{Se}_3$  networks examined here is that the MoSI networks are formed of overlapping or criss-crossing individual wires whereas the networks described here contain junction points which are composed of forked wire bundles, where the constituent wire strands of these bundles are shared between the “arms” of the network (figure 4.11).

In chapter 5 we will investigate the composition of  $\text{LiMo}_3\text{Se}_3$  solutions by means of rheometry and dynamic light scattering studies of the solutions and cryo-TEM imaging (chapter 7) of frozen sections of  $\text{LiMo}_3\text{Se}_3$  solution.

## 4.6 References

- [1] L. Venkataraman, C. M. Lieber, *Physical Review Letters* **1999**, 83, 5334.
- [2] L. Venkataraman, Y. S. Hong, P. Kim, *Physical Review Letters* **2006**, 96, 76601.
- [3] B. Messer, J. H. Song, M. Huang, Y. Y. Wu, F. Kim, P. D. Yang, *Advanced Materials* **2000**, 12, 1526.
- [4] B. Messer, J. H. Song, P. D. Yang, *Journal of the American Chemical Society* **2000**, 122, 10232.
- [5] J. H. Golden, F. J. Disalvo, J. M. J. Frechet, *Chemistry of Materials* **1995**, 7, 232.

- [6] F. E. Osterloh, J. S. Martino, H. Hiramatsu, D. P. Hewitt, *Nano Letters* **2003**, 3, 125.
- [7] M. D. Hornbostel, S. Hillyard, J. Silcox, F. J. DiSalvo, *Nanotechnology* **1995**, 6, 87.
- [8] J. M. Tarascon, F. J. DiSalvo, C. H. Chen, P. J. Carroll, M. Walsh, L. Rupp, *Journal of Solid State Chemistry* **1985**, 58, 290.
- [9] M. Allen, E. M. Sabio, X. B. Qi, B. Nwengela, M. S. Islam, F. E. Osterloh, *Langmuir* **2008**, 24, 7031.
- [10] X. B. Qi, F. E. Osterloh, J. A. Giacomo, S. Chiang, *Langmuir* **2006**, 22, 8253.
- [11] J. M. Tarascon, G. W. Hull, F. J. DiSalvo, *Materials Research Bulletin* **1984**, 19, 915.
- [12] M. Potel, R. Chevrel, M. Sergent, *Acta Crystallographica Section B-Structural Science* **1980**, 36, 1545.
- [13] R. Dronskowski, R. Hoffmann, *Inorganic Chemistry* **1992**, 31, 3107.
- [14] X. B. Qi, F. E. Osterloh, S. A. Barriga, J. A. Giacomo, S. Chiang, *Analytical Chemistry* **2006**, 78, 1306.
- [15] E. Rabani, D. R. Reichman, P. L. Geissler, L. E. Brus, *Nature* **2003**, 426, 271.
- [16] P. Moriarty, M. D. R. Taylor, M. Brust, *Physical Review Letters* **2002**, 89, 248303.
- [17] B. Bercic, U. Pirnat, P. Kusar, D. Dvorsek, D. Mihailovic, D. Vengust, B. Podobnik, *Applied Physics Letters* **2006**, 88, 173103.



## Chapter 5

# Characterization of solutions of $\text{LiMo}_3\text{Se}_3$ dissolved in dimethyl sulfoxide

### 5.1 Introduction

The data presented in the previous chapter of  $\text{LiMo}_3\text{Se}_3$  materials deposited from solution suggest that the composition of  $\text{LiMo}_3\text{Se}_3$  in solutions is important in understanding the origin of nanowire bundles and networks. In order to elucidate the formation mechanisms of these networks, the composition of  $\text{LiMo}_3\text{Se}_3$  solutions was examined using rheology and dynamic light scattering.

From the AFM images of samples that were prepared by drop casting a quantity of solution on substrate surfaces and immediately vacuum pumping (figure 4.14), small wire fragments were observed lining up on the network frame. The cross-sectional TEM images of large  $\text{LiMo}_3\text{Se}_3$  bundles (figure 4.10) show an irregular non-cylindrical geometry with voids between the nanowire bundle and the substrate. From this it seems that larger bundles are discrete entities but small oligomers in solution may be responsible for network growth. The question now is: are the observed nanowire networks pre-formed in solution or do they assemble from solution onto the substrate surface.

To examine this hypothesis we have undertaken a rheometry and Dynamic Light Scattering (DLS) study of a range of  $\text{LiMo}_3\text{Se}_3(\text{DMSO})$  solutions. Optical spectroscopy (UV-vis) and DLS studies of oxidising solutions are also presented.

## 5.2 Characterisation

### 5.2.1 Rheometry of $\text{LiMo}_3\text{Se}_3(\text{DMSO})$ solutions

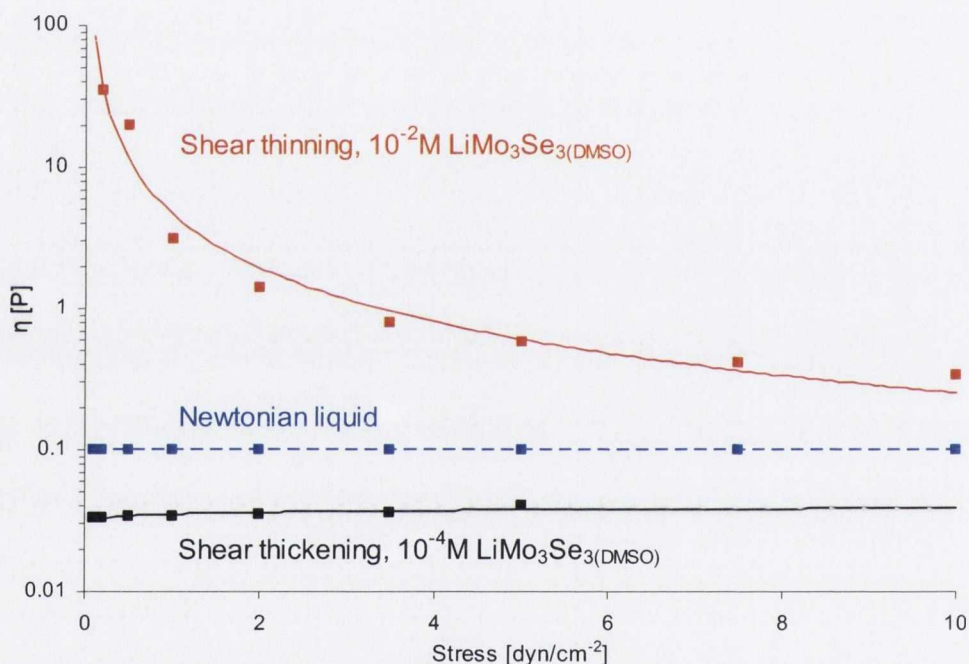


**Figure 5.1:** Rheology for  $10^{-2}$  M and  $10^{-4}$  M  $\text{LiMo}_3\text{Se}_3(\text{DMSO})$  solutions showing shear thinning at higher concentrations and shear thickening at lower concentrations.

Rheology data recorded for  $\text{LiMo}_3\text{Se}_3(\text{DMSO})$  solutions was obtained using a Rheometric Scientific SR 2000 instrument, in the laboratory of Prof. Earle Waghorne, UCD, Ireland. Measurements were carried out on a series of  $\text{LiMo}_3\text{Se}_3(\text{DMSO})$  solutions with concentrations ranging from  $10^{-2}$  to  $10^{-6}$  M. In figure 5.1 the obtained results for a  $10^{-2}$  M and a  $10^{-4}$  M solution are plotted as viscosity

(units: poise,  $P, = 0.1 \text{ kgm}^{-1} \text{ s}^{-1}$ ) vs. the applied shear stress (units: dyne,  $\text{dyn}, = 10^{-5} \text{ N}$ ). The dashed line shows the behaviour of a Newtonian liquid (i.e. its viscosity is independent of the applied stress).  $\text{LiMo}_3\text{Se}_3(\text{DMSO})$  exhibits shear thickening and at lower concentrations exhibits shear thinning at higher concentrations. For lower concentration samples the increase in viscosity with increasing shear stress can be explained by the entanglement of the colliding particles in solution (shear thickening). Shear thinning is observed for higher concentrations, the viscosity decreases with increasing shear stress as the particles have less space to move in solution and start to align with the flow direction due to the applied stress. This behaviour is consistent with one dimensional wire-like particles in solution. This can be likened to the analogy of logs floating down a river, the fewer logs the more room there is for them to revolve and entangle (shear thickening) but with a higher density of logs floating on the river they tend to line up together (shear thinning).

### 5.2.2 Dynamic Light Scattering

Dynamic Light Scattering, DLS, measures Brownian motion and relates this to the particle size in solution. Larger particles diffuse slower than smaller particles. In DLS the speed at which the particles are diffusing is measured by recording the rate of the variation of the intensity of the scattered light. [1] The correlation between measurements in a fluctuating signal is determined using a correlation function. The correlation of the signal will decay quicker for motion due to small particles than for large particles.

The size of the particle is described using the Stokes-Einstein relation [2, 3]:

$$D = \frac{kT}{f} = \frac{kT}{6\pi\eta R_H} \quad (5.1)$$

Where  $D$  is the translational diffusion coefficient,  $k$  is the Boltzmann constant,  $T$  is the absolute temperature,  $f$  is the frictional coefficient of the particle,  $\eta$  is the viscosity and  $R_H$  is the hydrodynamic radius.

Dynamic light scattering data was measured using a Malvern HPPS system at the laboratory of Dr. Dermot Brougham, Dublin City University, Ireland. The Malvern HPPS has a 633 nm He-Ne laser which was preferable for  $\text{LiMo}_3\text{Se}_3$  samples given the material's absorbance peak around 479 nm. The detector was located at an angle of  $7^\circ$  (backscattering from the sample). It was found that  $10^{-3}\text{M}$  solutions were too opaque to give meaningful data, therefore, solutions of  $10^{-4}$  and  $10^{-5}$  M were used. The samples were analyzed as is (pristine), after centrifugation at 6000 g, after filtration using  $0.45 \mu\text{m}$  PTFE syringe filters and, finally, a combination of both centrifugation and filtration.

Results are shown as % in class vs. hydrodynamic diameter in figure 5.2. While pristine solutions have size distributions centred about 200-300 nm, centrifugation reduces this to the sub 100nm level. Filtration has the most dramatic effect reducing the size to  $\sim 10$  nm in both cases. The values quoted are the hydrodynamic diameter ( $R_H$ ) which, for a stiff solid rod, can be approximated as  $R_g = 1.732R_H$ , where  $R_g$  is the radius of gyration. [4]

$$R_g = \left( \frac{L^2}{12} + \frac{r^2}{2} \right)^{\frac{1}{2}} = 1.732R_H \quad (5.2)$$

Where  $L$  and  $r$  are the rod's length and radius

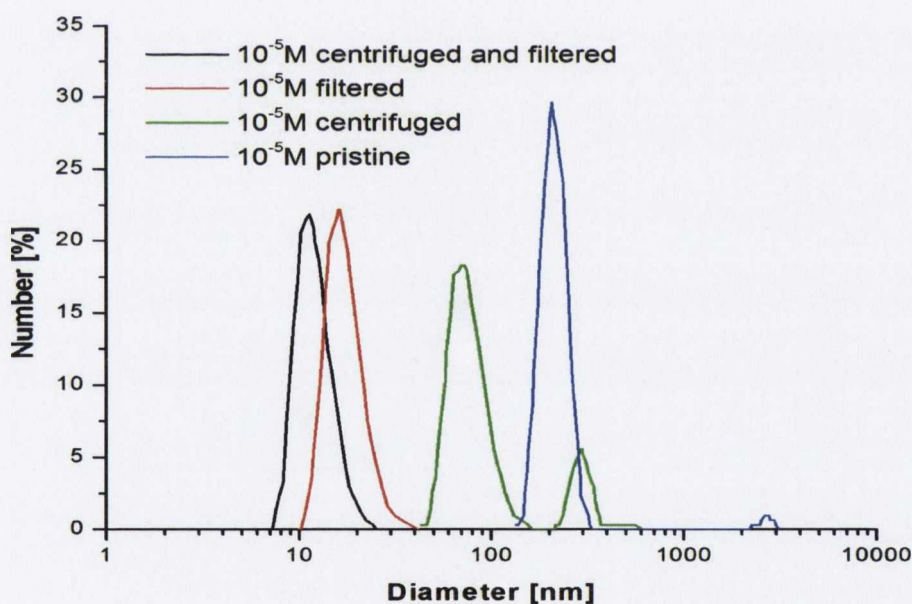
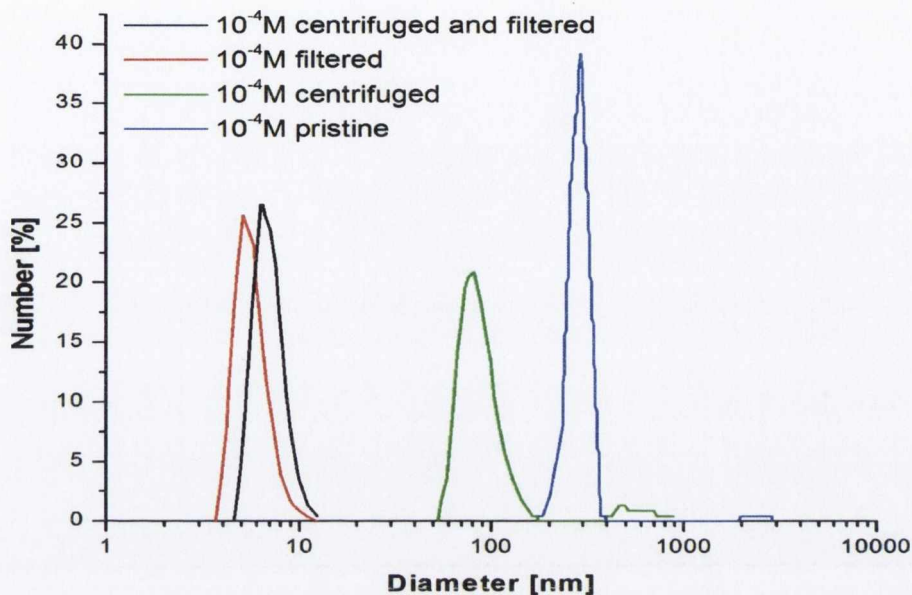


**Figure 5.2** Dynamic light scattering data for  $10^{-4}$  and  $10^{-5}$  M  $\text{LiMo}_3\text{Se}_3(\text{DMSO})$  solutions

From this the typical size of  $\text{LiMo}_3\text{Se}_3$  particles in solution can be estimated. From figure 5.2 a range of 5.4 nm to 16.3 nm is obtained for the hydrodynamic diameter for filtered and centrifuged samples of concentrations  $10^{-4}$  M and  $10^{-5}$  M. Taking

the largest value as an upper limit,  $R_H = 8.15$  nm will be used in the following calculation, an estimation of the size of a straight rod corresponding to the observed data.

Assuming a single (0.3nm radius)  $\text{LiMo}_3\text{Se}_3$  wire, the relationship in equation (5.2) above yields a length of 48.9 nm.

For a slightly larger particle of radius 1 nm, such as those seen lining up on the network scaffold in figure 4.14, a value of the length of 48.8 nm is obtained (the value of the radius term makes little difference in the case of high axial ratio cylinders).

The fragments seen lining up on the network in figure 4.14 have length dimensions of  $\sim 100$  nm and a radius of 1 nm. A fragment of these dimensions would give a value of  $R_H \sim 16.7$  nm which on the distribution in figure 5.2 would be seen as a peak centred about 33.4 nm. Given that the wire in solution is not likely to be perfectly straight this discrepancy may be acceptable.

Dynamic Light Scattering data has shown that filtration through a  $0.45 \mu\text{m}$  PTFE filter has a dramatic effect on the size distribution of the wires in solution. The image shown in Figure 5.3 was obtained from a filtered solution and shows that networks can still be obtained from filtered solutions. However, the large crystalline bundles are never observed in samples prepared this way.

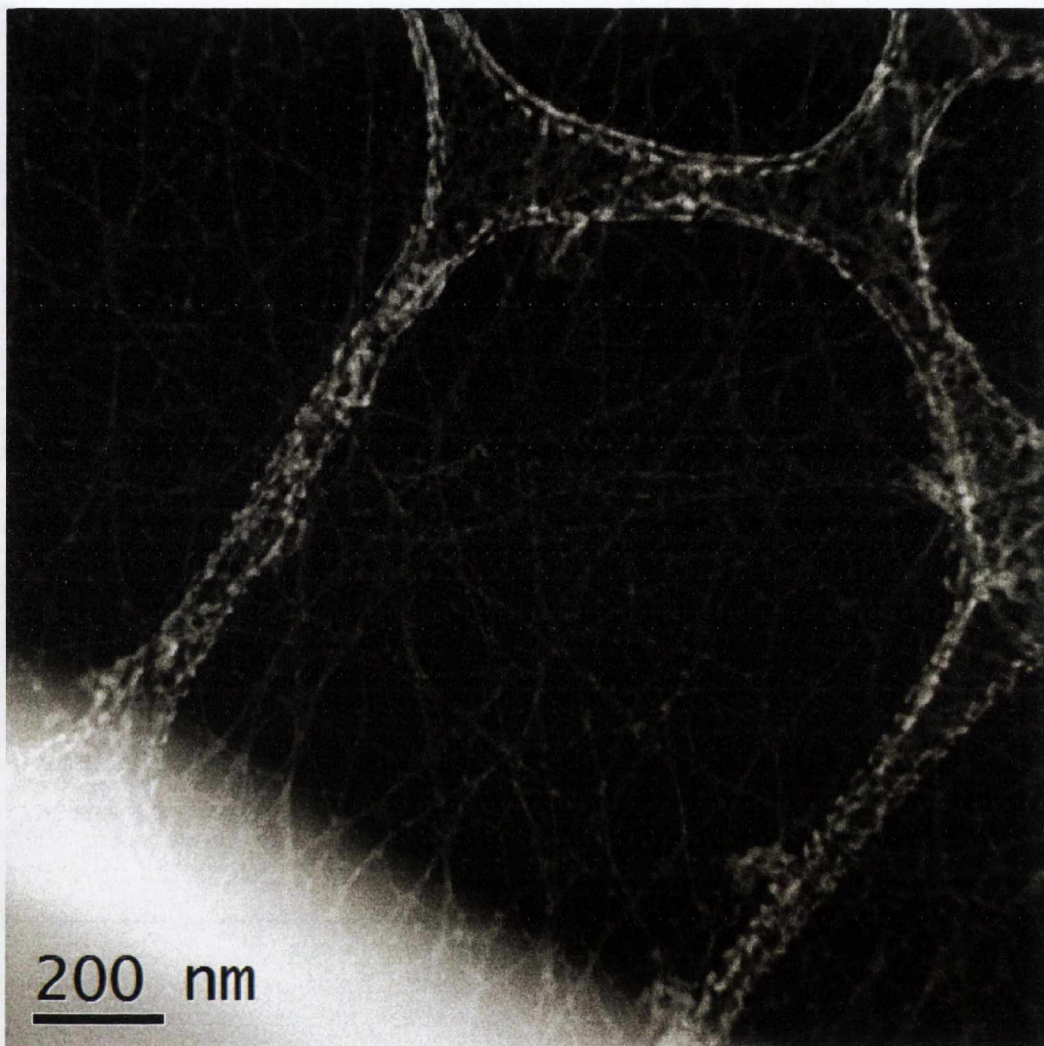


**Figure 5.3** STEM image of a network formed from a filtered  $10^{-4} M$   $\text{LiMo}_3\text{Se}_3(\text{DMSO})$  solution

It seems unlikely that, if networks were present in solution, they would pass through filters of this size, given that they have been observed to continuously span areas up to  $100 \mu\text{m}$  on a side. Figure 4.11 shows a  $3.5 \mu\text{m} \times 3.5 \mu\text{m}$  AFM image of a network on HOPG in which the constituent network wires have a height of  $\sim 4 \text{ nm}$ . A wire of  $L = 3.5 \mu\text{m}$  and  $r = 2 \text{ nm}$  would give a value of  $R_H \sim 2 \mu\text{m}$ . This value of  $R_H$  is greater than the values obtained from DLS measurements of pristine solutions (figure 5.2). Given that the DLS measurements rule out wires of this size (let alone the possibility of network spanning 10's of micrometers) in filtered solutions, and

that networks are still observed on substrates from filtered solutions it seems more likely that networks form from a scaffold laid down by smaller bundles which acts as a template upon which the small fragments observed in figure 4.14 ultimately align to create the observed network structure.

### 5.2.3 Dynamic Light Scattering comparison of filtered solutions kept in inert atmosphere and filtered solutions exposed to air

Dynamic light scattering was used to monitor the evolution of filtered solutions which were kept in inert atmosphere (argon glovebox) and filtered solutions which were exposed to air ( $\text{LiMo}_3\text{Se}_3$  is known to oxidise in the presence of oxygen or moisture[5, 6]). Over the course of 38 days a series of dynamic light scattering measurements were made on a variety of samples. The correlograms for a filtered  $10^{-5}\text{M}$   $\text{LiMo}_3\text{Se}_3(\text{DMSO})$  solution are shown in figure 5.4. In each instance a fresh aliquot was taken of the pristine solution (i.e. kept in an air and moisture free glovebox) for each measurement. As expected all the plotted normalised correlograms show good agreement indicating that the solution has not changed from the first measurement to the last. This is also evidenced by the fact that at any stage these solutions yield good quality networks.



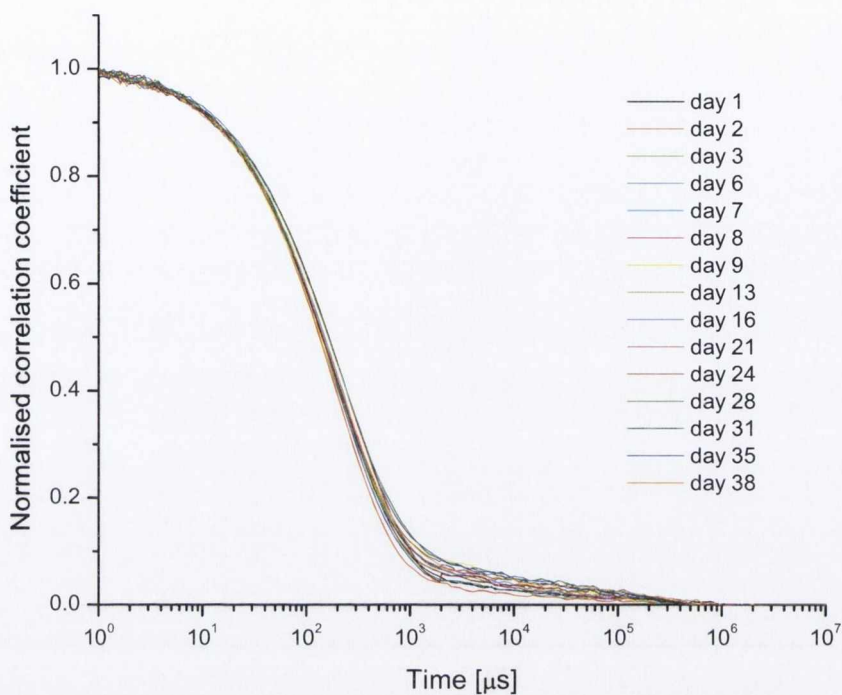


**Figure 5.4** Normalised correlograms from DLS measurements on a filtered  $10^{-5} M$   $\text{LiMo}_3\text{Se}_3(\text{DMSO})$  solution stored under glove box conditions. A fresh aliquot of this solution is removed from the glovebox for each measurement

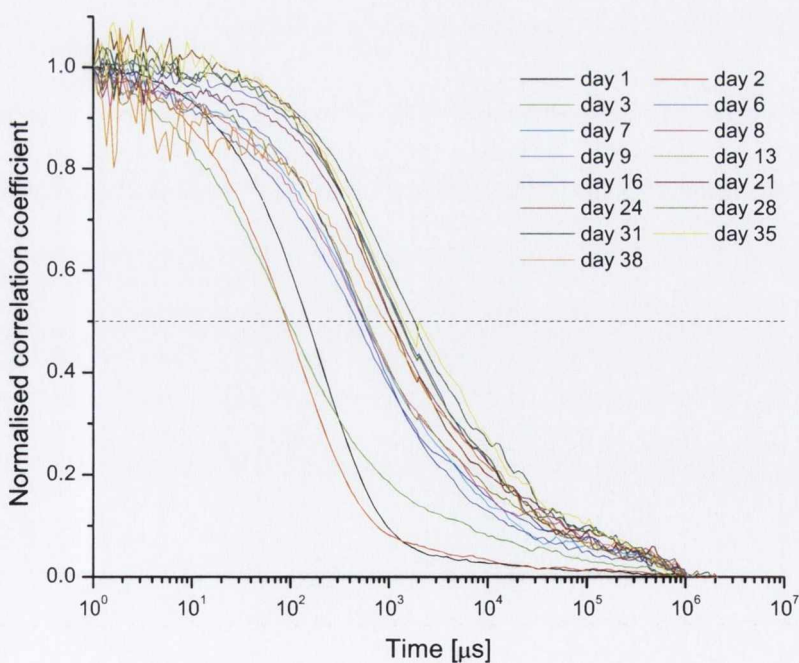


**Figure 5.5** Normalised correlograms of an air exposed, filtered  $10^{-5} M$   $\text{LiMo}_3\text{Se}_3(\text{DMSO})$  solution recorded over time. Cf. figure 5.4

Figure 5.5 shows the normalised correlograms for a filtered  $10^{-5}\text{M}$   $\text{LiMo}_3\text{Se}_3(\text{DMSO})$  solution which was placed in a cuvette on the first day and measured. The rubber septum of the cuvette was subsequently pierced and exposed to ambient for the remainder of the 38 day run. From the graph it is apparent that this sample does not remain constant over the time frame of the experiment. Instead the contents of the solution are changing. This is expected as it is known that  $\text{LiMo}_3\text{Se}_3$  oxidises upon exposure to ambient conditions. [5]

By taking the midpoint value on the y-axis of figure 5.5 (dotted line) and plotting this value against the age of the air exposed sample (1-38 days) figure 5.6 is obtained. The midpoint on the y-axis, is referred to  $t_{0.5}$  and is used as an indication of the average size of all species in solution, as the correlation function decay rate depends on the rate of Brownian motion in the sample and thus on the size. This graph shows the evolution of two  $10^{-4}\text{M}$  (squares) and two  $10^{-5}\text{M}$  (triangles) filtered  $\text{LiMo}_3\text{Se}_3(\text{DMSO})$  solutions. The black data points represent solutions which were filtered in the glovebox and had their septa pierced after the first measurement and remained pierced for the duration of the experiment. Red data points are of solutions which were filtered in air and then sealed. There is good agreement between the “pierced” and “air exposed once” samples, indicating that the time taken to filter the solutions in air is sufficient for an excess concentration of oxygen (relative to the concentration of  $\text{LiMo}_3\text{Se}_3$ ) to dissolve in the DMSO allowing the oxidation to proceed at the same rate as the samples who had their cuvette pierced on the first day.

The  $10^{-5}\text{M}$  solutions show rapid growth and it is difficult to obtain precise data after two weeks. The  $10^{-4}\text{M}$  solution grows steadily for the first three weeks and then appears to plateau.

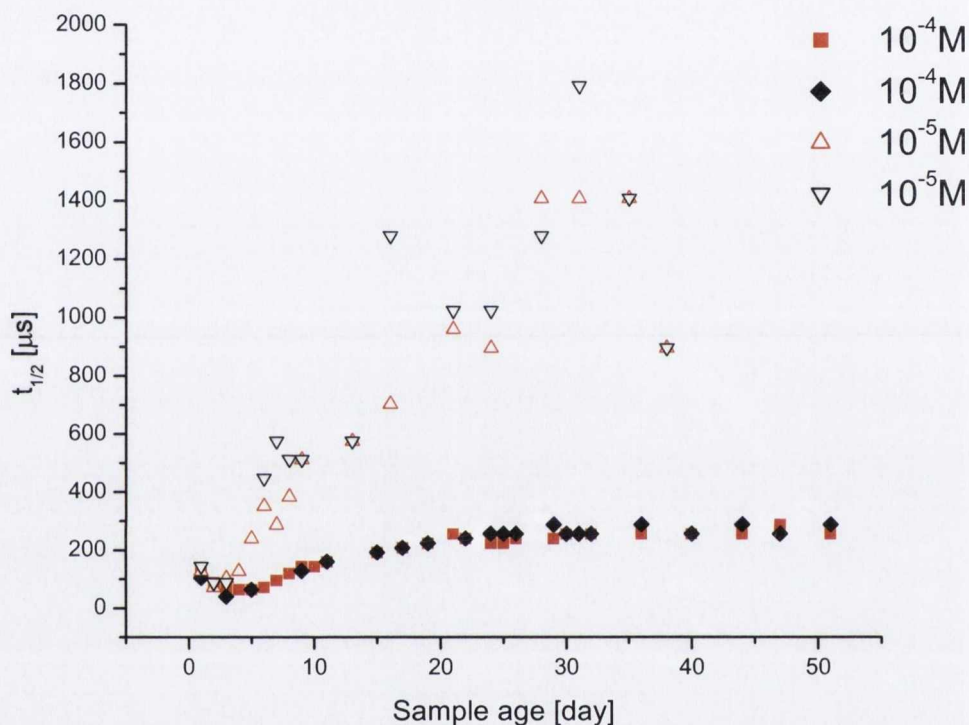


**Figure 5.6**  $t_{0.5}$  vs. time for air exposed  $10^{-5}\text{M}$  and  $10^{-4}\text{M}$  filtered  $\text{LiMo}_3\text{Se}_3(\text{DMSO})$  solutions. Squares indicate  $10^{-4}\text{M}$  solutions and triangles  $10^{-5}\text{M}$  solutions. Black indicates that the solutions were filtered in the glovebox and had their septum pierced at the time of the first measurement, red indicates that the solutions were filtered in air and then sealed.

Aliquots of the oxidising filtered solutions were also taken at intervals and drop cast on  $\text{SiO}_2$  substrates with vacuum pumping to remove the solvent. Figure 5.7 shows the SEM images obtained of these samples. After three days, networks are still observed for both concentrations (A and B), however some precipitate is visible in the  $10^{-4}\text{M}$  solution (A). After 9 days, the material from both concentrations is clearly

oxidised with some wires still visible (C and D) and after 36 days both samples show nothing but oxidised clumps on the substrate surface (E and F).

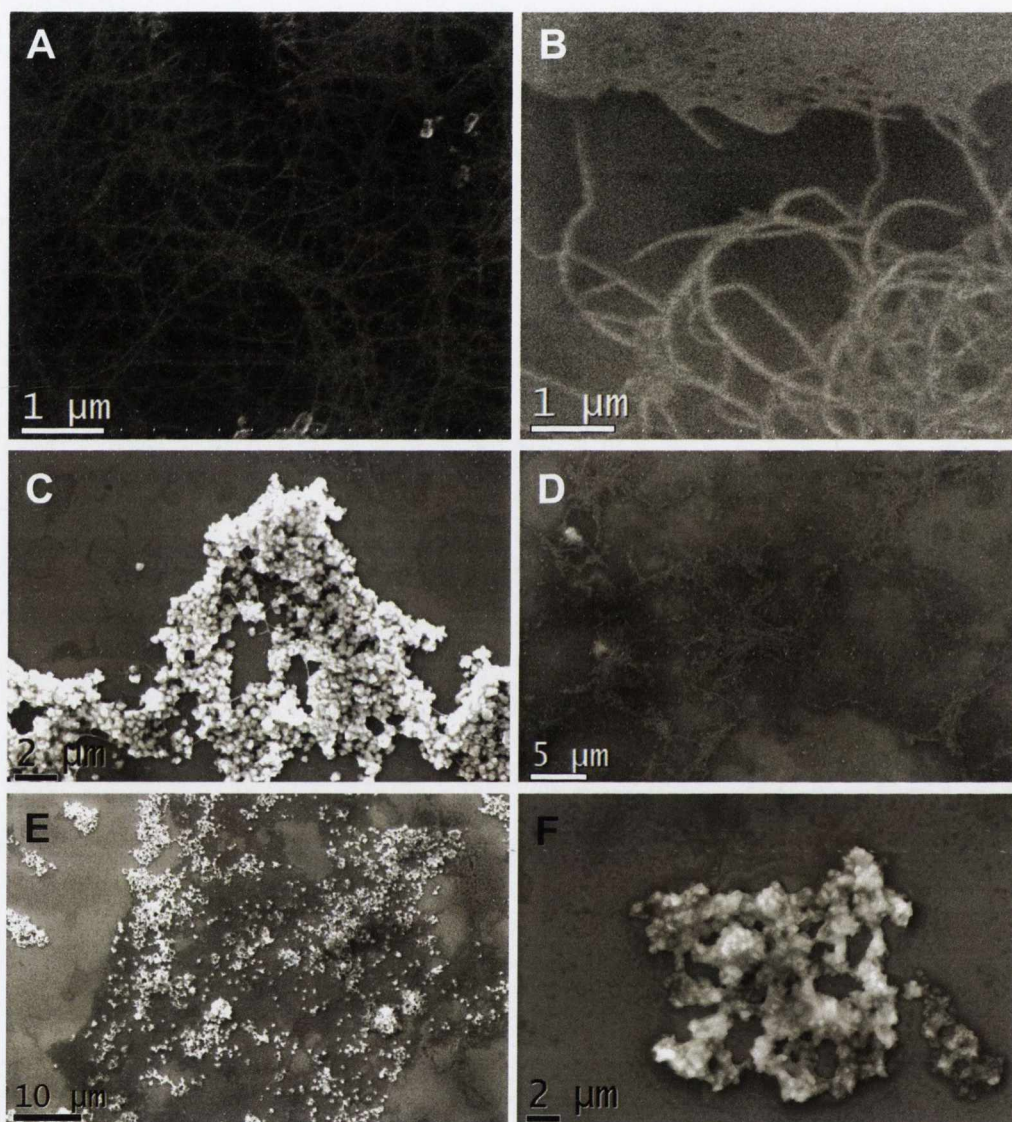


**Figure 5.7** SEM images of  $10^{-4} M$  (lhs) and  $10^{-5} M$  (rhs) air exposed  $LiMo_3Se_3(DMSO)$  solutions deposited on  $SiO_2$  at 3 days, 9 days and 36 days old.

In summary, filtered solutions which are kept in inert atmosphere remain constant throughout the 38 days that this experiment ran. Networks can be formed by spin or drop casting these solutions on substrate surfaces at any time. DLS measurements of

filtered solutions which are allowed to oxidise show that they do not remain constant during their lifetime. The value of  $t_{0.5}$  (an indication of the average size of all species in solution) increases with time. Precipitates were observed in the vials containing these samples. SEM images of samples formed by drop casting these oxidising solutions on  $\text{SiO}_2$  substrates show that nanowires and nanowire networks can still be observed for the first few days after air-exposure but that ultimately the wire species in solution degrade to form oxidised agglomerates.

#### 5.2.4 UV-vis spectroscopy of an air exposed $\text{LiMo}_3\text{Se}_3$ solution

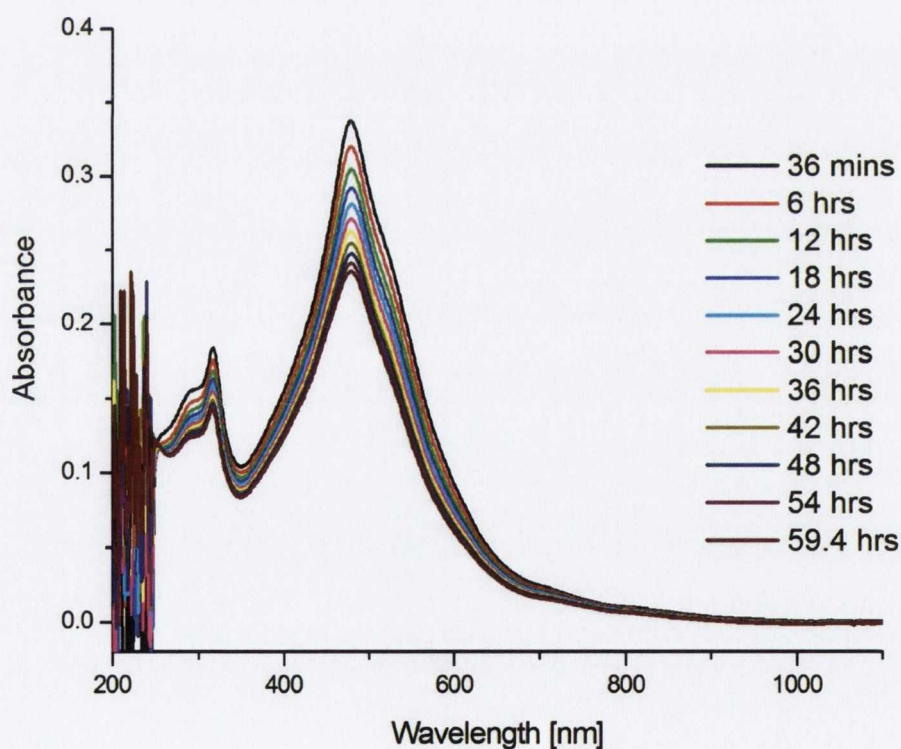


**Figure 5.8** UV-vis spectra of an air exposed  $10^{-4} \text{ M}$   $\text{LiMo}_3\text{Se}_3$  solution recorded over time

UV-vis (200 nm – 1100 nm) measurements were taken for a  $10^{-4}$ M  $\text{LiMo}_3\text{Se}_3$  solution in DMSO using a Shimadzu UV-1601. The required amount of solution was placed in a 1 mm path length cuvette outside of the glovebox and was immediately placed in the UV-vis apparatus. This air-exposed solution remained in the apparatus for 60 hours, with a spectrum recorded every 36 minutes. From the spectra shown in figure 5.8 it is apparent that while there is a loss in absorbance over this time frame, no new peaks are observed. From this data it was concluded that any product(s) formed from the oxidation of  $\text{LiMo}_3\text{Se}_3$  in solution do not have a UV-vis signature. This is most likely due to the fact that oxidised  $\{\text{Mo}_3\text{Se}_3\}$  materials are not soluble and form a precipitate.

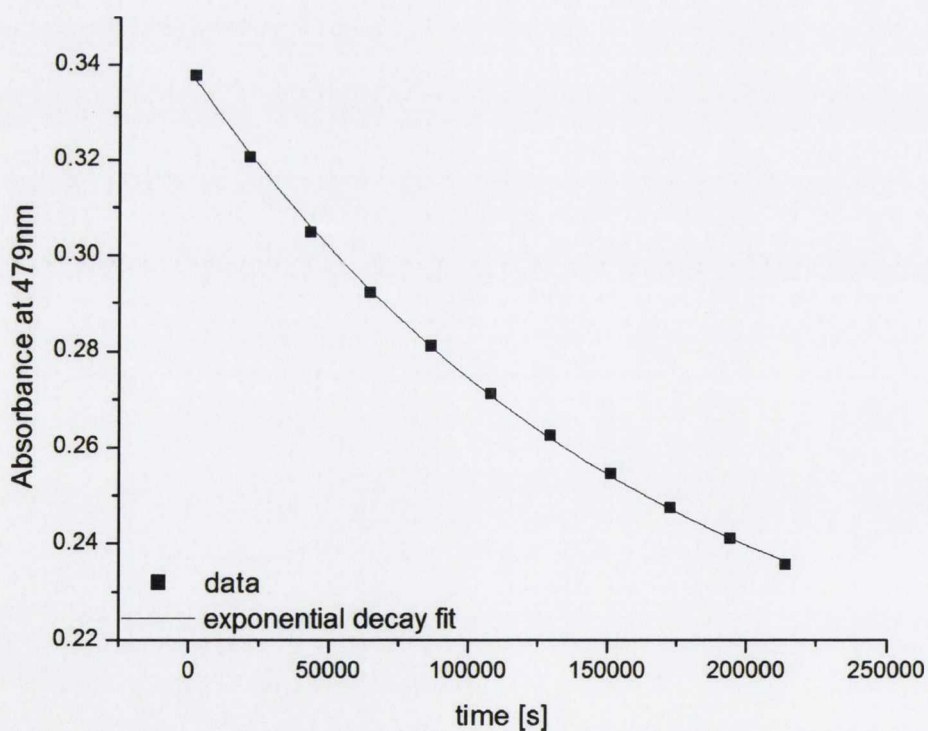


**Figure 5.9** Absorbance (at 479 nm) vs. time for a  $10^{-4}$ M  $\text{LiMo}_3\text{Se}_3(\text{DMSO})$  solution

By taking the value of the peak at 479 nm in figure 5.8 above for each successive run and then plotting the absorbance at 479nm vs. time the graph in figure 5.9, the rate of nanowire oxidation was determined. An exponential decay fit gives an equation of

$$A_{479nm} = 0.1991 + 0.1395e^{\left(\frac{-t}{162135 \cdot 3}\right)} \quad (5.3)$$

Where  $A_{479nm}$  is the absorbance at 479 nm and  $t$  is the time

This is indicative of a pseudo first order reaction of the nanowire species oxidising in solution which has been exposed to ambient. Air is readily soluble in DMSO. Based on the work of Dymond [7, 8]  $O_2$  has solubility in DMSO of  $1.57 \times 10^{-4}$  (expressed as a mole fraction). This yields a concentration of  $O_2$  in DMSO of  $2.21 \times 10^{-3}$  M, two orders of magnitude higher than the concentration of  $LiMo_3Se_3(DMSO)$  which is  $1.881 \times 10^{-4}$  M. Thus the concentration of  $O_2$  in solution can be considered constant as the nanowire material oxidises.

Using the Beer-Lambert equation:

$$A = \epsilon lc \quad (5.4)$$

Where  $A$  at time zero can be established from equation (5.3),  $l$  is the cuvette length (0.1cm) and  $c$  is  $LiMo_3Se_3(DMSO)$  concentration,  $1.881 \times 10^{-4}$  M. This yields a value for the molar absorptivity,  $\epsilon$ , of  $18002 \text{ L}\cdot\text{mol}^{-1}\cdot\text{cm}^{-1}$ .

The half-life,  $t_{1/2}$  (not to be confused with  $t_{0.5}$ , section 5.2.3) is calculated to be  $1.1238 \cdot 10^5$  seconds, indicating that (approximately) every 31.2 hours the absorbance (and therefore the concentration) will halve.

## 5.3 Discussion and Conclusions

### 5.3.1 Discussion of droplet effect

$\text{LiMo}_3\text{Se}_3$  materials are typically found within solution “stains” following surface deposition in locations where droplets can become pinned to the surface, often due to surface heterogeneities.[9] While the droplet has a uniform distribution of material, the stains observed on the surface have a non-uniform distribution; there is typically much more material at the edge of a stain. As the solution evaporates at the edges (which are pinned in place), there is a flow of solution from the centre of the droplet to replace the solution which has evaporated. [9, 10] As droplets of  $\text{LiMo}_3\text{Se}_3$  solutions evaporate, the bulk of the dissolved materials recrystallize toward the edge of these droplets. Typically, networks are observed throughout these areas, while the vast majority of bundles are located at the edges of these “stains”. For substrates which were pumped immediately following solution deposition (without allowing the solution to stand on the surface for  $\sim 2$  minutes prior to pumping), morphologies of “incomplete” network were observed. These samples showed what appear to be small wire fragments lining up onto network scaffolds (see section. 4.3.2, figure 4.14). These observations are supported by both rheometry measurements (section 5.2.1) that show behaviour consistent with one-dimensional species in solution and Dynamic Light Scattering data (section 5.2.2.) that shows filtered and centrifuged solutions have a dominant sub 10 nm species in solution. Filtered solutions cast on substrate surfaces also revealed the presence of  $\text{LiMo}_3\text{Se}_3$  networks and the absence of larger bundles (figure 5.3).



### 5.3.2 Conclusions

The presence of bundles and networks of  $\text{LiMo}_3\text{Se}_3$  on substrate surfaces after solution deposition and solvent removal was discussed previously in Chapter 4. Large bundles ( $> 20$  nm laterally) have non-cylindrical geometries and are believed to be present in solution as crystallites. It still remains unclear precisely how these networks form. However, from the results summarised above it seems unlikely that these networks are free-standing in solution. The data suggest that these networks form upon solvent evaporation, consistent with other reported nanoscale networks, such as Au nanoparticles. [11] However, an important distinction between those networks and the ones observed here must be drawn, in that those networks consist of an agglomeration of discrete nanoscale objects, neighbouring particles are simply particles which are arranged side by side. These observations differ from those reported herein for networks of  $\text{LiMo}_3\text{Se}_3$ , which are shown to consist of wires which are continuous through junctions between network branches. In figure 4.12 it is clear that the constituent wires of these junctions can splay and divide into branches making up the neighbouring network components.

From these results, it seems likely that networks form from individual  $\{\text{Mo}_3\text{Se}_3\}_\infty$  strands which recrystallise into bundles on substrate surfaces. At some points along these bundles junctions form, most likely due to an external factor such as the presence of another recrystallising bundle, the presence of a wire fragment or other particle on the surface.

Light scattering and UV-vis studies of oxidising solutions show that the  $\text{LiMo}_3\text{Se}_3$  agglomerate and ultimately crash out of solution with no change to the UV-vis

signature but with and observed loss in absorbance. These data suggest that networks are formed during deposition and that the degree of network formation is dependent on the stability of the material. As seen in the SEM images of oxidising  $\text{LiMo}_3\text{Se}_3$  solutions (figure 5.7), older solutions (oxidising > 3 days) show little evidence of networked materials and consist of oxidised agglomerates. However, filtered solutions which are kept in an inert atmosphere remain pristine over time and always are able to form networks on substrate surfaces.

## References

- [1] Malvern\_Instruments, *Technical Note*, [www.malvern.com](http://www.malvern.com), *Introduction to Dynamic Light Scattering*.
- [2] N. C. Santos, M. A. Castanho, *Biophysical journal* **1996**, *71*, 1641.
- [3] B. R. Jennings, K. Parslow, *Proceedings of the Royal Society of London. A. Mathematical and Physical Sciences* **1988**, *419*, 137.
- [4] Malvern\_Instruments, *Application Note*, [www.malvern.com](http://www.malvern.com), *What is the difference between  $R_g$  and  $R_H$* .
- [5] J. M. Tarascon, F. J. DiSalvo, C. H. Chen, P. J. Carroll, M. Walsh, L. Rupp, *Journal of Solid State Chemistry* **1985**, *58*, 290.
- [6] J. M. Tarascon, G. W. Hull, F. J. DiSalvo, *Materials Research Bulletin* **1984**, *19*, 915.
- [7] R. Battino ed., *Solubility Data Series, Vol 7. Oxygen and Ozone*, Pergamon Press **1981**, 7.
- [8] J. H. Dymond, *J. Phys. Chem.* **1967**, *71*, 1829.
- [9] R. D. Deegan, O. Bakajin, T. F. Dupont, G. Huber, S. R. Nagel, T. A. Witten, *Nature* **1997**, *389*, 827.

[10] R. D. Deegan, *Physical Review E* **2000**, *61*, 475.

[11] P. Moriarty, M. D. R. Taylor, M. Brust, *Physical Review Letters* **2002**, *89*, 248303.

## Chapter 6

### Electron Microscopy of frozen and freeze-dried

### LiMo<sub>3</sub>Se<sub>3</sub> nanowire solutions

#### 6.1 Introduction

The presence of bundles and networks of LiMo<sub>3</sub>Se<sub>3</sub> on substrate surfaces after solution deposition and solvent removal was discussed previously in chapter 4. AFM, rheometry, DLS, and S/TEM data have been discussed and collectively indicate that solutions do not consist of large networked materials (chapter 5). However, these data are not conclusive. To further examine the composition of the solution, frozen solutions of LiMo<sub>3</sub>Se<sub>3</sub> in DMSO and LiMo<sub>3</sub>Se<sub>3</sub> in H<sub>2</sub>O (as well as freeze-dried samples of these solutions) were examined using a combination of Transmission Electron Microscopy (TEM), Scanning Transmission Electron Microscopy (STEM) and Energy Dispersive X-ray (EDX) analysis. The results from these studies are discussed herein.

#### 6.2 Experimental

The preparation of samples for cryo TEM analysis is described briefly as follows. A TEM grid (400 mesh Cu, lacy C film) is clamped in tweezers and placed in a GATAN Cryoplunge “guillotine” system[1] as illustrated in figure 6.1. Using a pipette, a small (< 1 ml) drop is placed on the grid which is then blotted using a small roll of filter paper for 0.6 seconds to remove the excess solution while still leaving a film of nanowire solution on the face of the TEM grid. After blotting the

grid is immediately plunged into a reservoir of liquid ethane (-182.8°C m.p.) instantly freezing the solution (DMSO m.p. 17.9°C). The rapid freezing of the film of nanowire solution does not permit the rearrangement of whatever  $\{\text{Mo}_3\text{Se}_3\}$  strands that might exist in the solution, so that images obtained of these samples should reflect the composition of a cross section of pristine solution.[2] The sample grids were transferred to a liquid nitrogen cooled sample stage and introduced to the TEM system. A commercial S/TEM instrument (Tecnai F20 supertwin) operating at 200 kV was used for analysis<sup>3</sup>.

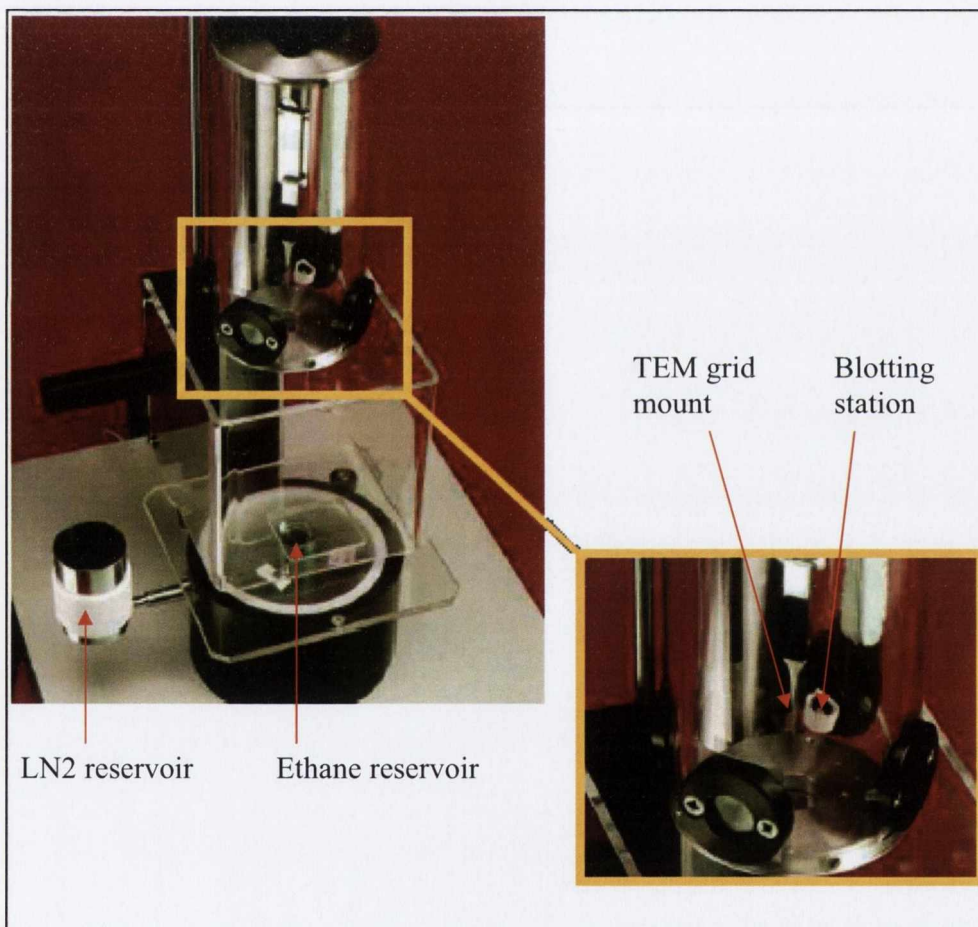


**Figure 6.1:** Gatan Cryoplunge system[1]

<sup>3</sup> This work was carried out at Johnson Matthey, Sonning Common, UK with Dr. Dogan Ozkaya. Three sessions were carried out with the Ph.D. candidate present for the first two to prepare the samples and direct the imaging. The final session was the imaging of the freeze-dried sample of a filtered  $\text{LiMo}_3\text{Se}_3(\text{DMSO})$  solution carried out under the direction of Dr. Ozkaya.

Freeze-drying was attempted by keeping the sample in the TEM chamber overnight and allowing the liquid nitrogen in the cooling stage to boil off. The triple point of DMSO occurs at 291.6 K, 0.489 mbar.[3-5] As the pressure in the TEM chamber is kept at  $\sim 3 \times 10^{-7}$  mbar throughout, as the temperature of the stage rises to room temperature, the DMSO solvent will sublime and the  $\text{LiMo}_3\text{Se}_3$  solute will ultimately crash out onto the lacy carbon film of the TEM grid.[6]

## 6.3 Characterisation

### 6.3.1 Cryo-TEM of unfiltered $\text{LiMo}_3\text{Se}_3(\text{DMSO})$ solutions

The first solution analysed using this technique was a  $10^{-3}\text{M}$   $\text{LiMo}_3\text{Se}_3(\text{DMSO})$  solution. The solution was prepared as normal in an inert argon atmosphere and then sealed in an airtight container for shipping.

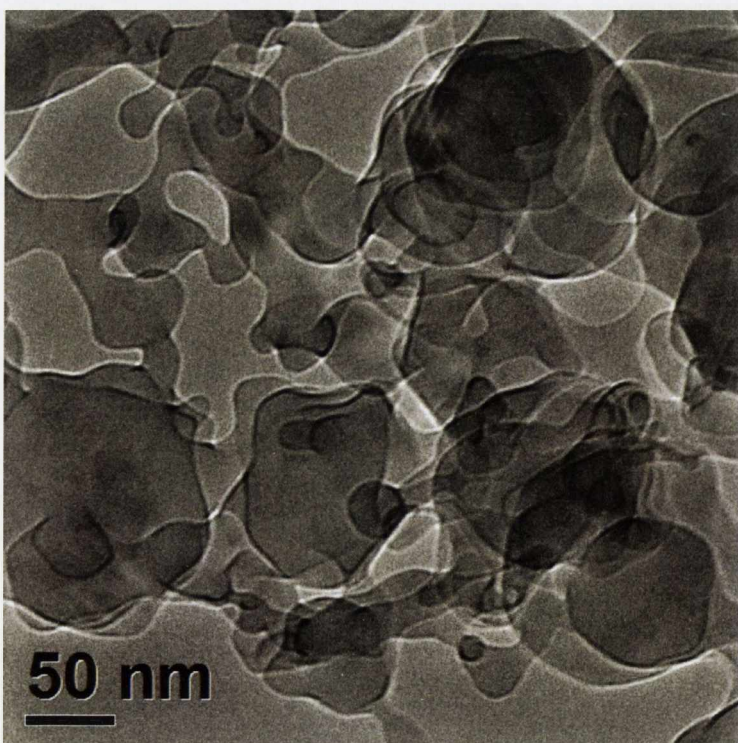
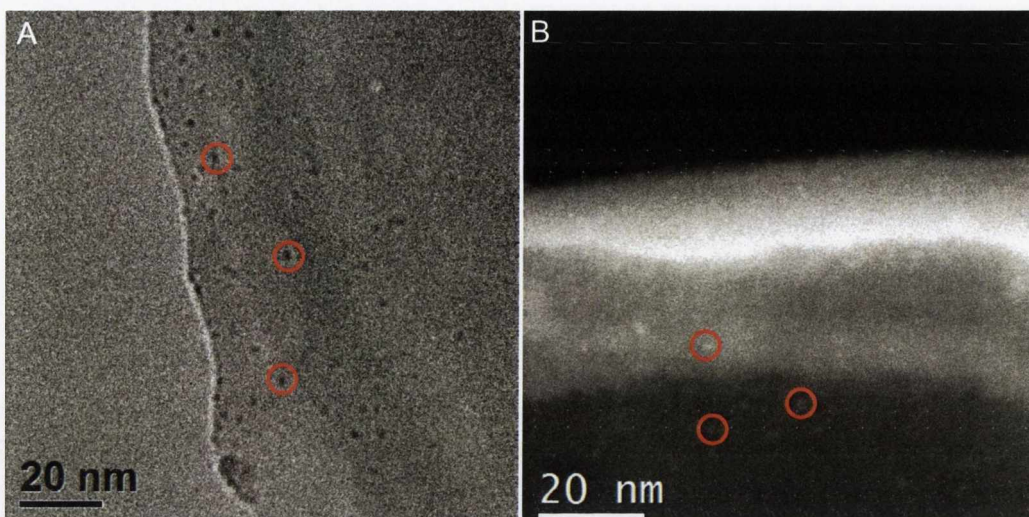


**Figure 6.2:** Frozen unfiltered  $\text{LiMo}_3\text{Se}_3(\text{DMSO})$  nanowire solution suspended on a TEM grid carbon film

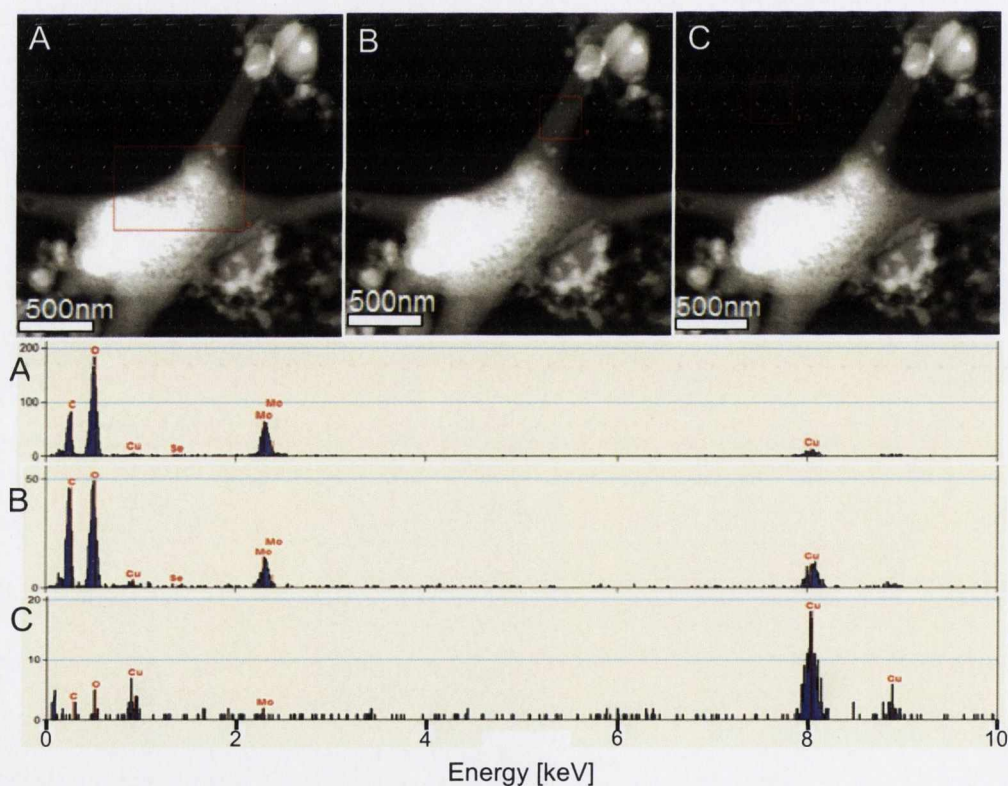
A small (< 1 ml) droplet was placed on a TEM grid, blotted and then plunged into liquid ethane. The grid was transferred to the TEM stage under liquid nitrogen and introduced to the vacuum of the TEM with the minimum air exposure.

Figure 6.2 shows a TEM image of a frozen nanowire solution film over a lacy carbon film on a copper TEM grid. At low magnifications such as this and in TEM mode it is difficult to identify any wire material in the matrix. However this image demonstrates that the sample preparation conditions used will produce electron transparent areas of frozen nanowire solution films. It also shows the morphology of a frozen nanowire solution film.

Figure 6.3A is a TEM image of an area of the solution film containing  $\text{LiMo}_3\text{Se}_3$  nanowire particles or fragments. The particles in this image are approximately 2 nm in size and appear darker than the surrounding medium, as is to be expected in normal TEM mode. Changing to STEM mode and using the high angle annular dark field (HAADF) detector the Z-contrast between the heavier  $\text{LiMo}_3\text{Se}_3$  materials and the lighter DMSO matrix and carbon support film can be observed. Figure 6.3B is an image of a similar area to figure 6.3A taken in STEM mode. The particles appear now as bright spots and show a real Z-contrast to the surrounding medium, indicating that these are  $\text{LiMo}_3\text{Se}_3$  particles.



**Figure 6.3.** *A: TEM image of  $\text{LiMo}_3\text{Se}_3$  particles suspended in the frozen DMSO solution (unfiltered) medium. B: A similar area imaged in HAADF STEM mode. In each image three of the many particles present are ringed in red*



**Figure 6.4.** *STEM image of a dense area of frozen  $\text{LiMo}_3\text{Se}_3(\text{DMSO})$  solution (unfiltered) on carbon support film and associated EDX spectra of three distinct regions corresponding to the red box in each image: A, the bulk of the material, B, a less dense area adjacent to A and C, which records the background of the vacuum.*



Figure 6.4 is a STEM image of a dense area of  $\text{LiMo}_3\text{Se}_3$  material suspended in solution on an area of the carbon support film. EDX spectroscopy was performed on three separate areas as shown.

As expected the Mo peak at 2.293 keV ( $\text{La}_1$ ) is visible in spectra A and B indicating that these areas are rich in  $\text{LiMo}_3\text{Se}_3$  nanowires and particles. The Mo peak has a greater intensity in spectrum A which correlates to the higher contrast in that region of the image. There are significant C and O peaks in both spectra, most likely originating from the solvent (DMSO). It is also possible that there is a contribution from oxidised  $\text{LiMo}_3\text{Se}_3$  material, given that the sample preparation was carried out in ambient conditions using a solution which had been prepared in an inert Argon atmosphere. Spectrum C (background) shows no Mo present (as expected) but the Cu peaks present in spectra A and B are still present here. These peaks are attributed to the TEM grid and the geometry of the sample with respect to the EDX detector.

### 6.3.1a Freeze-drying of unfiltered $\text{LiMo}_3\text{Se}_3(\text{DMSO})$ samples

After imaging was completed, any excess liquid nitrogen was decanted from the sample holder and the sample was allowed to warm to room temperature overnight in the UHV conditions of the TEM chamber. As a result, any material left on the grid the next day should be representative of the original solution contents, because as the solution warmed in the high vacuum of the TEM chamber, the solvent was sublimed away (freeze-dried) depositing solid  $\text{LiMo}_3\text{Se}_3$  materials to the lacy carbon support film. [2, 6-8]

TEM and STEM images of a freeze-dried sample are shown in figure 6.5 along with EDX spectra obtained for the two areas enclosed by the red boxes in the STEM image.

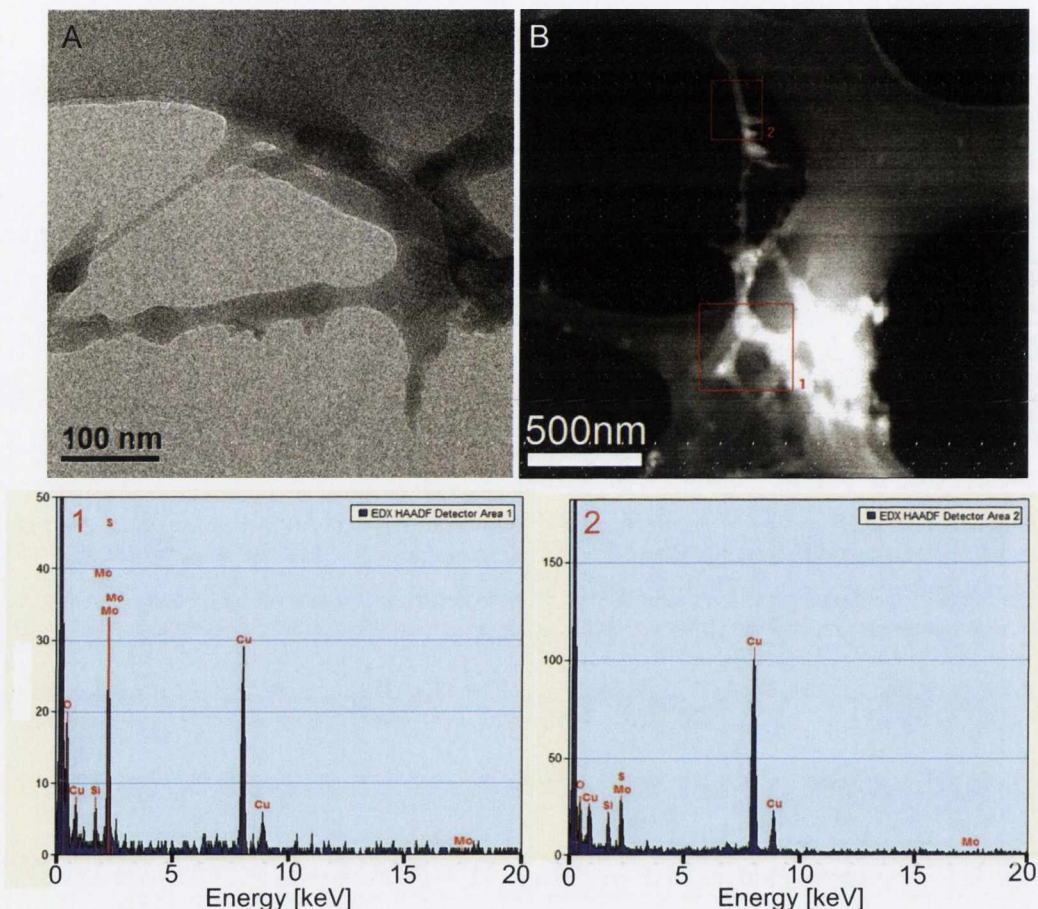


**Figure 6.5.** A: TEM image of freeze-dried unfiltered  $\text{LiMo}_3\text{Se}_3(\text{DMSO})$  sample on lacy carbon film TEM grid, B: STEM image of freeze-dried sample, spectra 1 and 2 correspond to the numbered red boxes in B.

Figure 6.5A shows a TEM image obtained of  $\text{LiMo}_3\text{Se}_3$  material deposited on the sample grid which is suspended over vacuum and supported by the edges of a region of lacy carbon film. Figure 6.5B shows a lower magnification image of the same area (rotated through  $90^\circ$ ), the bright contrast in this HAADF image indicating that these strands are  $\text{LiMo}_3\text{Se}_3$ . The wires in these images do not appear as clear or with the same resolution as previous samples imaged in S/TEM. The system used is more than capable of the high resolution images seen previously (chapter 4), however it

seems that the manner of sample preparation and the likely oxidation of the solutions contribute to make these samples somewhat amorphous and difficult to image. The spectra labelled 1 and 2 in figure 6.5 correspond to the similarly numbered boxes on the STEM image. The presence of Mo is noted in both spectra.

### 6.3.2 Cryo-TEM of unfiltered aqueous $\text{LiMo}_3\text{Se}_3$ solutions

Based on the difficulty of imaging frozen and freeze-dried samples of  $\text{LiMo}_3\text{Se}_3$  dissolved in DMSO, another sample was prepared where water was used as the solvent. In this case, water was chosen because it is known that cryo-fixation of water solutions give vitreous ice [7, 8] which is considerably easier for obtaining high resolution images. These solutions were prepared in an inert argon atmosphere using deionised water which had been bubbled through with argon for 15 minutes to remove dissolved oxygen prior to being sealed and transported for analysis.

It was noted that with repeated imaging the electron beam caused the solution film to sputter away, causing the encased material to migrate within the remaining film and agglomerate. Figure 6.6 contains three STEM images of a film of  $\text{LiMo}_3\text{Se}_3(\text{aq})$ . Figure 6.6A is the initial image of this area. The bright particles in the bottom right hand corner are dense areas of nanowire material. The latticework that is visible throughout most of the rest of the image consists of small  $\text{LiMo}_3\text{Se}_3$  fragments similar to those seen in figure 6.3. The image displayed in figure 6.6B was taken after approximately two minutes of raster scanning by the beam.

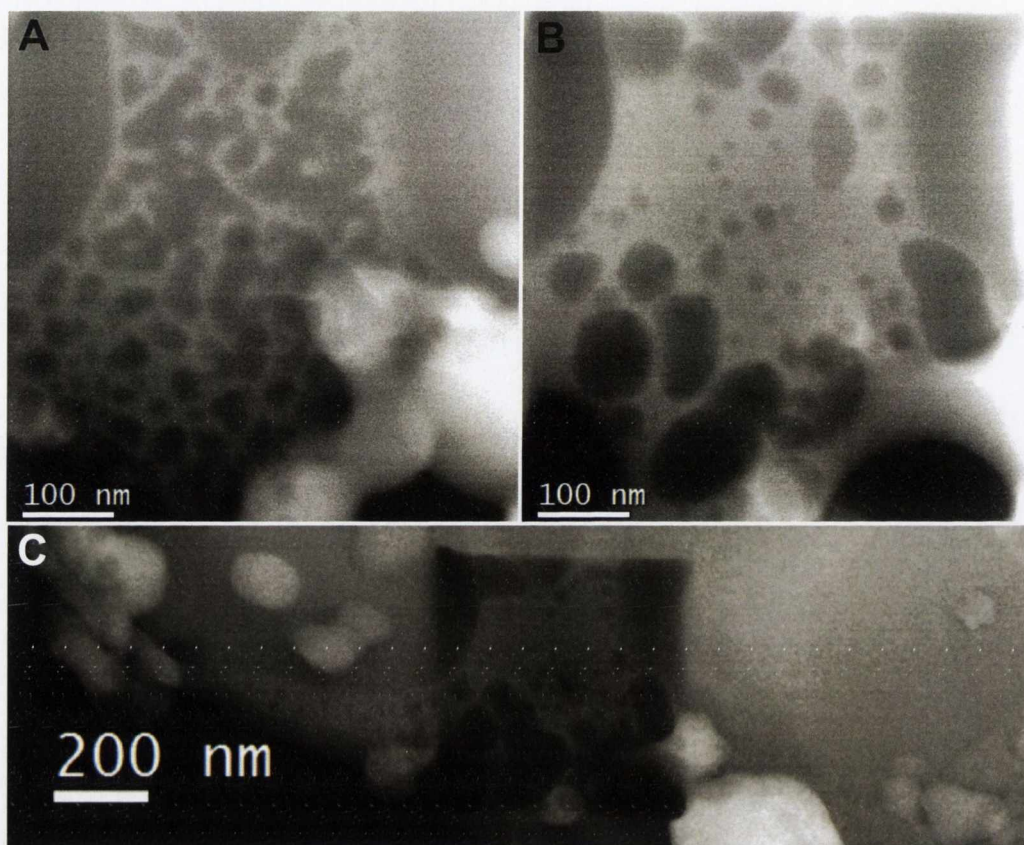


**Figure 6.6.** STEM images of frozen unfiltered aqueous  $\text{LiMo}_3\text{Se}_3$  solution on lacy carbon TEM grid. A: initial image, B: after two minutes of imaging, C: lower magnification view of damaged area

The structure of the  $\text{LiMo}_3\text{Se}_{3(\text{aq})}$  film has been altered under exposure to the electron beam. Following exposure it appears as a continuous mass of nanowire particles. As the solvent ( $\text{H}_2\text{O}$ ) was being sputtered by the electron beam, the wire fragments started to agglomerate on the new surface of the frozen solution film. Figure 6.6C is a lower magnification view of the area, showing the local damage caused by the beam.

While agglomerations of particles and fragments were common within the frozen medium, they were not the only structures observed. Figure 6.7 is a STEM image which shows a large amount of nanowire (bright) material. In the bottom right hand

corner there is some material similar to that of figure 6.6, however, what is of interest is the large high Z-contrast entanglement of material in the centre and top of the image. This material remained stable over several minutes of scanning (although because the magnifications are different the beam dose was accordingly lower). Some of the features in this image are highly reminiscent of pristine  $\text{LiMo}_3\text{Se}_3$  nanowires, for example, the feature bounded by the blue box on figure 6.7.

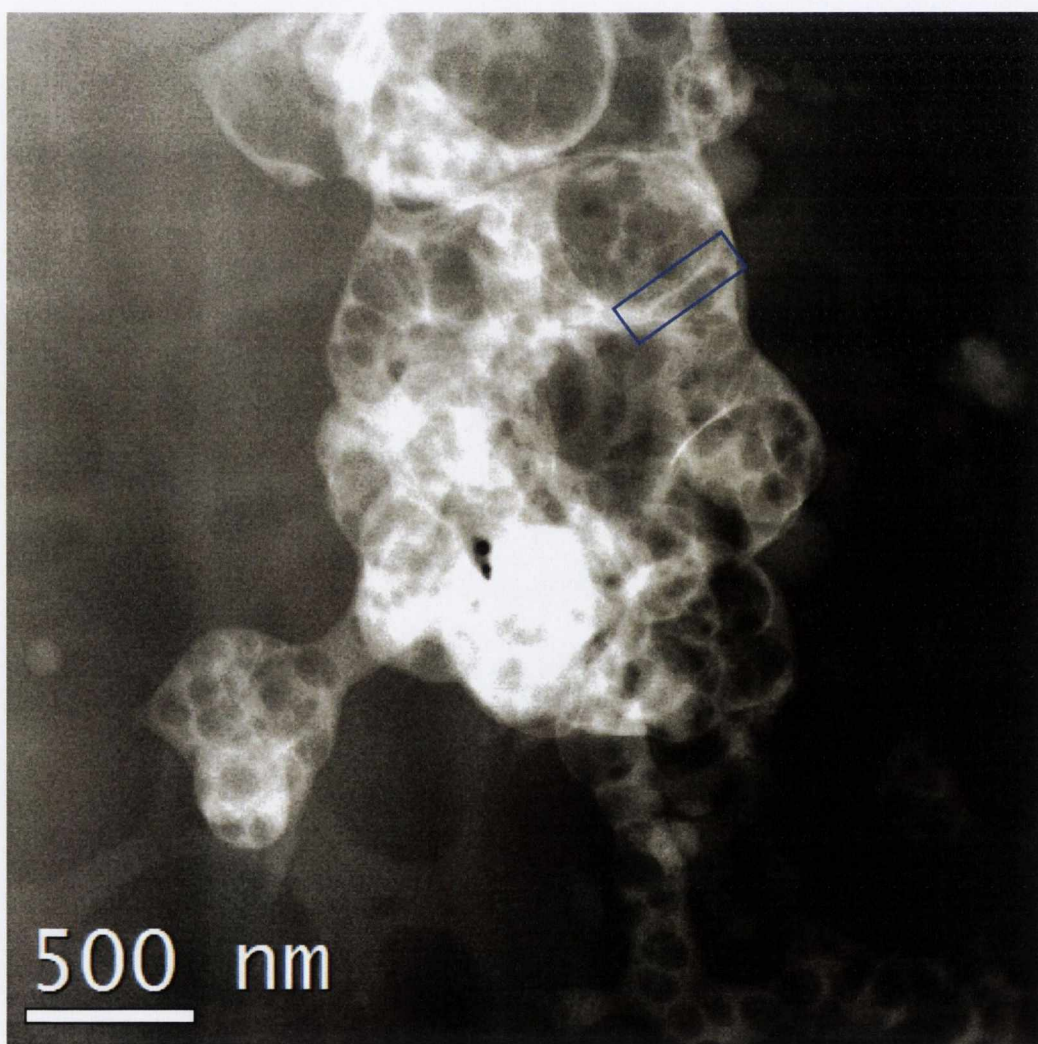


**Figure 6.7** STEM image of frozen unfiltered aqueous  $\text{LiMo}_3\text{Se}_3$  on lacy carbon TEM grid

Whole, distinct nanowire bundles were also observed in this sample. STEM images of a thin area of  $\text{LiMo}_3\text{Se}_{3(\text{aq})}$  film in figure 6.8A show long, narrow nanowire bundles embedded in the frozen solution. Another area with bundles is shown in figures 6.8B and C. In this instance, repeated imaging caused the bundles to fragment (figure 6.8C). This was unusual given the previously observed stability of nanowire bundles spun or drop cast (without freezing) onto a TEM grid and imaged in conventional TEM and STEM modes (chapter 4). Those images showed pristine bundles, at much higher magnifications and beam doses. Furthermore, they were imaged repeatedly with no sign of degradation under the electron beam. Given that the nanowires imaged in figure 6.8 were prepared by dissolution in water, it seems likely that the observed instability is due to the fact that these wires are heavily oxidised.

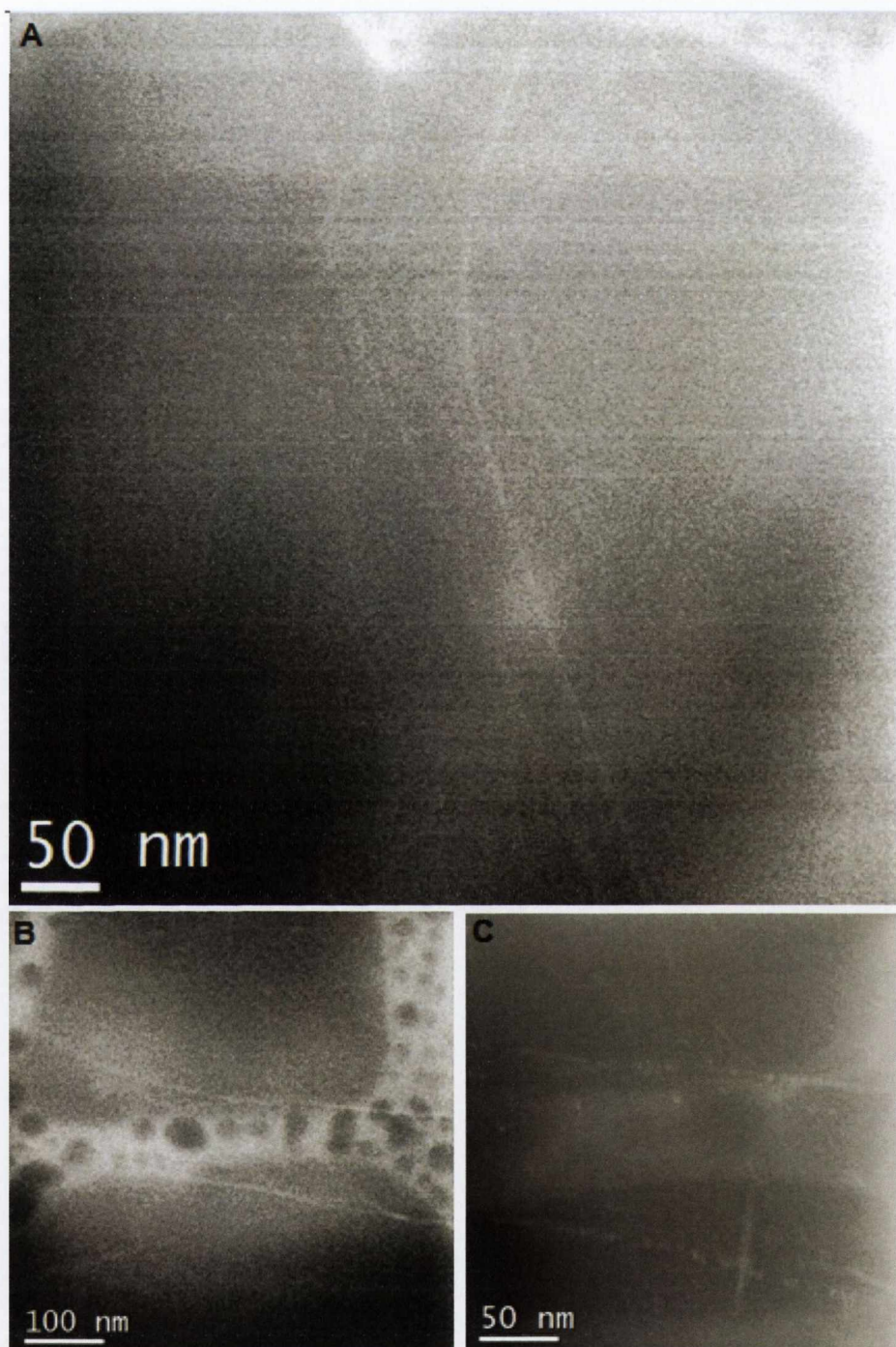


**Figure 6.8.** *A: STEM image of wires visible in frozen unfiltered aqueous  $\text{LiMo}_3\text{Se}_3$  suspended on lacy carbon TEM grid. B: wires running across image. C: same area as B, electron beam has caused nanowire to fragment.*

Some areas of the sample showed features which bare a great resemblance to the SEM images of air-exposed  $\text{LiMo}_3\text{Se}_3(\text{DMSO})$  solutions (section 5.2.3). Figure 6.9C is one of those SEM images, included here for comparison. Figure 6.9 A and B are a

STEM image of one of these features and the EDX spectra obtained from the area marked in red on the image. EDX in this area shows very large carbon and oxygen peaks with only a small amount of Mo and Se. The resemblance to the particles in figure 6.9C is striking but unsurprising given that they are both obtained from oxidised solutions.

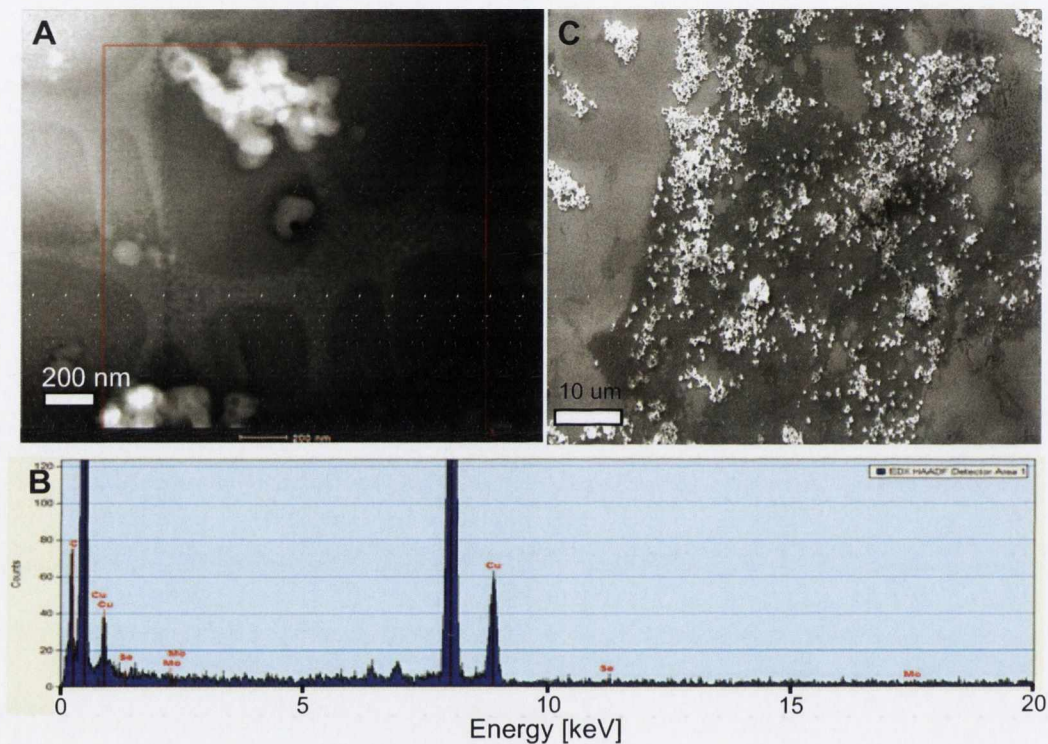


**Figure 6.9.** A: STEM image of frozen unfiltered aqueous  $\text{LiMo}_3\text{Se}_3$  solution (on lacy carbon TEM grid) showing heavily oxidised material. B: EDX spectrum of red box area in A. C: SEM image of an oxidised  $\text{LiMo}_3\text{Se}_3(\text{DMSO})$  solution (drop cast on a  $\text{SiO}_2$  substrate, never frozen)



### 6.3.2.a Freeze-drying of unfiltered $\text{LiMo}_3\text{Se}_3(\text{aq})$ samples

The sample prepared from a  $\text{LiMo}_3\text{Se}_3(\text{aq})$  solution was freeze-dried by allowing it to remain under vacuum in the TEM chamber overnight as the sample stage warmed up to room temperature. The sample was imaged the next day.

Conventional TEM imaging of the freeze-dried aqueous sample shows what appears to be a large scale network spanning for microns, figure 6.10A. Other than the areas of oxidised particles this is very similar to images of large scale pristine network formed on surfaces (chapter 4). A more magnified image, figure 6.10B, shows a junction of this network, which appears to be two entangled bundles rather than a continuous network where both branches are coordinated by a shared crystalline bundle.

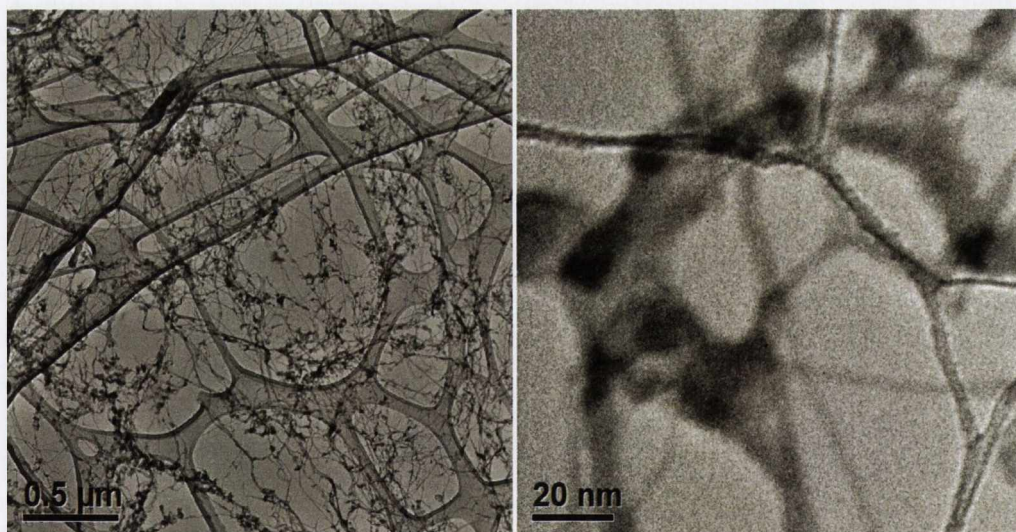


**Figure 6.10.** TEM images of freeze-dried unfiltered aqueous  $\text{LiMo}_3\text{Se}_3$  solutions on lacy carbon TEM grid

STEM imaging of this area supports what was observed in TEM mode. With Z-contrast it can easily be seen that this network is composed of a heavier material than the background carbon support film. Figure 6.11A is an image of a large scale

network in the same region as figure 6.10A. The dense oxidised particles show up as bright agglomerates. In the bottom and right of the image there is an out-of-focus feature which is attributed to either a piece of broken carbon film which is bending out of the focus plane or some  $\text{LiMo}_3\text{Se}_3$  network material that is not in the plane of the main image due to the geometry in which it was suspended in solution.

Figures 6.11 B and C are two magnified images of junctions of material displayed in the main image, A. It is apparent from these magnified images that most of these network “junctions” are not actually networked in the way seen in section 4.3.2 where bundles splay out and constituent wires join up with other bundles, but instead consist of intertwining and overlapping bundles. The inset shows a section based on the Z-contrast of the image in figure 6.11C. A distinct and clear increase in intensity is observed about the centre of this junction, in stark contrast to junctions formed from pristine  $\text{LiMo}_3\text{Se}_3$  solutions which have been imaged by AFM which show no increase in height throughout a network (section 4.3.2).

Figure 6.12 contains an EDX spectrum of an area of network shown in figure 6.11C. As noted in figure 6.11C, the Z-contrast section shows this is an area of overlapping bundles. The EDX spectrum shows low intensity Mo and Se peaks, which are dominated by C and Cu peaks, but indicate that the features observed in STEM are  $\text{LiMo}_3\text{Se}_3$ .

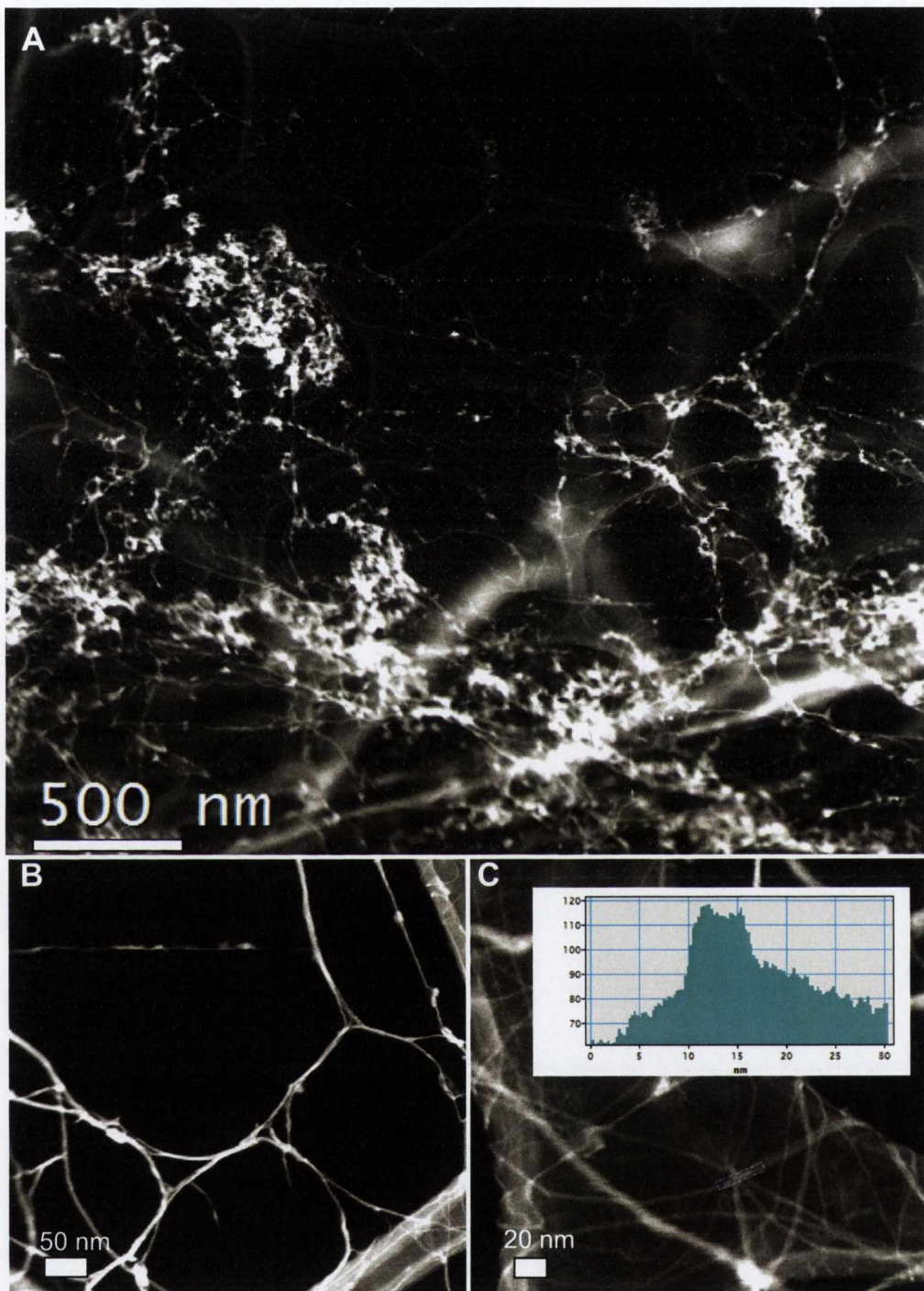


**Figure 6.11.** *A: STEM image of freeze-dried unfiltered aqueous  $\text{LiMo}_3\text{Se}_3$  on lacy carbon TEM grid. B and C: magnified image of wires. Inset on C corresponds to the blue box on image C*

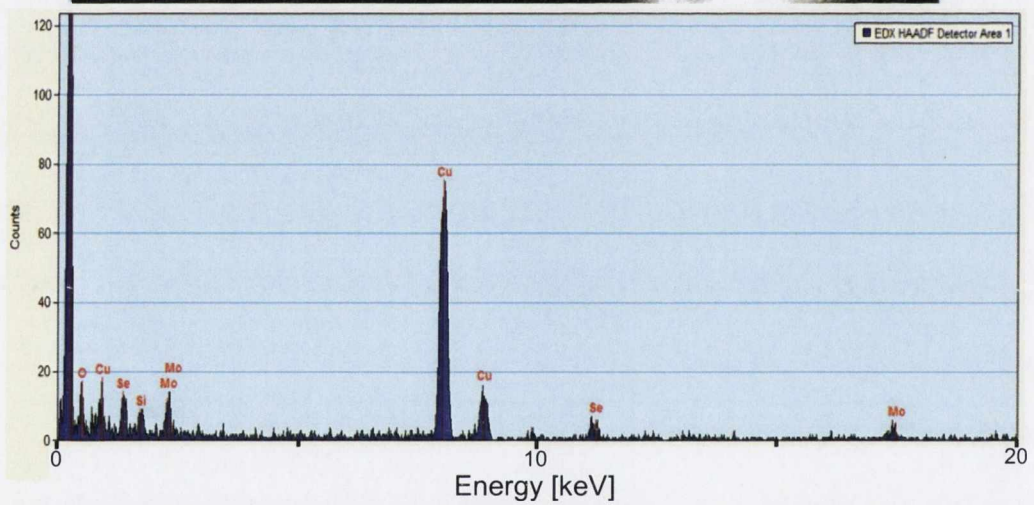
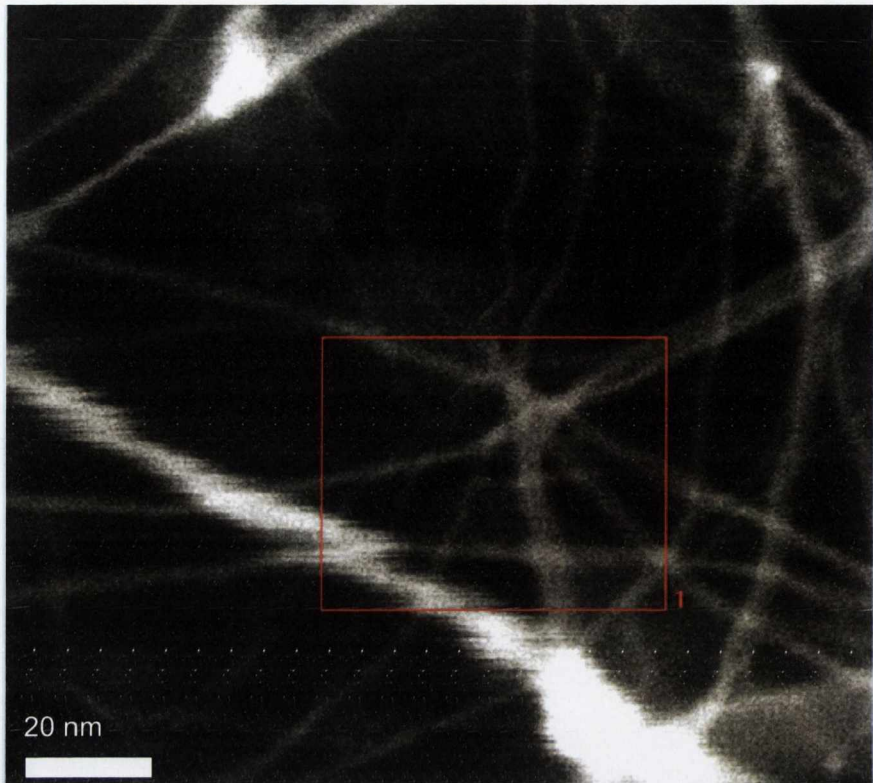


**Figure 6.12.** STEM image of freeze-dried unfiltered aqueous  $\text{LiMo}_3\text{Se}_3$  on lacy carbon TEM grid, showing an area of overlapping wires and the EDX spectrum of the area in the red box

Figure 6.13 shows a STEM image and EDX linescan analysis of an area of this network. By recording EDX spectra along a line and then plotting position vs. counts for a given energy window, a line profile of the intensity of that element along the line can be obtained. The red line marked “1” on the image corresponds to the series of plots on the right hand side of this image.

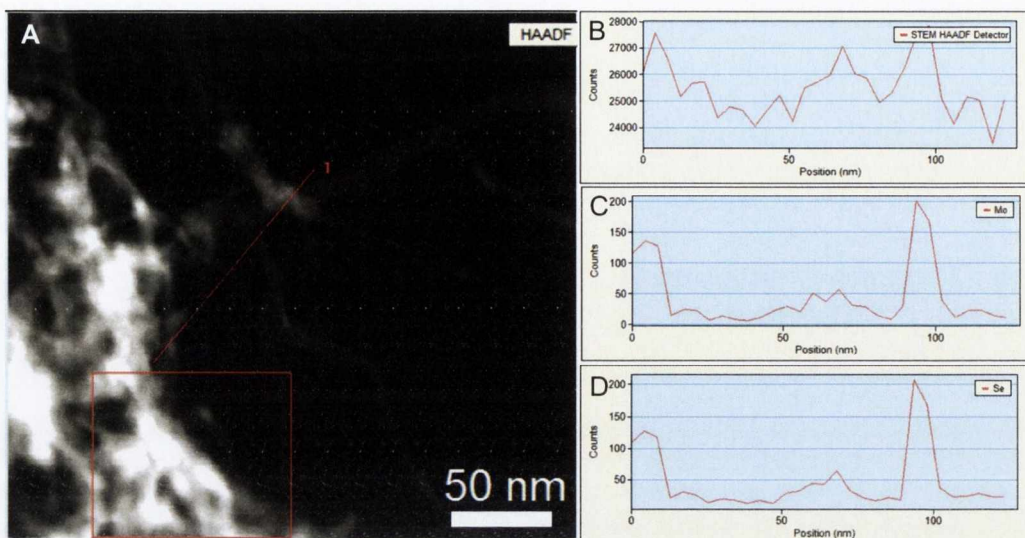


**Figure 6.13.** STEM image of freeze-dried unfiltered aqueous  $\text{LiMo}_3\text{Se}_3$  solution. EDX analysis carried out along the red line in the image. B: total EDX signal along the linescan, C: Mo signal along the linescan, D: Se signal along the linescan

The X axis is positioned along this line and the Y axis displays EDX signal counts. Figure 6.13B shows the overall number of counts along this linescan. Figure 6.13C shows the variation in the Mo peak intensity along the line. The two peaks correspond to the dense area of agglomerated material on the left hand side of the image and the second (small) and third (large) peaks correspond to the network areas which intersect with the linescan. Figure 6.13D shows a similar profile for Se along this linescan.

### 6.3.3 Electron microscopy of freeze-dried filtered $\text{LiMo}_3\text{Se}_3(\text{DMSO})$ solutions

High resolution STEM images of filtered  $\text{LiMo}_3\text{Se}_3(\text{DMSO})$  solutions cast onto TEM grids without freezing (chapter 5, figure 5.3, formed by drop casting on lacy carbon film TEM grid followed by vacuum pumping to remove the non-volatile solvent) showed the presence of network, small pristine nanowire bundles, and the absence

of large crystallite bundles. From these images as well as light scattering and rheology data, it seemed likely that solutions of  $\text{LiMo}_3\text{Se}_3$  have a polydispersed size distribution of larger crystallite bundles, smaller nanowires and wire fragments which are involved in the formation of network. In the images of the filtered solutions (figure 5.3) no large bundles were present (these would not pass through the  $0.45\ \mu\text{m}$  PTFE filters used). From these data, it seems reasonable to expect that if the network were present in solution, it would also not pass through these filters. To confirm this, a solution of  $\text{LiMo}_3\text{Se}_3$  with DMSO as a solvent was prepared in an inert atmosphere and filtered using the same  $0.45\ \mu\text{m}$  PTFE filters. The sample was prepared as normal for cryo-TEM (pipette a drop onto a lacy carbon TEM grid, blot and plunge into liquid ethane) and introduced it to the system on a cold (LN2) stage. The sample was left in the TEM chamber to warm overnight, allowing the sample to freeze-dry, so that when it was imaged the next morning a representation of the composition of a filtered solution could be obtained. This experiment was motivated by the images of the freeze-dried samples shown in figures 6.10 and 6.11 which contained features similar to those of pristine nanowire networks.

Conventional TEM images of the freeze-dried, filtered sample are shown in figure 6.14. The main image, A, is a low magnification overview of the network which was observed on these samples. Figures 6.14B and C are higher magnification TEM images of junctions of the network displayed in A. Both show evidence of overlapping wires and of “networked” wires, especially in image C where, toward the bottom of the image a nanowire can be seen to run underneath two others. Also, in the centre of the image there appears to be a pristine junction where one bundle is splaying into two.

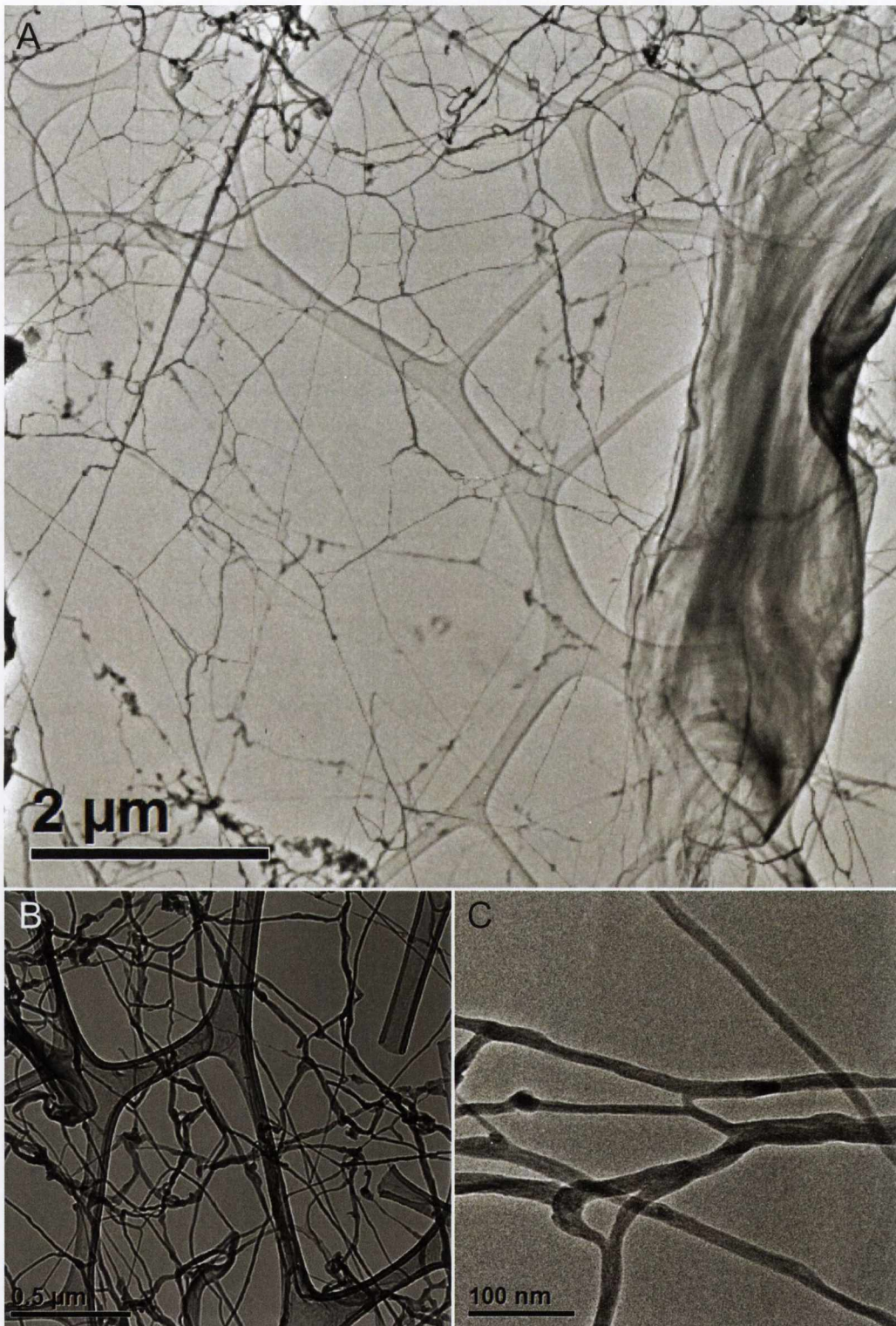


**Figure 6.14** TEM images of freeze-dried, filtered  $\text{LiMo}_3\text{Se}_3(\text{DMSO})$  solution on lacy carbon TEM grid

In figure 6.15, two TEM images of a junction of pristine material are visible. The main image shows a length of nanowire bundle running diagonally through the

image. Individual  $\text{LiMo}_3\text{Se}_3$  strands are visible along its length. At either end, the bundle is clearly splaying out into junctions.

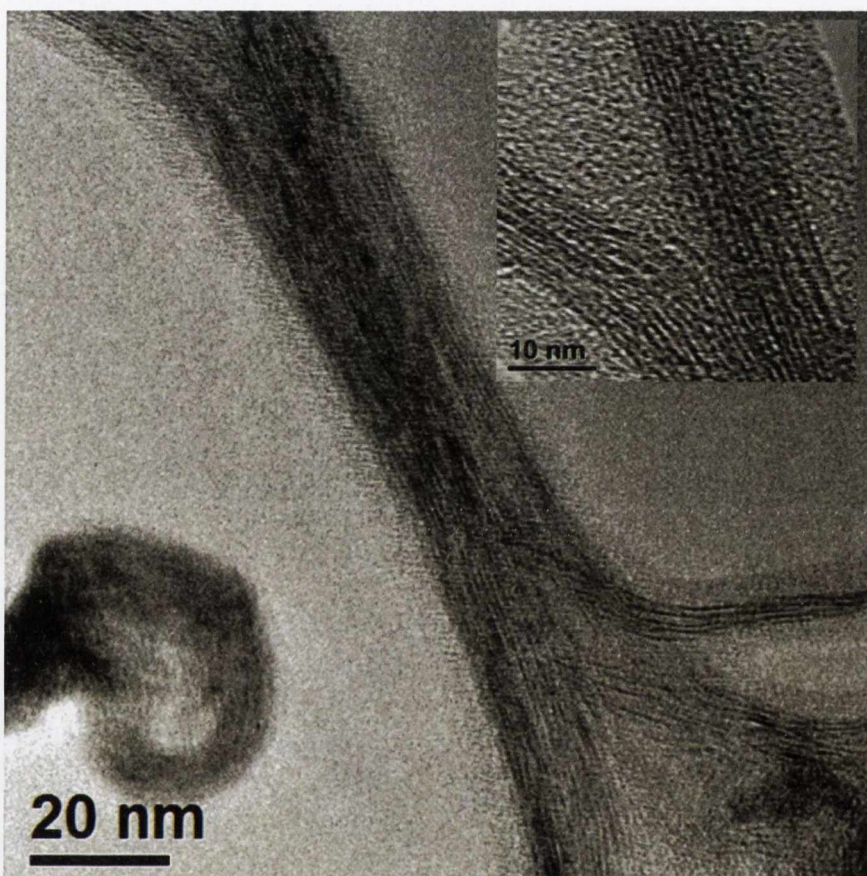


**Figure 6.15.** TEM image of a junction of  $\text{LiMo}_3\text{Se}_3$  formed on a lacy carbon TEM grid during freeze drying of the filtered  $\text{LiMo}_3\text{Se}_3(\text{DMSO})$  solution in the TEM chamber. Inset shows a magnified view of the junction in the top left hand side of the main image

The inset of figure 6.15 is a magnified image of the junction visible in the top left hand corner of the main image. Individual nanowire chains are again visible within the bundles and the junction in this case is clear and abrupt.

STEM imaging of this area (figure 6.16) shows similar features as those observed in figure 6.14A. The Z-contrast of this image shows that certain areas appear much brighter than the surrounding wire material (the agglomerates in the centre and right hand side of the image for example) indicating that these  $\text{LiMo}_3\text{Se}_3$  material areas



are significantly denser than the surrounding network. They also bear a resemblance to images of oxidised materials (section 6.3.2). It is possible that this sample's parent solution oxidised during transit or during sample preparation.

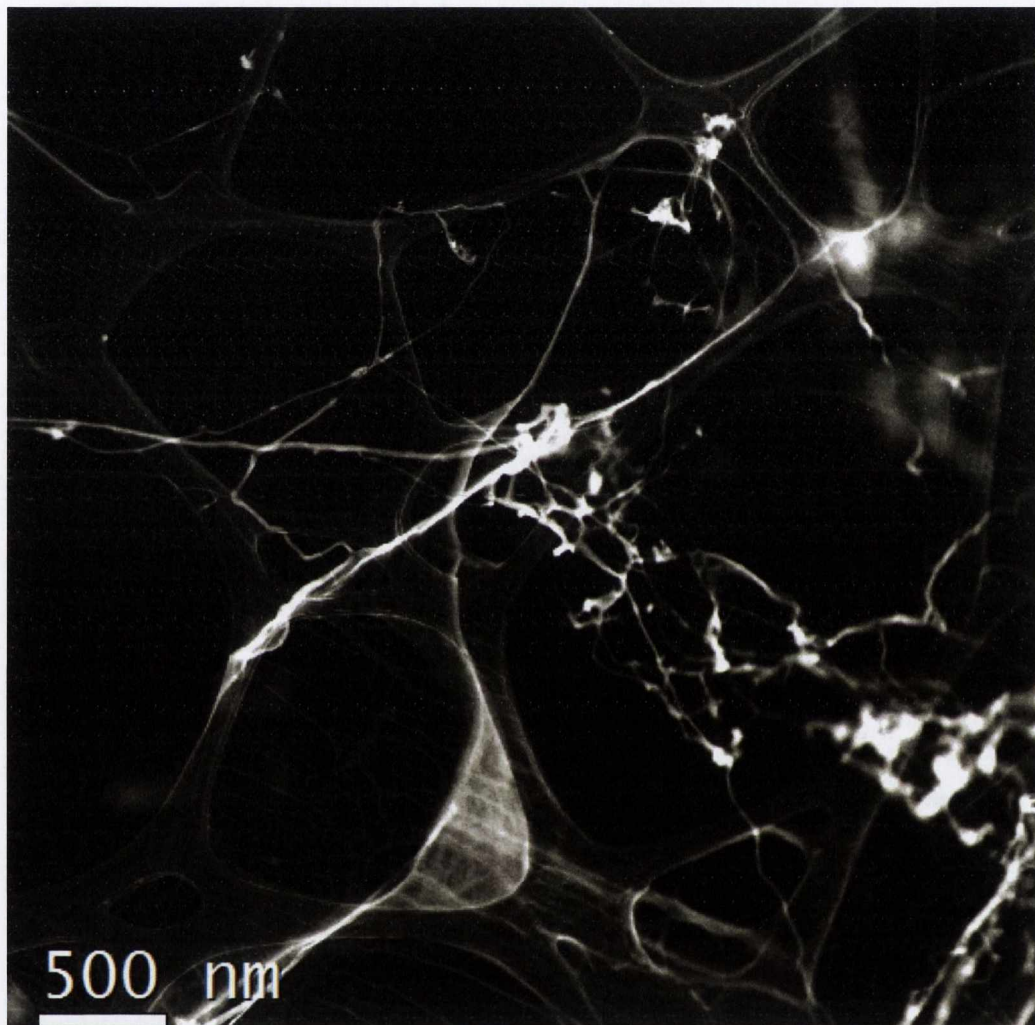


**Figure 6.16** STEM image of freeze-dried filtered  $\text{LiMo}_3\text{Se}_3(\text{DMSO})$  solution on lacy carbon TEM grid

In figure 6.17 a STEM image and an EDX spectrum corresponding to the red box on the image are displayed. The image is of an area of “clean” network, i.e. there are no obvious agglomerates in the image. The EDX spectrum shows the presence of Mo and Se within the area analysed. Large O and C peaks are also noted, which can be accounted for by the presence of solvent residue on the network, oxidised  $\text{LiMo}_3\text{Se}_3$ ,

or the carbon support film on the TEM grid. There are also Cu peaks present which are due to the TEM grid.

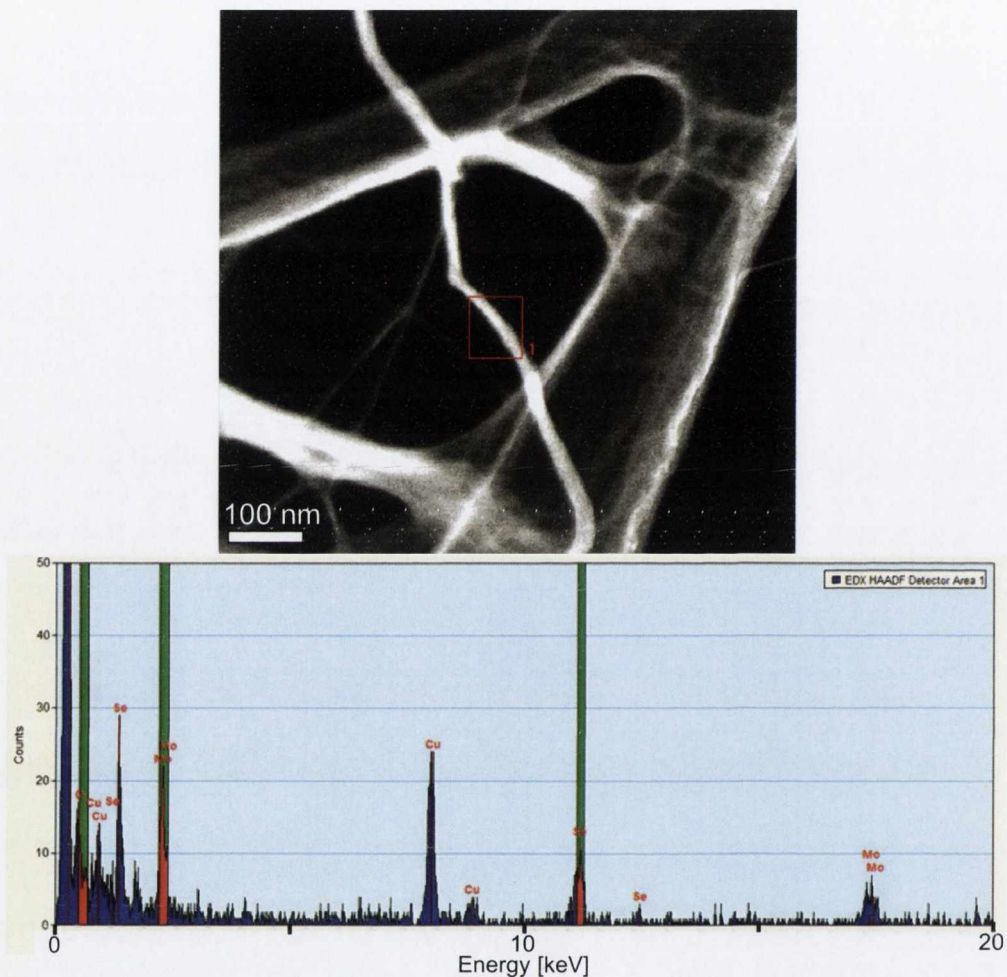


**Figure 6.17** STEM image of freeze-dried filtered  $\text{LiMo}_3\text{Se}_3(\text{DMSO})$ . EDX spectrum corresponds to red box in image

Figure 6.18A shows an image of a networked area containing agglomerated particles and the EDX linescan analysis of this area. Figure 6.18B shows a linescan of EDX spectra intensities along the red line marked “1” in the image. This linescan is unfiltered and the Y axis is the total number of counts over all recorded energy ranges for each spectrum obtained along this line. Figures 6.18C, D and E are the linescans where only the intensity for the signal about the Mo, Se and O peaks, respectively, are displayed. C, D, and E all show low intensities towards the end of

the linescan where the position of the electron probe was over vacuum. Towards the centre of the linescan a “double-hump” peak is noted in all cases, indicating that the bright, high Z-contrast areas of the agglomerate which intersect the red line are oxidised  $\text{LiMo}_3\text{Se}_3$  materials.

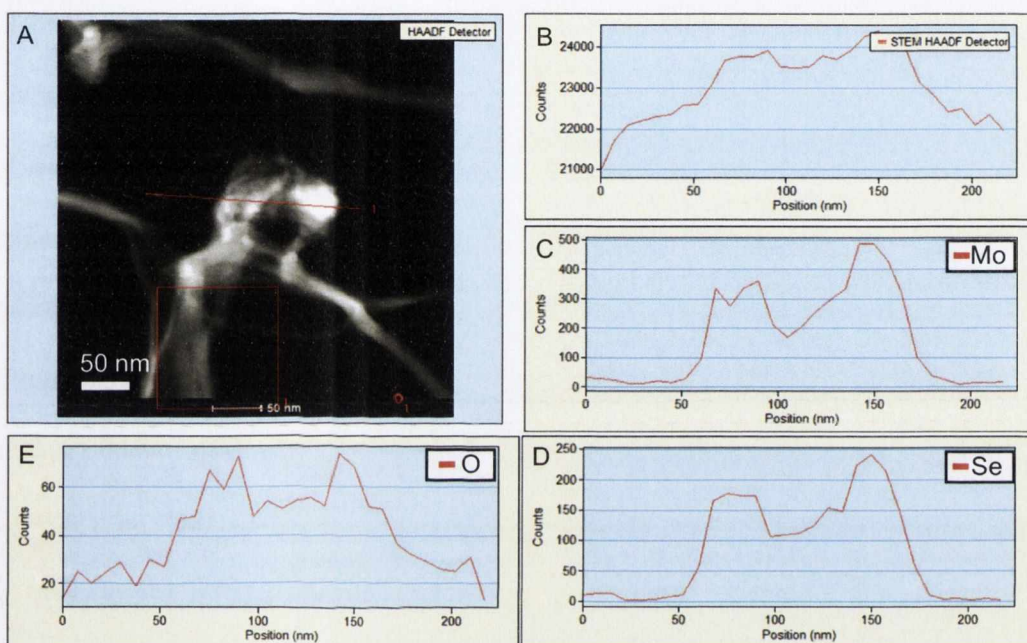


**Figure 6.18** STEM image (A) and EDX linescans (B-E) of freeze-dried filtered  $\text{LiMo}_3\text{Se}_3(\text{DMSO})$ . B: total EDX signal along the linescan, C: Mo signal along the linescan, D: Se signal along the linescan, E: O signal along the linescan. Linescans correspond to the red line on image A

## 6.4 Conclusions

Herein, the investigation of samples of frozen  $\text{LiMo}_3\text{Se}_3(\text{DMSO})$  solutions is discussed. From these samples nanowire fragments were visible in the suspended frozen matrix, both in TEM and STEM imaging modes. EDX analyses of these areas showed the presence of Mo and Se, confirming that the particles visible are  $\text{LiMo}_3\text{Se}_3$ . Areas rich in  $\text{LiMo}_3\text{Se}_3$  were observed to be sputtered away by repeated imaging with the electron beam resulting in a loss of nanowire signal in the EDX spectra of these areas. Freeze drying of these  $\text{LiMo}_3\text{Se}_3(\text{DMSO})$  solutions resulted

samples containing some areas which resemble pristine network, however it was not possible to obtain sufficiently high resolution images of these samples to say whether junctions in this network are overlapping/intertwining bundles or junctions formed of splaying nanowire bundles .

Samples prepared from  $\text{LiMo}_3\text{Se}_3(\text{aq})$  solutions were also investigated.  $\text{LiMo}_3\text{Se}_3$  particles were again noted suspended within the frozen matrix. However, in this instance, it was noted that repeated imaging of an area rich in  $\text{LiMo}_3\text{Se}_3$  caused the distribution of  $\text{LiMo}_3\text{Se}_3$  particles to change. The most likely cause of this observed change is that the presence of the electron beam causes the solvent to be removed by sputtering, freeing the embedded particles to move and agglomerate. Although these features are similar in appearance to a pristine network, they are actually agglomerates of  $\text{LiMo}_3\text{Se}_3$  particles.

Whole nanowire bundles were also observed the sample prepared from the aqueous solution. Unlike samples prepared for TEM without freezing or freeze-drying, the bundles were not stable under the electron beam, and they appeared to fragment with continued exposure. This sample also contained amorphous agglomerates. These agglomerates most likely consist of oxidised  $\text{LiMo}_3\text{Se}_3$  material given the solvent used ( $\text{H}_2\text{O}$ ). EDX analyses confirm the presence of Mo, Se and O in the samples, however, given the variety of materials which are likely to contain oxygen in this sample (oxidised wire material, solvent, carbon support film) it is not possible to ascribe the oxygen peak in the spectra solely to the presence of oxidised wire material. However, the agglomerates observed do bear a striking resemblance to

images obtained from a sample of  $\text{LiMo}_3\text{Se}_3$  dissolved in DMSO which had been deliberately air-exposed.

The freeze-dried sample of aqueous  $\text{LiMo}_3\text{Se}_3$  solution revealed large scale network. However closer examination of the images of this sample revealed that junctions of this network consist of overlapping/intertwining bundles rather than the junctions observed in a pristine network in chapter 4, i.e. bundles which splay at their ends and branch out into other areas of the network. Oxidised material is also visible in these images and EDX confirms the presence of Mo, Se and O in the material analysed. It is likely that these networks form from nanowires present in the frozen matrix which cross each other as the solvent sublimates.

Thus far, the analysis of the frozen nanowire solutions confirms the presence of  $\text{LiMo}_3\text{Se}_3$  particles and nanowires throughout the solution. There has been no direct imaging of pristine network suspended in the frozen medium. The features noted in figure 6.7 bear some resemblance to pristine network, but the exact topography of these is unclear. Even if these features are pristine network, there is not enough present to account for the large scale networks (non-pristine) observed in the freeze-dried samples. As previously noted, (chapter 5), when filtered solutions were cast on TEM grids, continuous pristine networks and no large bundles were observed. Because large bundles cannot pass through the  $0.45\ \mu\text{m}$  PTFE syringe filters used, it seems unlikely that a pristine network would be able to pass the same filter if it were in solution. To confirm that these networks were not present in solution a filtered  $\text{LiMo}_3\text{Se}_3(\text{DMSO})$  solution was prepared and was sent for cryo-imaging. The intention was to prepare the frozen sample (drop, blot, and freeze) and then allow it to freeze-

dry in the TEM system overnight. Small wires and wire fragments were expected to be observed with no network present. If network were observed, it would be the non-pristine variety, i.e. overlapping/intertwining wires. However a large scale feature similar to the networks seen in chapter 4 was observed. In addition to simple overlapping wires some of the junctions displayed “splaying” (where a bundle branches out into two or more, smaller bundles, figure 6.15) the hallmark of networks observed in chapter 4. This would indicate the possibility that networks form very quickly on contact with a surface (when the solution is dropped on the TEM grid just prior to blotting and plunging in liquid ethane) or that there is some mobility of the nanowire material during the freeze-drying process. As we have previously noted the presence of network spanning over large bundles (figure 4.3) and the “quenching” of network formation by rapid pumping of drop cast samples (chapter 4 .14) it seems highly unlikely that networks are forming instantly upon contact with a surface indicating that some there is some mobility the nanowire material during the freeze-drying process.

## 6.5 References

- [1] Gatan\_Inc, [www.gatan.com/pdf/Cryoplunge.pdf](http://www.gatan.com/pdf/Cryoplunge.pdf) **2000**.
- [2] O. Balmes, J.-O. Malm, G. Karlsson, J.-O. Bovin, *Journal of Nanoparticle Research* **2004**, 6, 569.
- [3] NIST\_Chemistry\_webbook, <http://webbook.nist.gov/chemistry/>.
- [4] H. L. Clever, E. F. Westrum, *The Journal of Physical Chemistry* **1970**, 74, 1309.
- [5] T. B. Douglas, *Journal of the American Chemical Society* **1948**, 70, 2001.

- [6] D. B. Hibbert, A. C. C. Tseung, *Journal of Materials Science* **1979**, *14*, 2665.
- [7] M. Bonini, S. Rossi, G. r. Karlsson, M. Almgren, P. Lo Nostro, P. Baglioni, *Langmuir* **2006**, *22*, 1478.
- [8] J.-O. Bovin, T. Huber, O. Balmes, J.-O. Malm, G. Karlsson, *Chemistry – A European Journal* **2000**, *6*, 129.

## Chapter 7

# Electron Microscopy of ion-exchanged

# $X^+ \{Mo_3Se_3\}^-$ networks

### 7.1 Introduction

In this chapter the structural characteristics of ion-exchanged  $X^+ \{Mo_3Se_3\}^-$  networks are described. These networks form in solution when  $LiMo_3Se_3$  nanowires are treated with a positively charged organic ligand and a crown-ether which complexes the  $Li^+$  ion of the nanowires and facilitates ion-exchanged network formation. The product forms as a precipitate which is then placed on a copper TEM grid and dried prior to imaging. Transmission Electron Microscopy (TEM) and Scanning Transmission Electron Microscopy (STEM) studies of ion-exchanged nanowire networks,  $X^+ \{Mo_3Se_3\}^-$  are presented. In addition Electron Energy Loss Spectroscopy (EELS) of the  $Surf_3 \{Mo_3Se_3\}$  samples is also presented.

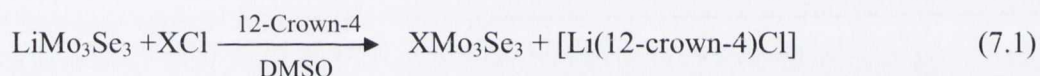
Ion-exchanged  $X^+ \{Mo_3Se_3\}^-$  networks are of interest as the  $LiMo_3Se_3$  system is prone to degradation in ambient conditions. The ligands used here were selected to hinder the oxidation of the  $\{Mo_3Se_3\}$  wire strands as shown in the work of Heidelberg et al[1], essentially the idea is to create an array of self-organizing, Teflon<sup>TM</sup> coated wires. Once the corrosion issue is dealt with, these self-organized nanowire arrays could have many applications, noticeably in composites given the method of their synthesis.



## 7.2 Background

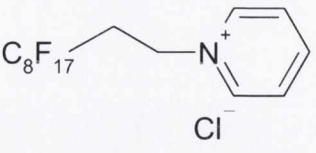
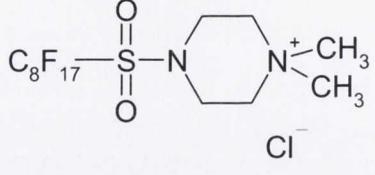
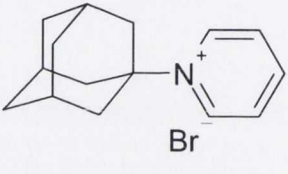
The preparation of these  $X^+ \{Mo_3Se_3\}^-$  networks has been described elsewhere (section 3.4) but can be described briefly as follows:

The  $Li^+$  ion of the  $LiMo_3Se_3$  nanowire can be replaced by similarly charged cations, in this case organic ligands with positively charged headgroups with long or voluminous aliphatic hydrocarbon tails.[2, 3]



A  $LiMo_3Se_3(DMSO)$  solution is mixed with a two-fold excess of surfactant X (with respect to the concentration of the  $Li^+$  counter-ion of the  $\{Mo_3Se_3\}_\infty$  strand). To hasten the reaction a two-fold excess of 12-crown-4 is also added.[4] The crown ether serves to complex the  $Li^+$  ion, driving the reaction toward the ion-exchanged nanowire network product, which is an ordered assembly of surfactant/ $(Mo_3Se_3)_\infty$  units.

The positively charged ligands used to form ion-exchanged networks for high resolution TEM studies are shown with their anion in table 7.1. Their colloquial names (Surf 3, Surf 4, etc.) are also listed.

| Name      | Ligand   | Structure  |
|-----------|--|--|
| Surf 3    | 1-H, 1-H, 2-H, 2-H – Perfluorodecyl-pyridiniumchloride               |  |
| Surf 4    | N', N'- dimethyl – N – (perfluorooctansulfonyl)-piperaziniumchloride |  |
| Surf 5    | 1-(1-Adamantyl)-pyridiniumbromide                                    |  |
| Surf Thio | 2-Aminoethanthiol Hydrochloride                                      | $\text{H}_2\text{N}-\text{CH}_2-\text{CH}_2-\text{SH} \cdot \text{HCl}$            |

**Table 7.1** Ligands used to prepare ion-exchanged networks

Figure 7.1 also shows a ball and stick schematic of the ion-exchanged product. Because the  $\text{Li}^+$  ions have been complexed by the crown-ether, the positively charged ligands replace them on the surface of the individual, negatively charged nanowire chains. Due to the size and low solvation energy of the ligands, the coated nanowire strands no longer remain in solution but instead precipitate. The ligands used are considerably larger than the original Li cations which results in an increased interwire spacing relative to a pristine  $\text{LiMo}_3\text{Se}_3$  nanowire bundle. The actual interwire spacing should then be dependent on the ligand used, consistent with the results presented below (table 7.2).

The products can be thought of as molecular chains of  $\{\text{Mo}_3\text{Se}_3^-\}_\infty$  surrounded by hydrophobic surfactant tails. To preserve electroneutrality, each  $\text{Li}^+$  ion complexed

by the 12-crown-4, is replaced on by a positively charged  $X^+$  surfactant. It is the hydrophobic nature of the surfactant tails that causes the sheathed molecular chains to reassemble into the observed mesostructures described below.[2] There are two typical mesostructures, a hexagonal array which can be thought of as a “bloating” of the  $LiMo_3Se_3$  crystal structure and a lamellar type structure where the ligands attach to the wire strand in such a way that they are  $180^\circ$  opposed to each other. As the ligands bond to the wire surface it is likely that they arrange themselves in such a way as to keep steric interferences to a minimum by having nearest neighbour ligands attach at exactly opposite sides of the wire. In both cases there is an expected degree of interdigitation of the ligands used (figure 7.1). The ion-exchanged networks formed here are of the lamellar variety and form two-dimensional ribbon like structures due to the interdigitation of the hydrophobic ligand tails.

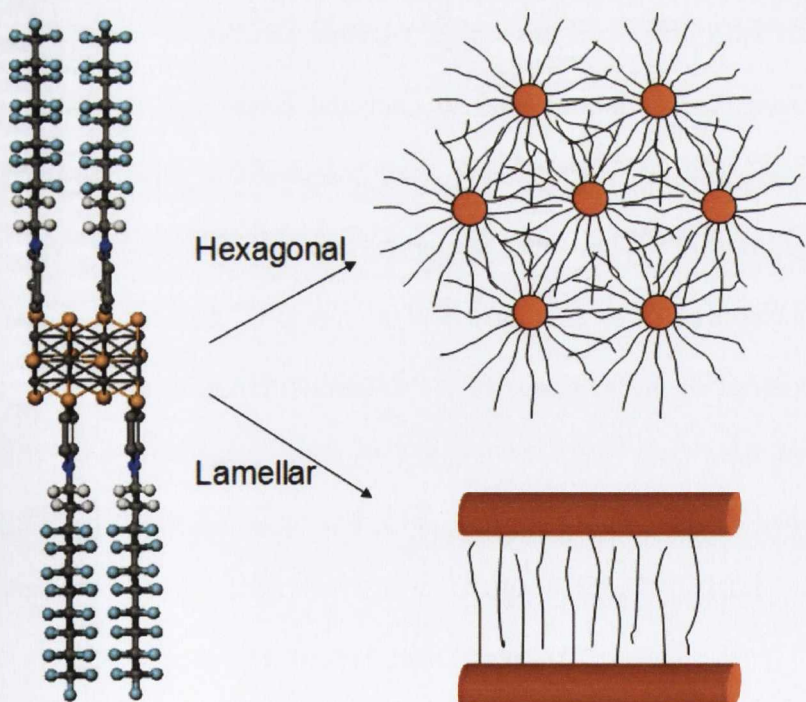


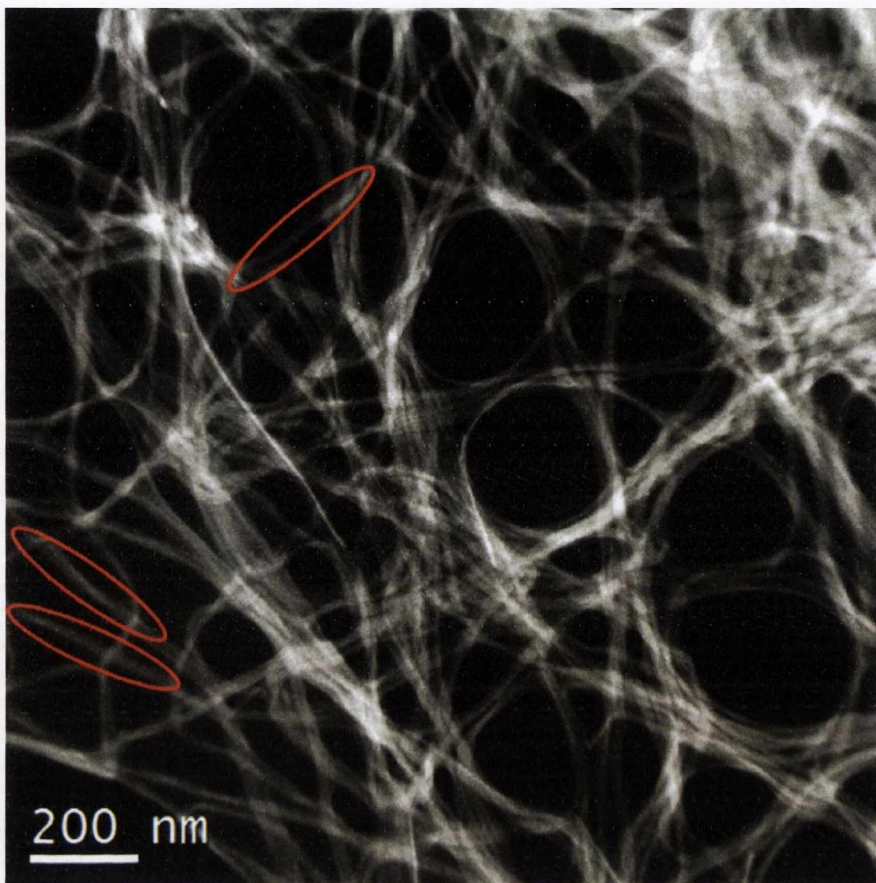
**Figure 7.1:** LEFT: Ball and stick cartoon of ligands attached to a segment of a  $\{Mo_3Se_3\}_\infty$  chain). RIGHT possible resultant hexagonal and lamellar structures

## 7.3 Characterisation

### 7.3.1 Characterisation of Surf 3 {Mo<sub>3</sub>Se<sub>3</sub>} networks

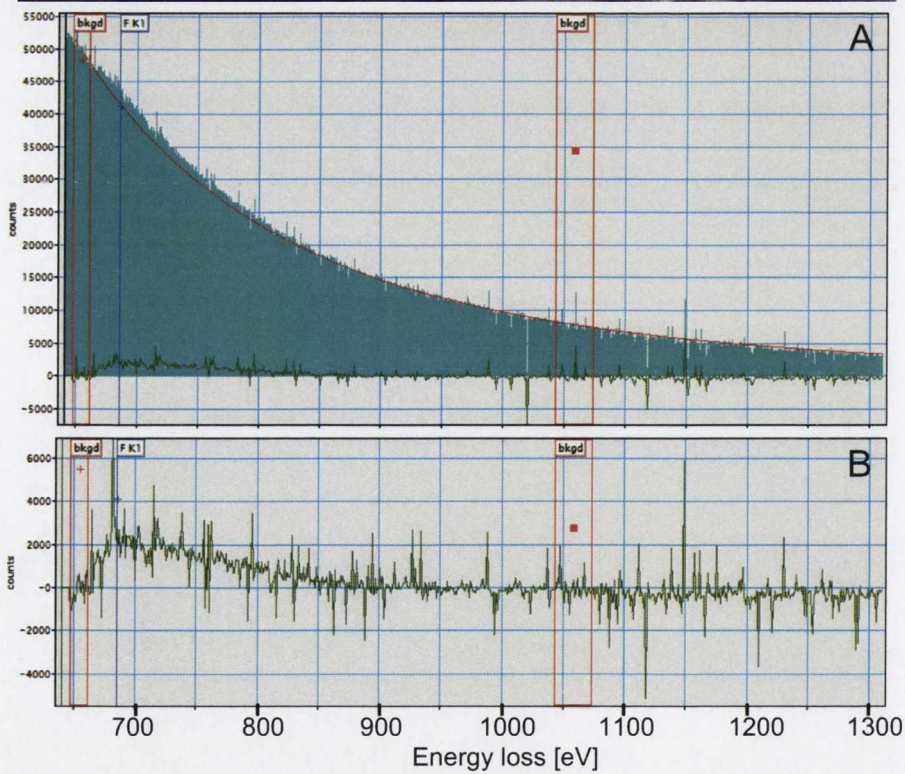
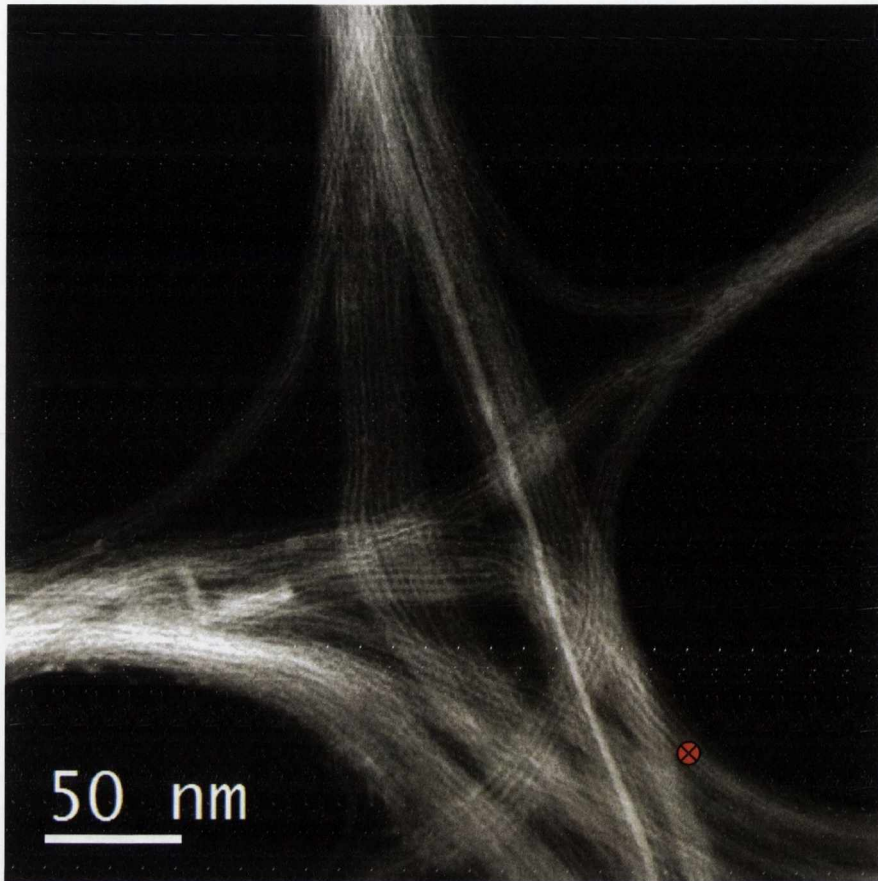
Samples were prepared from a  $10^{-3}$ M LiMo<sub>3</sub>Se<sub>3</sub> solution in DMSO. A small amount of the precipitated product was washed in DMSO and placed on a lacy carbon TEM grid and dried. The sample was imaged at the SuperSTEM facility at the Daresbury UK Labs in collaboration with Dr. P.D. Nellist using the SuperSTEM1, a modified VG system, with aberration correction and an electron energy loss spectrometer (EELS). The sample was imaged at 100 kV throughout. Images were recorded using a HAADF (High Angle Annular Dark Field) detector, giving real atomic mass (*Z*) contrast to the images.[5]

Figure 7.2 shows an area of the network suspended over the lacy carbon film which can be seen in the background. In this image a coarse network of ion-exchanged ribbons can be seen. These ribbons tend to knot and cross each other and the junctions of this network are not continuous as observed for networks of bare LiMo<sub>3</sub>Se<sub>3</sub>, i.e. in LiMo<sub>3</sub>Se<sub>3</sub> the networks are formed from bundles splaying out into their constituent nanowires which then form network junctions. This is evidenced by the increase in contrast of the junctions in the *Z*-contrast HAADF images (figure 7.2). These ribbons form from LiMo<sub>3</sub>Se<sub>3</sub> bundles which have been stripped of their Li cations and replaced with an organic ligand, in this case a perfluorinated alkyl chain with a pyridinium headgroup.



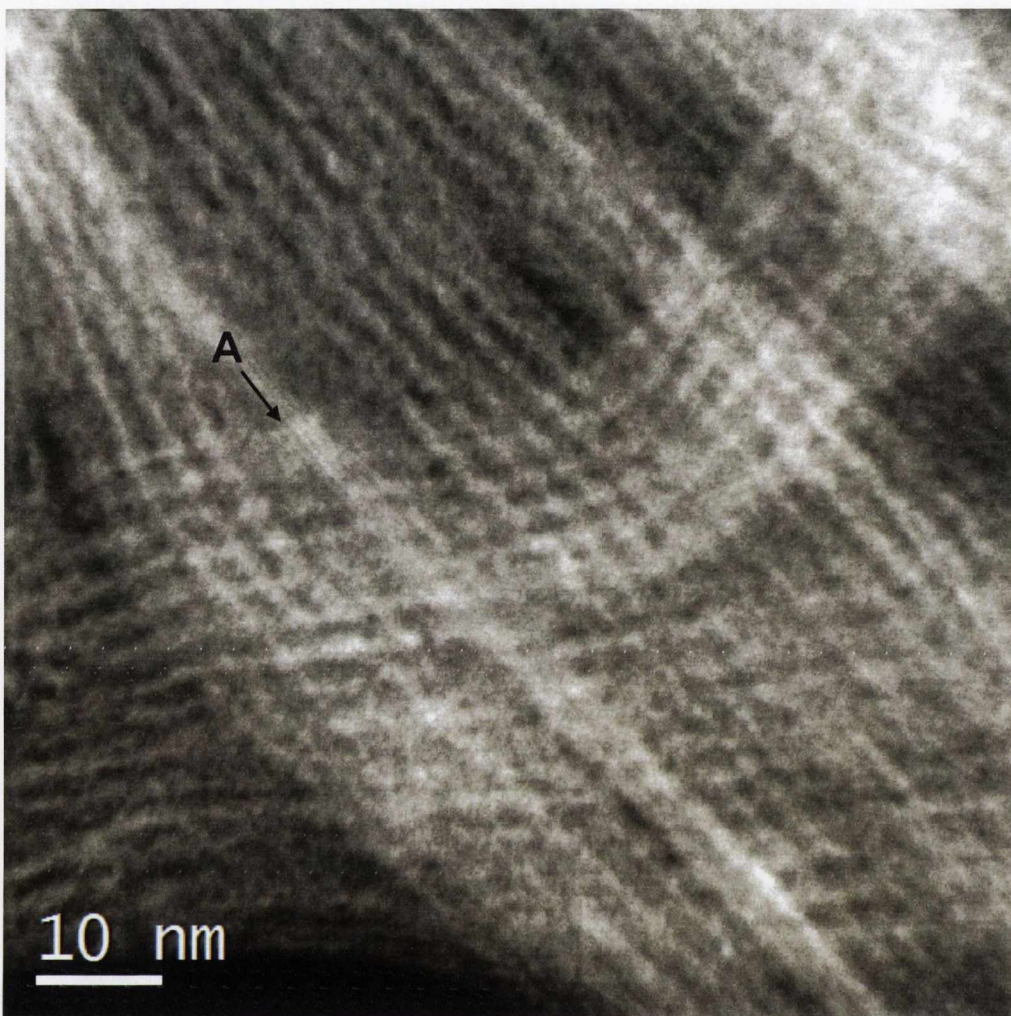
**Figure 7.2:** STEM image of Surf3{Mo<sub>3</sub>Se<sub>3</sub>}. Long strands (examples circled in red) of the ion-exchanged network visible on a carbon support film.

Figure 7.3 shows an area of network which was selected for EELS analysis. The red cross on the bottom right hand side of the image indicated where the spectrum was obtained. The EEL spectrum recorded from this region (red spot on image) is shown in figure 7.3A. The background subtracted spectrum is shown in figure 7.3B and the fluorine K edge at an energy loss of 685 eV is visible. For this sample the end chain of the Surf 3 is a perfluorinated alkyl chain and the presence of the fluorine in the spectrum shows that the  $\{\text{Mo}_3\text{Se}_3\}_\infty$  chains in this image have been stripped of their  $\text{Li}^+$  ions and replaced with surfactant ligands.



**Figure 7.3:** STEM image of an area of Surf3{Mo<sub>3</sub>Se<sub>3</sub>}. Inset A shows the EEL spectra obtained at the point marked with the red cross in the image. Inset B shows the background subtracted spectrum and shows the fluorine K edge (blue).

Figure 7.4 shows a magnified area of the sample in figure 7.2. Immediately apparent are the regular  $\{\text{Mo}_3\text{Se}_3\}^\infty$  chains running parallel to one another. The interwire spacing is  $2.71 \pm 0.04$  nm and considerably larger than that of a pristine  $\text{LiMo}_3\text{Se}_3$  bundle (0.85 nm). Other than areas where there are two overlying ribbons running in different directions (bottom half of image), the contrast of neighbouring chains appears constant. These data indicate the structures are ribbon-like lamellar structures such as those shown in figure 7.1. In the case of a hexagonal structure, an increase in contrast would be expected towards the centre of a ribbon where there would be more material present. Further PXRD experiments are needed to confirm this structure.



**Figure 7.4:** Surf3{Mo<sub>3</sub>Se<sub>3</sub>} higher magnification image of the area displayed in figure 7.2. An unreacted Mo<sub>3</sub>Se<sub>3</sub> crystallite can be seen running diagonally through the network (marked A)

To get a sense of the expansion that occurs following ion exchange Fig 7.4 shows a pristine unreacted bundle running diagonally across the centre of the image (marked as “A” on figure 7.4). This offers a clear comparison of the difference in interwire separation between the exchanged and non-exchanged species (see figure 7.5 for a higher magnification view). This pristine bundle could be one of three things: a LiMo<sub>3</sub>Se<sub>3</sub> bundle which has not undergone ion-exchange with the surfactant ligand, a LiMo<sub>3</sub>Se<sub>3</sub> bundle which still contains a large amount of In which was not removed

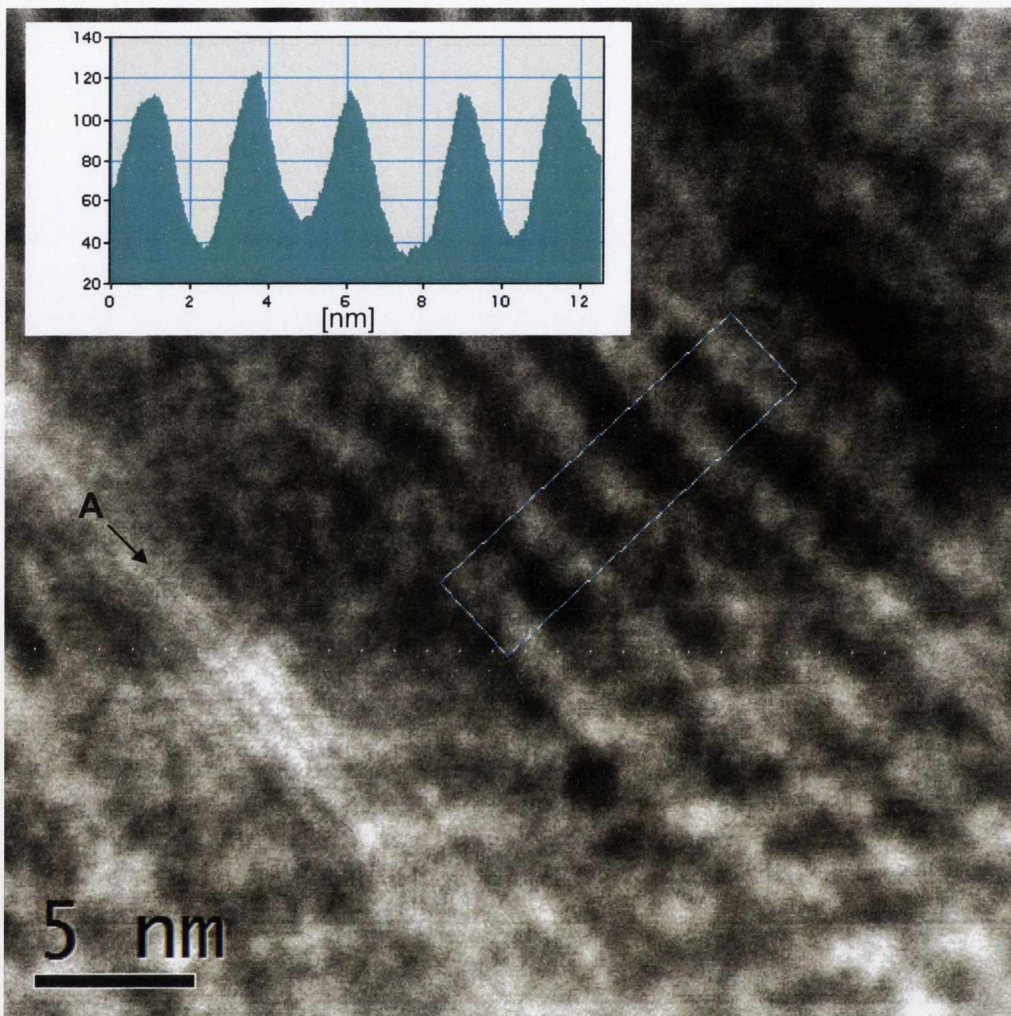


during  $\text{LiMo}_3\text{Se}_3$  synthesis (i.e.  $\text{Li}_x\text{In}_{1-x}\text{Mo}_3\text{Se}_3$ ) or an  $\text{InMo}_3\text{Se}_3$  crystallite which did not undergo chemical transport as per the reaction:



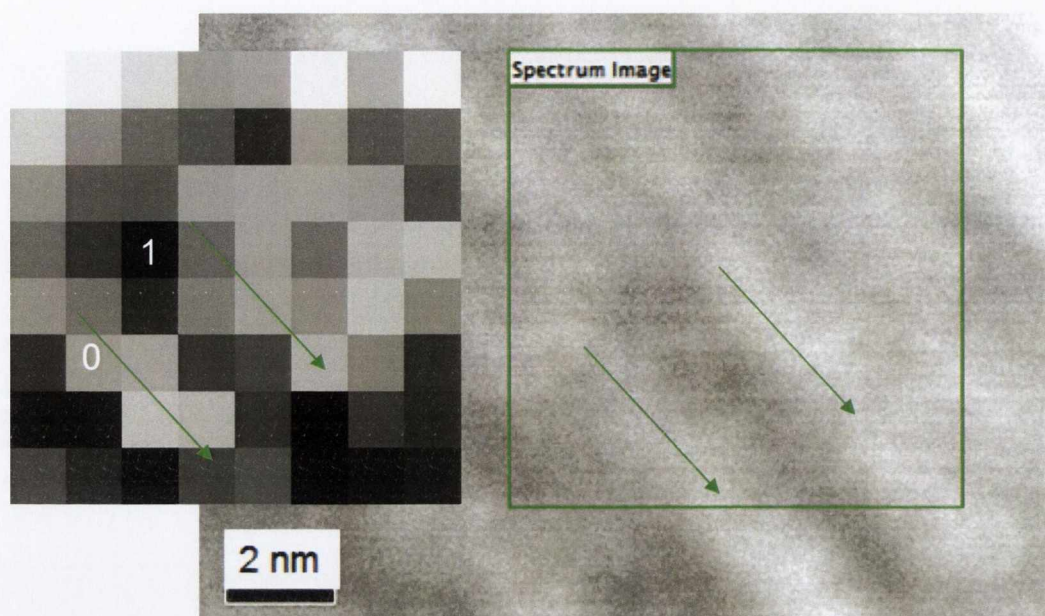
during  $\text{LiMo}_3\text{Se}_3$  synthesis (section 3.2).

Figure 7.5 is a further magnified image of  $\text{Surf3Mo}_3\text{Se}_3$  displayed in figure 7.4. The inset is a cross section based on the colour intensity (z-contrast) of the image which correlates to the blue rectangle drawn on the image. An interwire separation of  $\sim 2.71$  nm is measured (this cross section shown, figure 7.5 inset, is for representative purposes only, the actual value is the average of 54 measurements on a series of images acquired from this sample). It is clear from this image that the interwire separation of the ion-exchanged network has increased relative to the separation in a pristine bundle (2.71nm vs. 0.85 nm respectively). Higher resolution of individual  $\{\text{Mo}_3\text{Se}_3\}_\infty$  strands in these samples was not possible, even though they proved relatively easy to obtain for pristine  $\text{LiMo}_3\text{Se}_3$  nanowire samples (section 4.3.1).[7] This difficulty in imaging is attributed to the fact that the  $\{\text{Mo}_3\text{Se}_3\}_\infty$  strands are now densely coated with organic ligands resulting in a loss of image resolution.



**Figure 7.5:** Surf3{Mo<sub>3</sub>Se<sub>3</sub>}, magnification of the area in figure 7.4. Crystallite A is clearly visible. Inset shows a cross section of the area in the blue rectangle

Figure 7.6 shows a EELS spectrum image which was attempted on a portion of the area shown in figure 7.5.[8] Sixty four EEL spectra were recorded on different locations of the area enclosed by the green square on figure 7.6. Each of these is represented by one pixel in the spectrum image. The spectra were recorded between 480 eV and 1150 eV. By taking a “slice” of the 3-D spectrum image at  $509 \pm 10$  eV, an image of the distribution of molybdenum within this area is obtained since the molybdenum M1 energy loss edge is located at 505 eV.



**Figure 7.6:** Surf3{Mo<sub>3</sub>Se<sub>3</sub>}. Magnification of figure 7.5. The green rectangle shows the area where Spectrum imaging was attempted. The spectrum image is inset on the left hand side. Each of the 64 pixels represents an EEL spectrum recorded in that area. The slice window was set at  $509 \pm 10$  eV (Mo M1 edge: 505 eV). Contrast within the spectrum image represents the presence of molybdenum.

Although there is some degree of “blurring” of the image which can be attributed to drift in the system during the acquisition of the spectra, especially in the upper right hand corner of the image, there are two clear bands of high contrast pixels running diagonally in the lower left hand side of the image (green arrows). These bands correspond well to the locations of the {Mo<sub>3</sub>Se<sub>3</sub>} strands in the HAADF image.

Figure 7.7 shows two spectra taken from the pixels labelled “0” and “1” in the spectrum image. By integrating the number of counts under the plot for the same energy range in both cases, it is apparent that there is a higher concentration of molybdenum present in the area represented by pixel “0” by a factor of  $\sim 1.4$ .

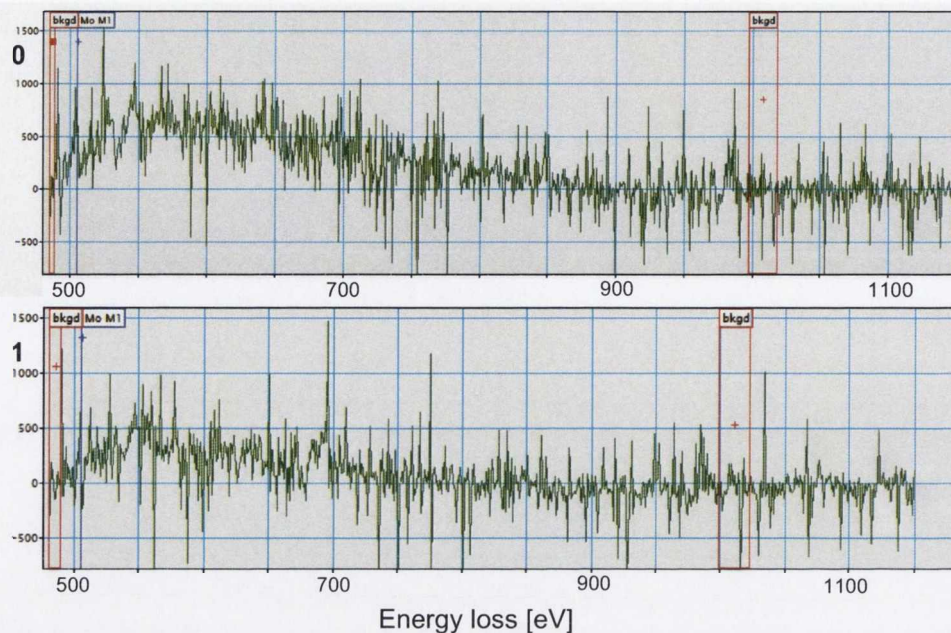


**Figure 7.7:** EELS spectra from the spectrum image shown in figure 7.6. Top: Spectrum obtained at site “0” in figure 7.6, bottom: spectrum obtained at site “1”

Figure 7.8 shows an EEL spectrum recorded over the area where the spectrum image was obtained. Both figures 7.8 (A) and (B) are the same spectrum, however two different elemental signals are examined, (A) shows the Carbon K edge and (B) shows the Molybdenum M3 edge. The signal at the carbon edge is rather large as expected given that the sample is supported by a carbon film. However, given the area where the spectrum was acquired, a contribution from the carbon of the organic ligands is expected.

The Mo M3 edge at an energy loss of 392 eV can be clearly seen in the inset of figure 7.8 (B). The inset shows a magnified view of the background subtracted signal seen on the x-axis of the main spectrum. From these spectra, in addition to the spectrum imaging, it can be inferred that both molybdenum and carbon are present in the sample.

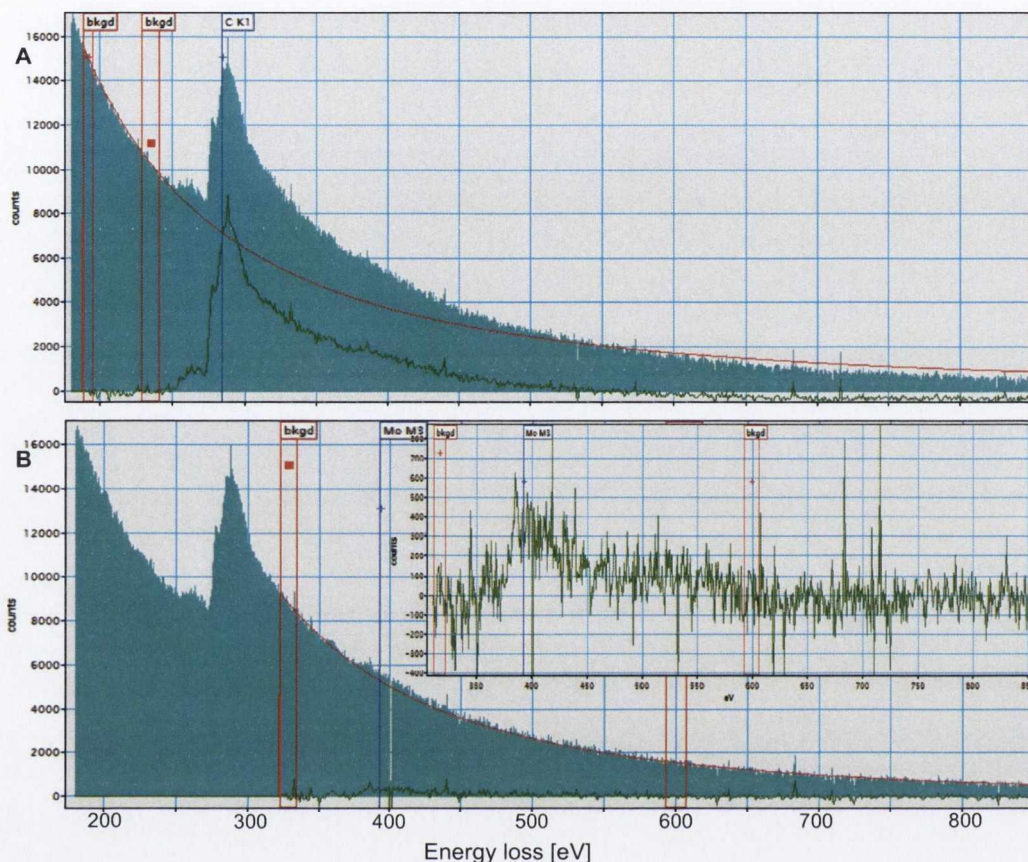


**Figure 7.8:** EEL spectrum of a Surf3 {Mo<sub>3</sub>Se<sub>3</sub>} network. (A) The green plot shows the background subtracted spectrum with the Carbon K edge clearly visible. (B) The same spectrum, but with the background subtraction performed after the onset of the carbon edge. In this case the Molybdenum M3 edge is visible. The inset on (B) is an enlarged plot of the x-axis in the main image after background subtraction.

### 7.3.1.a Dependence of parent LiMo<sub>3</sub>Se<sub>3</sub> solution concentration on Surf3 {Mo<sub>3</sub>Se<sub>3</sub>} network formation

To investigate whether the appearance of ribbons of Surf3 {Mo<sub>3</sub>Se<sub>3</sub>} is dependent on the size of the parent LiMo<sub>3</sub>Se<sub>3</sub> nanowire, two more samples were prepared, one from a 10<sup>-4</sup>M LiMo<sub>3</sub>Se<sub>3</sub> solution and one from a 10<sup>-5</sup>M LiMo<sub>3</sub>Se<sub>3</sub> solution. Images of these samples were compared with the images above which were obtained from a 10<sup>-3</sup>M solution. The samples were prepared as described previously (section 3.4) and were imaged using a JEOL 2100 TEM system at 200kV.

Figure 7.9 shows two images of Surf3{Mo<sub>3</sub>Se<sub>3</sub>} prepared from a 10<sup>-4</sup>M LiMo<sub>3</sub>Se<sub>3</sub> solution.

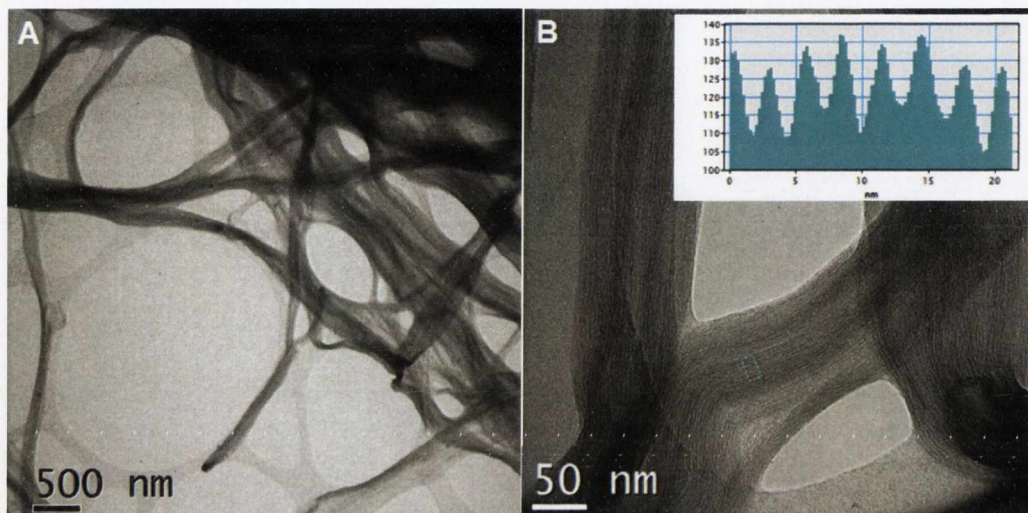


**Figure 7.9:** TEM image of Surf3{Mo<sub>3</sub>Se<sub>3</sub>} prepared from a 10<sup>-4</sup>M LiMo<sub>3</sub>Se<sub>3</sub> solution. Inset on B corresponds to the interwire spacing from the blue rectangle in B

These images, although lower in resolution than the STEM images above (figures 7.2 – 7.5), show that, superficially, there is no noticeable change in appearance of networks obtained from lower concentration parent solutions. Figure 7.9A shows a typical ion-exchanged network scenario of knotted and intertwined Surf3{Mo<sub>3</sub>Se<sub>3</sub>} ribbons. A magnified image of this area, figure 7.9B shows branching of these ribbons with interwire separations of ~2.84 nm, similar to the values obtained for networks formed from 10<sup>-3</sup>M LiMo<sub>3</sub>Se<sub>3</sub> parent solutions.

Figure 7.10 shows a standard TEM image of a Surf3{Mo<sub>3</sub>Se<sub>3</sub>} network obtained from a parent LiMo<sub>3</sub>Se<sub>3</sub> solution of concentration 10<sup>-5</sup>M. Again, in the low magnification case (figure 7.10A) knotted and overlapping Surf3{Mo<sub>3</sub>Se<sub>3</sub>} ribbons are noted and a magnified view of this area (figure 7.10B) shows an interwire separation for these ribbons of ~3.04 nm, which is slightly higher than the values

obtained for ion-exchanged ribbons from  $10^{-3}\text{M}$  and  $10^{-4}\text{M}$   $\text{LiMo}_3\text{Se}_3$  parent solutions.

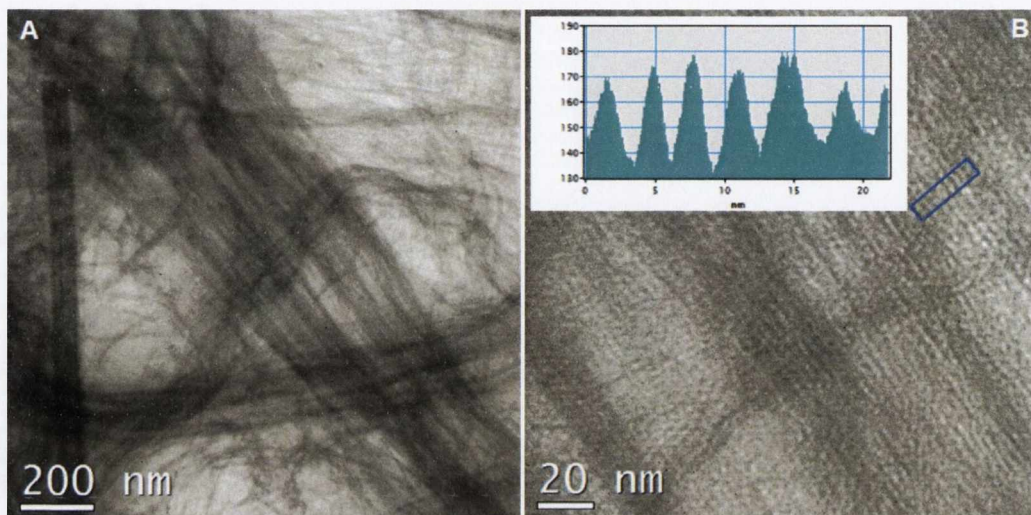


**Figure 7.10:** TEM image of Surf3{Mo<sub>3</sub>Se<sub>3</sub>} prepared from a  $10^{-5}\text{M}$  LiMo<sub>3</sub>Se<sub>3</sub> solution.

It is worth noting that, due to the manner of sample preparation, it is difficult to draw statistically reliable data from these images. This is because only a small fraction of the material deposited on a TEM grid is available to be imaged. During the wet preparation of these samples, the product (the ion-exchanged networks) precipitates from solution, typically as what can be described as a “seaweed” type material. A small amount of this product is transferred onto a TEM grid and vacuum dried. Typically, an area of  $\sim 0.05\text{ mm}^2$  of material is deposited on a grid, however only a few areas of the deposited mass are sufficiently electron transparent for TEM analysis. The bulk of the material is too thick, consisting of an entangled mass of ion-exchanged nanowire chains. For the case of the ion-exchanged networks formed from  $10^{-4}\text{M}$  and  $10^{-5}\text{M}$  LiMo<sub>3</sub>Se<sub>3</sub> concentrations, even less material was deposited on the TEM grids than normal. As such, the areas presented above are typically the best of perhaps three areas that were possible for imaging. While the images and

data obtained are representative of the bulk, the scarcity of available areas to image makes it difficult to draw conclusions about the effect of parent solution concentration on ribbon formation, however, judging from the areas imaged in this study, it appears that it is of little influence.

### 7.3.2 Characterisation of $X^+ \{Mo_3Se_3\}^-$ networks formed from $X =$ Surf 4, Surf 5 and Surf Thio

As noted in table 7.1 Surf 3 was not the only surfactant ligand to be used in this study. Surf 4 (similar to Surf 3, a long chain perfluorinated ligand), Surf 5 (with a voluminous adamantyl end group) and Surf Thio (a short chain amino thiol ligand) were also used to produce ion-exchanged networks.



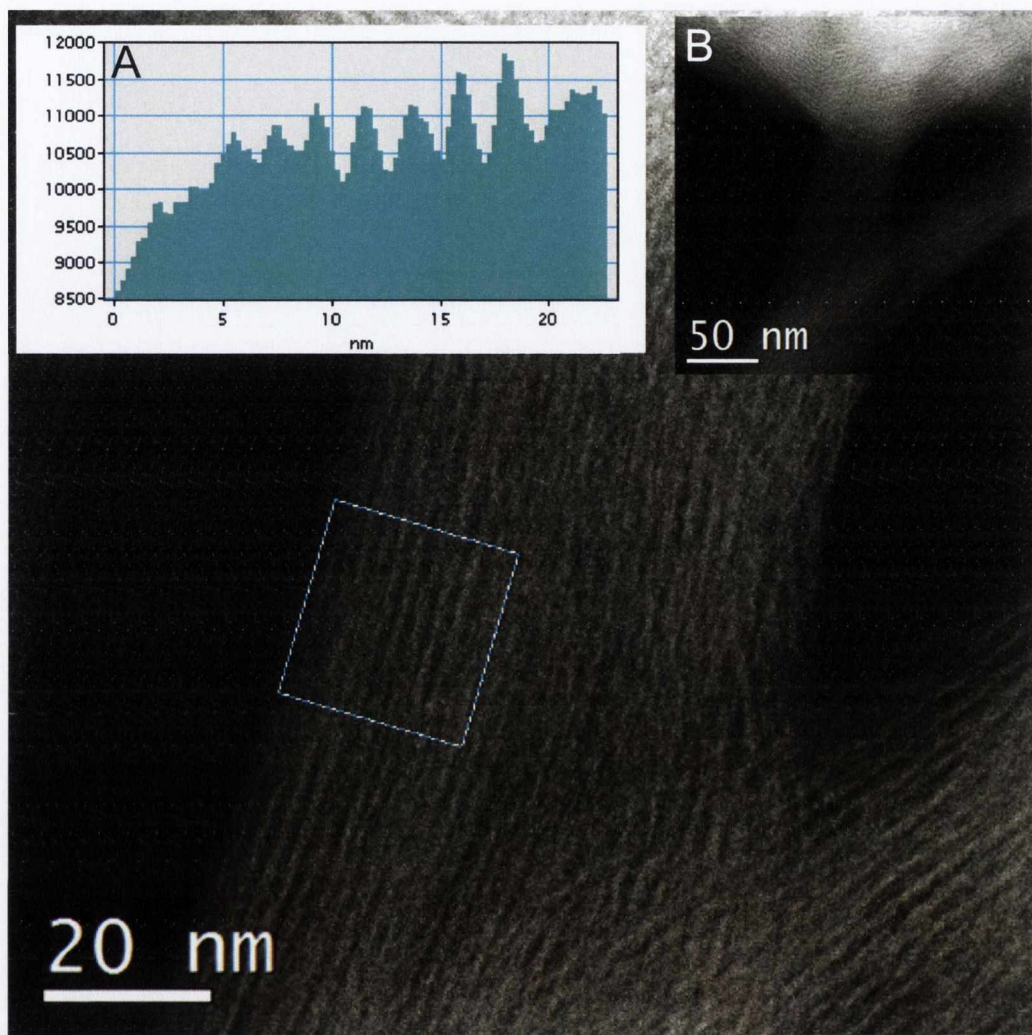


**Figure 7.11:** STEM image of Surf4{Mo<sub>3</sub>Se<sub>3</sub>}. Inset A shows a cross section of the area in the blue rectangle. Inset B shows a less magnified image of this area

Figure 7.11 shows an image of Surf4{Mo<sub>3</sub>Se<sub>3</sub>}, taken on a commercial JEOL 3000F instrument operating in STEM mode with a HAADF detector. Inset A shows a colour intensity cross section of the area marked with the blue rectangle in the main image. As with Surf3{Mo<sub>3</sub>Se<sub>3</sub>}, the actual average interwire separation was calculated from a larger number of measurements than those shown and was found to be  $2.85 \pm 0.07$  nm. Inset B shows a less magnified view of the image in figure 7.11. Similar to Surf3Mo<sub>3</sub>Se<sub>3</sub>, the formation of two-dimensional ribbons of the ion-exchanged networks is observed. These similarities are not surprising given the similarities between the two ligands. In this instance, it appears that the ribbons are

extending from a larger entangled mass of ion-exchanged network. This dense mass is to be expected for all samples due to the fact that the majority of the material on the TEM grid was far too thick to be electron transparent, only thinner areas at the edges of the sample were available for imaging.

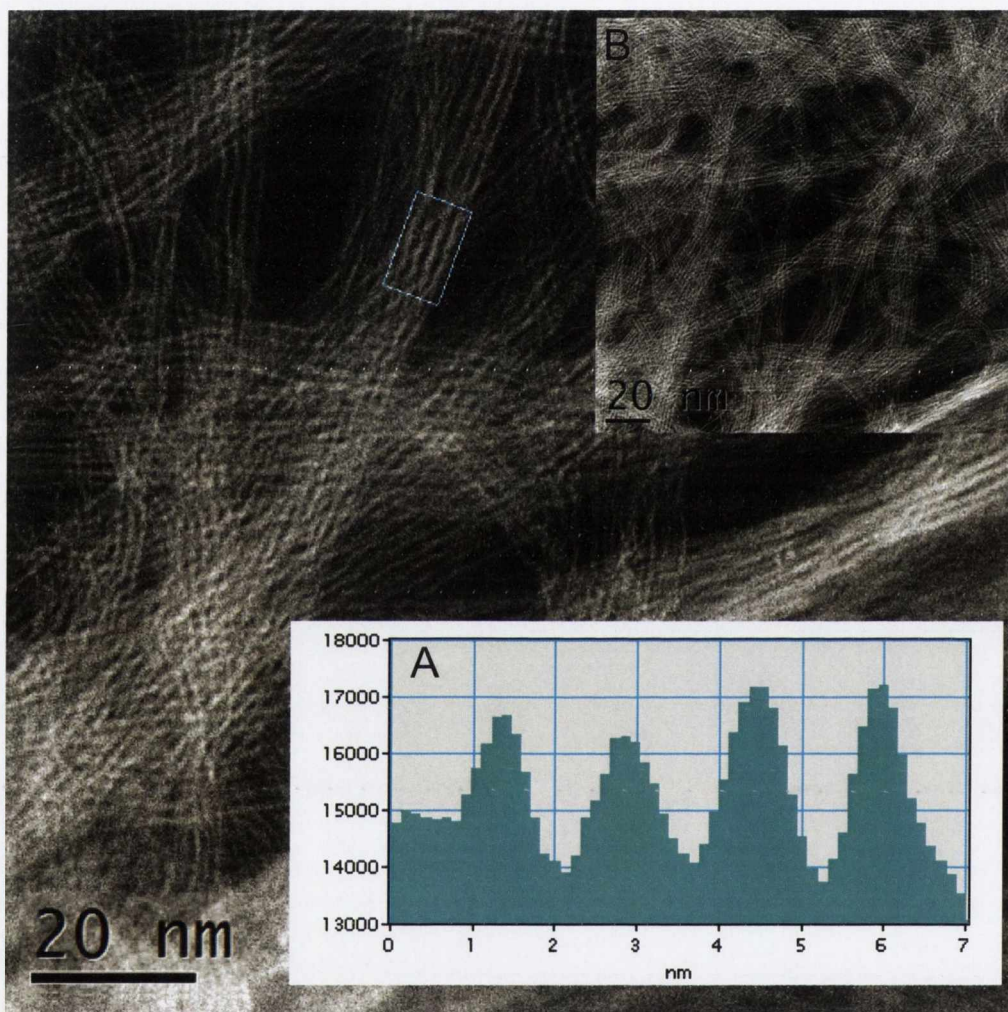


**Figure 7.12:** STEM image of Surf5{Mo<sub>3</sub>Se<sub>3</sub>}. Inset A shows a cross section of the area in the blue rectangle. Inset B shows a less magnified image of this area

Figures 7.12 and 7.13 are HAADF-STEM images of Surf5{Mo<sub>3</sub>Se<sub>3</sub>} and SurfThio{Mo<sub>3</sub>Se<sub>3</sub>} taken on a commercial JEOL3000F instrument. In both these images the ribbon like structure is clearly visible and all ribbons appear fairly uniform in width. The cross section insets A show the interwire spacing for the area in the images marked with the blue rectangle. The interwire spacings (averaged over

a large number of measurements on a series of images of these materials) were found to be  $1.63 \pm 0.02$  nm for Surf5 and  $1.16 \pm 0.05$  nm for SurfThio. Insets B are lower magnification images of the areas of interest showing many ribbon-like structures present in the sample.

Surf5 $\{\text{Mo}_3\text{Se}_3\}$  (figure 7.12) appears to give ribbons only a few chains in width. This may be because the electron transparent part of the sample consists of ion-exchanged network that was formed from smaller diameter  $\text{LiMo}_3\text{Se}_3$  bundles. These ribbons consist of closely packed  $\{\text{Mo}_3\text{Se}_3\}_\infty$  chains as is to be expected given the short length of the ligand used compared to Surf 3 or Surf 4.

Networks of Surf Thio $\{\text{Mo}_3\text{Se}_3\}$  (figure 7.13) show ribbon formation similar to that of Surf 3 and Surf 4 with long dense ribbons visible. Due to the very short ligand used this network has the smallest interwire spacing.

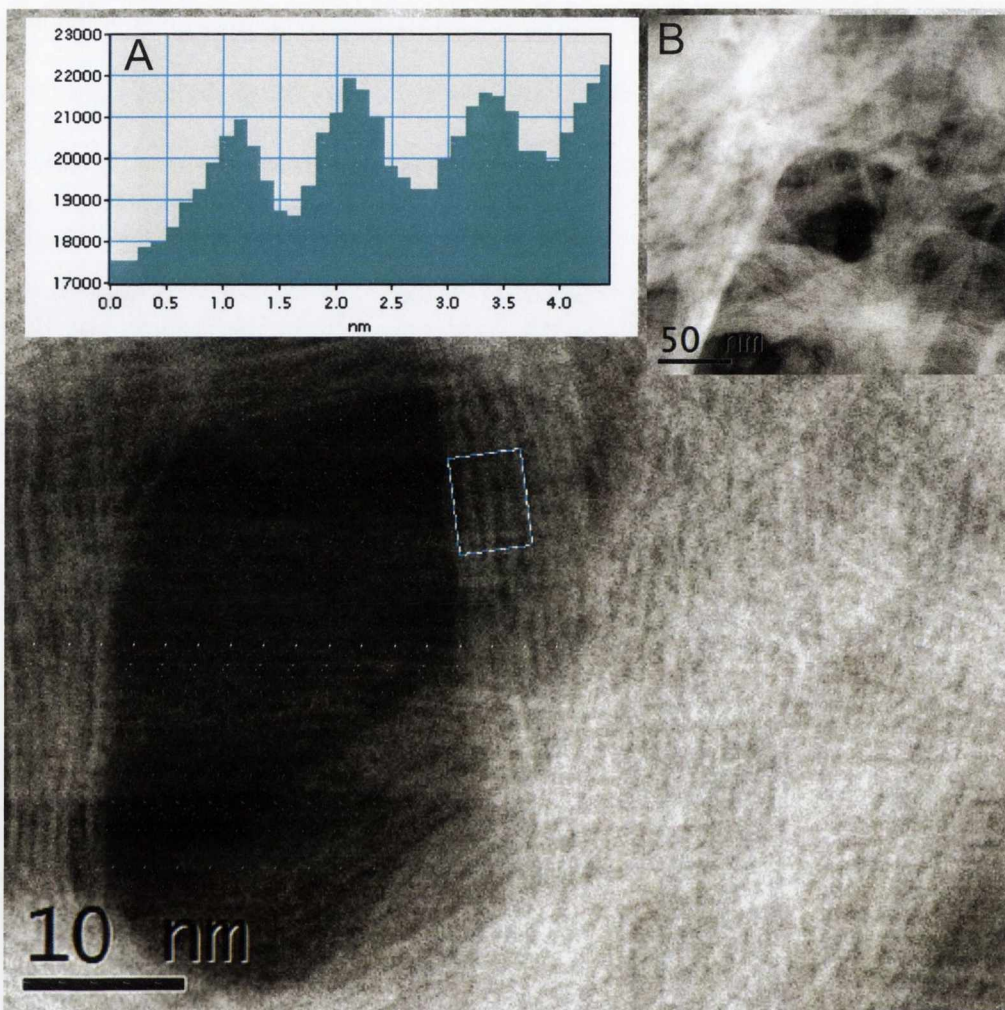


**Figure 7.13:** STEM image of SurfThio{Mo<sub>3</sub>Se<sub>3</sub>}. Inset A shows a cross section of the area in the blue rectangle. Inset B shows a less magnified image of this area

## 7.4 Conclusions

TEM, STEM and EELS studies have been presented for ion-exchanged networks of the form  $X^+\{Mo_3Se_3^-\}_\infty$  where X is an organic ligand (see table 7.1). Images of these samples show the formation of long flat ribbons of ion-exchanged material which cross and knot with each other to form network. Junctions of these networks are not continuous like those of bare LiMo<sub>3</sub>Se<sub>3</sub> (section 4.3.2) but consist of entwined or overlapping ribbon strands as evidenced by the increase in contrast of the HAADF images of these junctions.

From the images obtained it becomes clear that the interwire separation of these ion-exchanged networks is dependent on the surfactant ligand used. In order of increasing length, the surfactant ligands; Thio; 5; 3; 4 cause a corresponding increase in the interwire spacing of the networks they form. (Table 7.2) This observed interwire spacing scales well with the estimated physical length of the surfactants, indicating a good degree of interdigitation for Surfs 3 and 4.

| Ligand    | Mean interwire spacing [nm] | Standard deviation ( $\sigma$ ) | Standard error ( $\sigma/\sqrt{N}$ ) | Estimated physical length [nm] |
|-----------|-----------------------------|---------------------------------|--------------------------------------|--------------------------------|
| Surf 3    | 2.71                        | 0.28                            | 0.04                                 | 1.75                           |
| Surf 4    | 2.85                        | 0.45                            | 0.07                                 | 1.86                           |
| Surf 5    | 1.63                        | 0.15                            | 0.02                                 | 0.77                           |
| Surf Thio | 1.16                        | 0.30                            | 0.05                                 | 0.49                           |

Table 7.2 Mean interwire spacings

EELS data of samples of Surf3  $\{\text{Mo}_3\text{Se}_3\}$  show the presence of carbon and fluorine in the areas between the  $\{\text{Mo}_3\text{Se}_3\}_\infty$  strands and the spectrum imaging shows bands of light and dark areas which correlate well to the location of the  $\{\text{Mo}_3\text{Se}_3\}_\infty$  strands in these ribbons.

Investigation of the effect of parent  $\text{LiMo}_3\text{Se}_3$  solution concentration on the geometry of ribbons of Surf3  $\{\text{Mo}_3\text{Se}_3\}$  appeared to make no appreciable difference in the case of  $10^{-3}\text{M}$ ,  $10^{-4}\text{M}$  and  $10^{-5}\text{M}$   $\text{LiMo}_3\text{Se}_3$  solutions.

## 7.5 References

- [1] A. Heidelberg, H. Bloess, J. W. Schultze, C. J. Booth, E. T. Samulski, J. J. Boland, *Zeitschrift Fur Physikalische Chemie-International Journal of Research in Physical Chemistry & Chemical Physics* **2003**, 217, 573.
- [2] B. Messer, J. H. Song, M. Huang, Y. Y. Wu, F. Kim, P. D. Yang, *Advanced Materials* **2000**, 12, 1526.
- [3] C. F. J. Faul, M. Antonietti, *Advanced Materials* **2003**, 15, 673.
- [4] J. H. Song, B. Messer, Y. Y. Wu, H. Kind, P. D. Yang, *Journal of the American Chemical Society* **2001**, 123, 9714.
- [5] B. Fultz, J. M. Howe, *Transmission Electron Microscopy and Diffractometry of Materials*, Springer, **2008**.
- [6] J. M. Tarascon, G. W. Hull, F. J. DiSalvo, *Materials Research Bulletin* **1984**, 19, 915.
- [7] M. D. Hornbostel, S. Hillyard, J. Silcox, F. J. Disalvo, *Nanotechnology* **1995**, 6, 87.
- [8] R. Brydson, *Electron Energy Loss Spectroscopy*, BIOS Scientific Publishers **2001**.

## Chapter 8

# Electrical properties of $\text{LiMo}_3\text{Se}_3$ bundles and ion-exchanged $\text{X}^+\{\text{Mo}_3\text{Se}_3\}^-$ networks

### 8.1 Introduction

In this chapter, the electrical properties of bare  $\text{LiMo}_3\text{Se}_3$  nanowires and ion-exchanged  $\text{X}^+\{\text{Mo}_3\text{Se}_3\}^-$  networks are measured and discussed. As mentioned in chapter 7, these ion-exchanged  $\text{X}^+\{\text{Mo}_3\text{Se}_3\}^-$  materials were prepared with the intention of creating conducting  $\{\text{Mo}_3\text{Se}_3\}$  wires that are resistant to oxidation, unlike  $\text{LiMo}_3\text{Se}_3$  which degrades in ambient conditions. The effect of the surfactants on the  $\{\text{Mo}_3\text{Se}_3\}$  corrosion stability is discussed in the work of Heidelberg et al. [1, 2]

For the studies described herein, electrical measurements of  $\text{LiMo}_3\text{Se}_3$  nanowires were performed by depositing  $\text{LiMo}_3\text{Se}_3$  solutions on  $\text{SiO}_2$  substrates. Electrical contact between the nanowire and prepatterned Au leads was made by electron beam induced deposition of Pt from an organometallic precursor. Measurements were carried out in ambient conditions and in vacuum at temperatures varying from 7 K to room temperature.

Ion-exchanged  $X^+\{Mo_3Se_3\}^-$  materials were deposited on  $SiO_2$  substrates with Au lines on the surface and electrical measurements were performed in vacuum at temperatures from 7 K to room temperature.

## 8.2 Characterisation

### 8.2.1 Electrical properties of $LiMo_3Se_3$ bundles in air

$LiMo_3Se_3$  bundles were spun cast from solution onto pre-patterned gold electrodes on  $SiO_2$  substrates in inert atmosphere. These substrates were pre-patterned with 8 Au lines tapering from  $1mm^2$  pads at the substrate edge to  $2\mu m$  wide fingers which surround a blank  $SiO_2$  “playground”,  $60\mu m$  to a side (figure 8.1B). The excess solvent was removed by pumping the sample in the glovebox antechamber. This sample was then transferred to a dual beam SEM/FIB system with an organometallic Pt gas source,  $(C_5H_5)Pt(CH_3)_3$ , for electron beam induced deposition (EBID) of metal lines to make electrical contact to the nanowire bundle.[3]



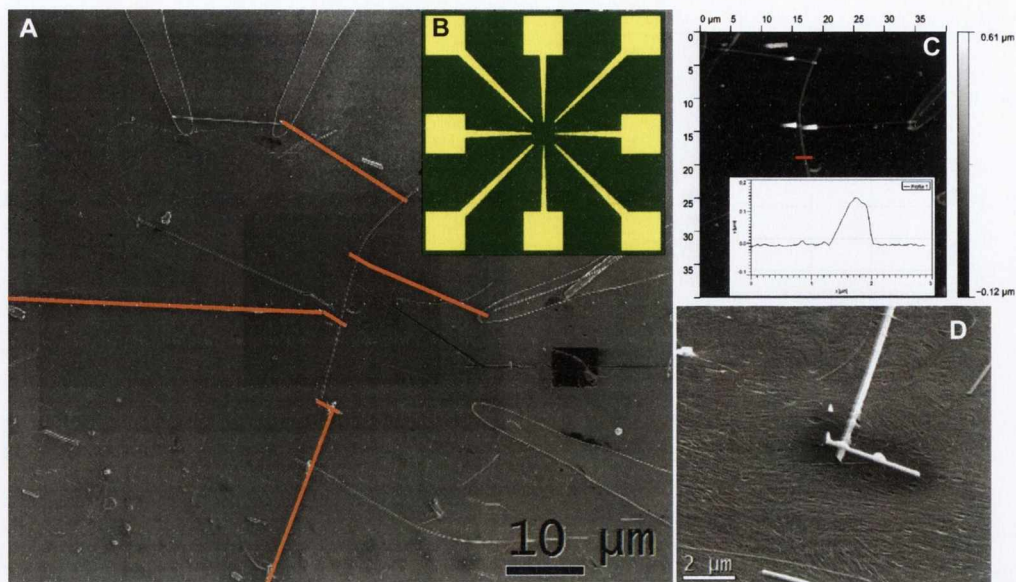


**Figure 8.1:** *A:  $\text{LiMo}_3\text{Se}_3$  bundle for electrical measurements. Four EBID Pt contacts (orange) connect the nanowire to prepatterned gold lines. B: Schematic of prepatterned gold lines on  $\text{SiO}_2$  substrate. C: AFM image of bundle with height profile corresponding to the red line (height 151nm). D: Close up of beam deposited Pt line crossing the nanowire (the nanowire is running top to bottom).*

Figure 8.1 shows a SEM image of the bundle following EBID of Pt lines which connect the nanowire bundle to the pre-patterned Au electrodes. Once the sample was placed in the SEM/FIB system, a suitable  $\text{LiMo}_3\text{Se}_3$  nanowire was identified and Pt lines were deposited connecting the nanowire to the pre-patterned Au lines via beam induced deposition of Pt. Inset C shows an AFM image with a height profile which gives the height of the nanowire to be 151nm. The AFM image was taken after all electrical measurements. Inset D shows a Pt line crossing the  $\text{LiMo}_3\text{Se}_3$  nanowire. This sample was used for the resistance vs. temperature measurements in section 8.2.2.

Another nanowire prepared in this way (height: 110nm, centre electrode separation:  $1.73\mu\text{m}$ ) was used to investigate the effect of air exposure upon the electrical

characteristics of a  $\text{LiMo}_3\text{Se}_3$  nanowire over time as this material is susceptible to oxidation upon exposure to air.[4, 5]

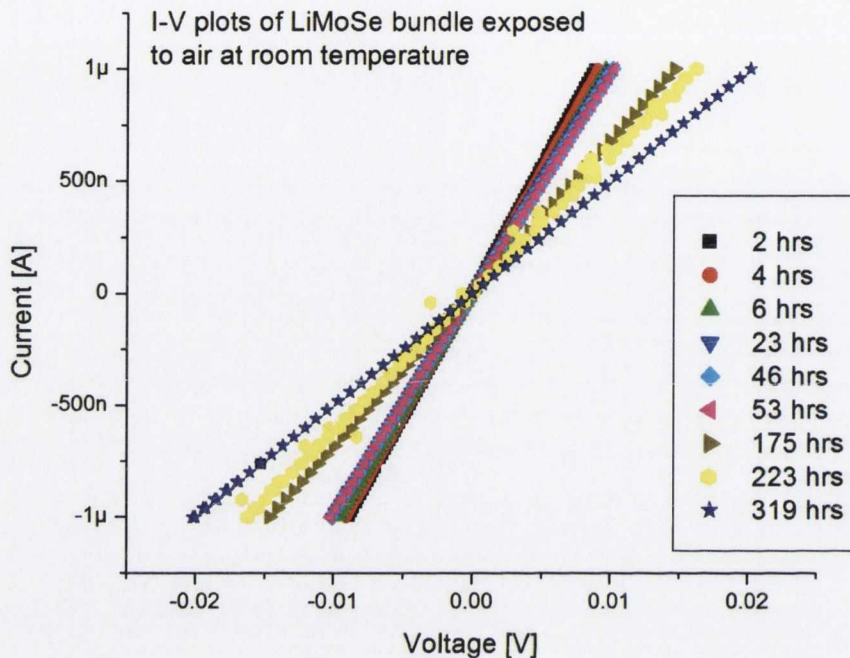


**Figure 8.2:** Successive I-V plots for a 110 nm diameter  $\text{LiMo}_3\text{Se}_3$  bundle, obtained as the specimen was exposed to air

Once the electrical connections had been made, current-voltage (I-V) plots were obtained using a Karl Suss PM8 probe station (tungsten probes) and a Keithley 2400 source measure unit (SMU). These measurements were made using a four point probe method, i.e. for each a current was sourced through the outer two probes and the associated voltage drop across the centre two electrodes was measured. Four point probe measurements were used because they eliminate contact resistance inaccuracies. The current was swept from  $-1\mu\text{A}$  to  $1\mu\text{A}$ , and measurements were recorded over 319 hours. The current range was chosen to minimize the risk of destroying the wire while still giving a good signal to noise ratio. The results, figure 8.2, show a marked increase in resistance with increasing time (i.e. decreasing

slope). Also, the I-V plots remain linear throughout, indicating metallic behaviour along the nanowire axis over the bias range investigated.

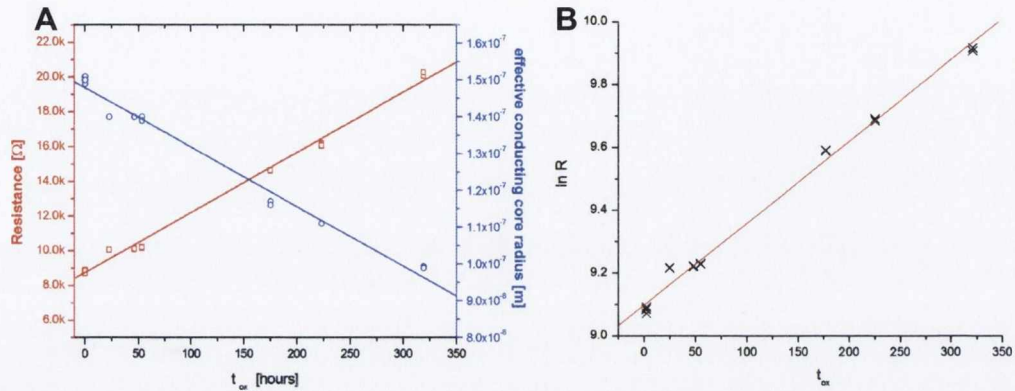


**Figure 8.3:** *A: Resistance vs. time (red) and effective conducting core radius vs. time (blue) for  $\text{LiMo}_3\text{Se}_3$  bundle exposed to ambient. B:  $\ln R$  vs.  $t_{ox}$  for nanowire bundle exposed to ambient*

Figure 8.3A shows the resistance of the nanowire plotted against time for each measurement taken (red plot and axis) and the size of the effective conducting core radius vs. time (blue plot and axis) based on the assumption that oxidation starts at the surface and progresses inwards. Because the nanowire had already oxidised for  $\sim 2$  hours prior to the first measurement, the resistance of the pristine wire can be found from the value of the plot intercept with the y axis at  $t_{ox} = 0$ . This gives an estimate of the intrinsic resistivity of the materials to be  $4.76 \cdot 10^{-5} \Omega\text{m}$ , in excellent agreement with Golden et al.[6] who showed similar values ( $5 \cdot 10^{-5} \Omega\text{m}$ ) for free standing films of  $\text{LiMo}_3\text{Se}_3$ . As the nanowire bundle oxidises, less and less material is available for conduction. The size of the effective conducting core of the wire is estimated using the resistivity of the pristine nanowire and calculating the radius of a nanowire necessary to account for the measured resistance. This is shown in the blue plot of figure 8.3A.

Assuming the nanowire oxidation is a first order reaction, the oxidation half life can be calculated from a plot of  $\ln R$  vs  $t_{ox}$  as shown in figure 8.3B. The half life can be estimated using the equation;

$$t_{1/2} = \frac{\ln 2}{k} \quad (8.1)$$

where the equation of the line in figure 8.3B is

$$\ln R = 0.00261t_{ox} + 9.09753 \quad (8.2)$$

This yields a half life value of 265.6 hours, i.e. the resistance doubles every 265.6 hours.

### 8.2.2 Resistance as a function of temperature of $\text{LiMo}_3\text{Se}_3$ bundle under vacuum

In addition to measurements conducted under ambient conditions, the conductivity of  $\text{LiMo}_3\text{Se}_3$  bundles was also investigated under variable temperatures. Four point probe samples (similar to the section 8.2.1) were prepared on  $\text{SiO}_2$  substrates and affixed to the cooling block of a helium closed cycle cryostat (ARS DE-202NF) using Apiezon N grease. The system was then pumped to  $\sim 10^{-6}$  mbar and the temperature cycled from 300K – 7K. Resistance vs. temperature measurements and I-V measurements at varying temperatures were then carried out using a Keithley 2400.

Figure 8.4 shows the natural logarithm of the conductivity vs. the inverse temperature obtained from a 4 point measurement of a  $\text{LiMo}_3\text{Se}_3$  nanowire (height

151 nm, centre electrode spacing  $8\mu\text{m}$ ). The inset of this figure shows the recorded resistance vs. temperature plot. This is the same nanowire shown in figure 8.1.

The nanowire's resistance rises gradually from  $\sim 4\text{ k}\Omega$  at room temperature to  $\sim 11\text{ k}\Omega$  at 17 K (figure 8.4 inset) after which it dramatically increases to a final resistance of  $\sim 17\text{ k}\Omega$  at 7 K. The room temperature resistance yields a resistivity of  $9.1 \cdot 10^{-6}\ \Omega\text{m}$ . In the work of Venkataraman, et al.[7], macroscopic samples (diameter  $> 1\mu\text{m}$ ) were reported to display metallic behaviour with decreasing temperature, i.e., resistance decreased at lower temperatures. They reported two probe measurements of smaller wires (diameter 1-15nm) which behave similarly to those presented here. In their case, the sharp increase in resistance at low temperatures was attributed to Coulomb blockade and indicates the presence of tunnel junctions, most likely due to defects within the wire. A Pierels transition at low temperatures can be ruled out due to the fact that scanning tunneling spectroscopy (STS) measurements of these wires at low temperature show no evidence for the formation of a band gap. [1, 8]

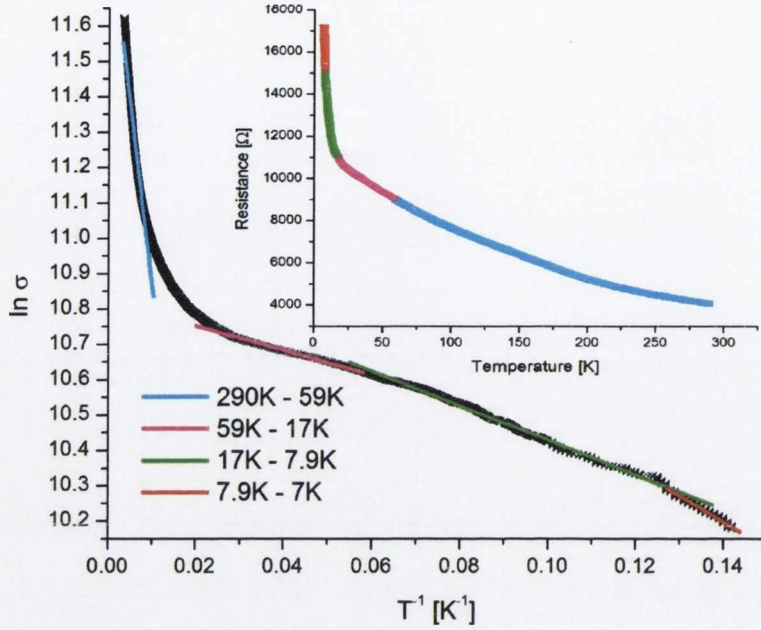


**Figure 8.4:** Natural logarithm of the conductivity vs. the inverse temperature for a  $\text{LiMo}_3\text{Se}_3$  bundle under vacuum. The colours of the linear plots correspond to the coloured regions of the inset which is the Resistance vs. Temperature plot for this nanowire bundle

The temperature dependence of the conductivity is more clearly seen in the plot of  $\ln \sigma$  vs.  $T^{-1}$  (figure 8.4 main image). Using equation (8.3) the energy barrier associated with activated transport for each of the four straight line regions can be determined and are presented in table 8.1.

$$\sigma = \sigma_0 e^{\frac{-E}{2k_B T}} \quad (8.3)$$

$$\ln \sigma = \frac{-E}{2k_B} T^{-1} + \ln \sigma_0 \quad (8.4)$$

where  $\sigma$  = conductivity,  $E$  = energy,  $T$  = temperature,  $k_B$  = Boltzmann constant

| Temperature | Energy                  |
|-------------|-------------------------|
| 290K-59K    | $1.75 \cdot 10^{-2}$ eV |
| 59K-17K     | $5.98 \cdot 10^{-4}$ eV |
| 17K-7.9K    | $8.39 \cdot 10^{-4}$ eV |
| 7.9K-7K     | $1.27 \cdot 10^{-3}$ eV |

**Table 8.1:** temperature ranges and calculated activation energy for  $\text{LiMo}_3\text{Se}_3$  nanowire

Current-voltage (I-V) measurements were recorded at a variety of temperatures during the cooling cycle, figure 8.5. These I-V plots remain linear for all temperatures over the range studied indicating the nanowire bundle has ohmic behaviour and no bandgap is noted.

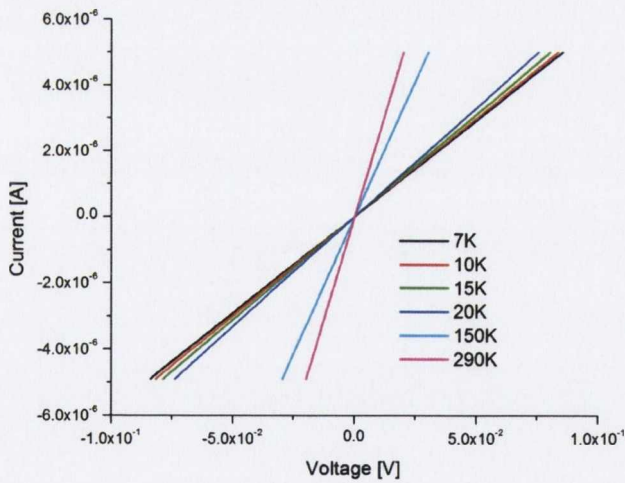


**Figure 8.5:** I-V plots for  $\text{LiMo}_3\text{Se}_3$  bundle under vacuum at different temperatures

This behaviour seen here; a gradual increase in resistance with decreasing temperature, a dramatic increase in resistance at low temperatures (<17 K) and linear I-V characteristics over the whole temperature range is similar to the work of RueB,

et al.[9] Their results showed that P-doped Si nanowires behave in a similar fashion over a temperature range 35 – 1.3 K and attribute the drastic increase in resistance at sub 4 K temperatures to a 1-dimensional Variable Range Hopping (VRH) mechanism.[10]

$$\sigma = \sigma_0 \exp(T_0 / T)^{\frac{1}{d+1}} \quad (8.5)$$

Where  $\sigma$  is the conductivity,  $T$  is the temperature and  $d$  describes the dimensionality of the conductor.

Using this model, the data in figure 8.4 ( $\ln \sigma$  vs  $T^{-1}$ ) was replotted as  $\ln \sigma$  vs  $T^{-1/2}$  (1D),  $\ln \sigma$  vs  $T^{-1/3}$  (2D) and  $\ln \sigma$  vs  $T^{-1/4}$  (3D), for the ranges that give straight lines in the  $\ln \sigma$  vs  $T^{-1}$  plot. The findings are summarised in figure 8.6. The description in the legend of each graph is the value of the x-axis for that colour plot. The  $R^2$  values of the linear fits for each data set are displayed on the graph. In the temperature ranges 290 – 150 K and 40 – 20K the best fit was found to be  $T^{-1/4}$  (3D). The 14 – 8 K region also fits best to  $T^{-1/4}$  but the  $R^2$  values indicate it is very close to  $T^{-1/2}$ . Oddly for the 7.8 – 7 K region  $T^{-1}$  fits best, but there is very little difference between the  $R^2$  values in this temperature range (the  $R^2$  values in the work of RueB, et al. also showed little difference between each fit for a given temperature range). It seems the trend would indicate that at higher temperatures the conduction occurs by a 3D VRH mechanism which (at  $< 17$  K temperatures) switches to a 1D VRH system, most likely due to electron localization at low temperatures.



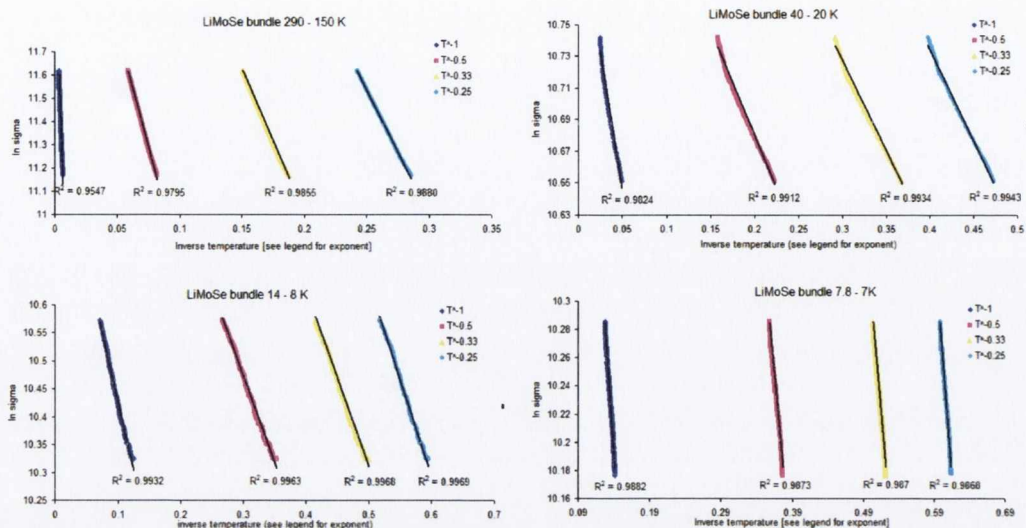


**Figure 8.6:**  $\ln \sigma$  vs  $T^{-1}$  (navy),  $T^{-1/2}$  (magenta),  $T^{-1/3}$  (yellow),  $T^{-1/4}$  (light blue) for a LiMoSe bundle. The temperature ranges are displayed at the top of each plot and the  $R^2$  values for each linear fit is displayed beside the trendline

### 8.2.3 Ion-exchanged $X^+ \{Mo_3Se_3\}^-$ networks

In addition to regular  $LiMo_3Se_3$  nanowires, the electrical conductivity of ion-exchanged  $X^+ \{Mo_3Se_3\}^-$  nanowire networks was also investigated. Previous studies (Heidelberg, et al.[1]) show that under ambient conditions these nanowire networks are much less susceptible to oxidation and that conduction occurs via a percolation mechanism. In this case the conduction is determined by the interwire separation and occurs by a hopping mechanism between the  $\{Mo_3Se_3\}$  chains, figure 8.7.

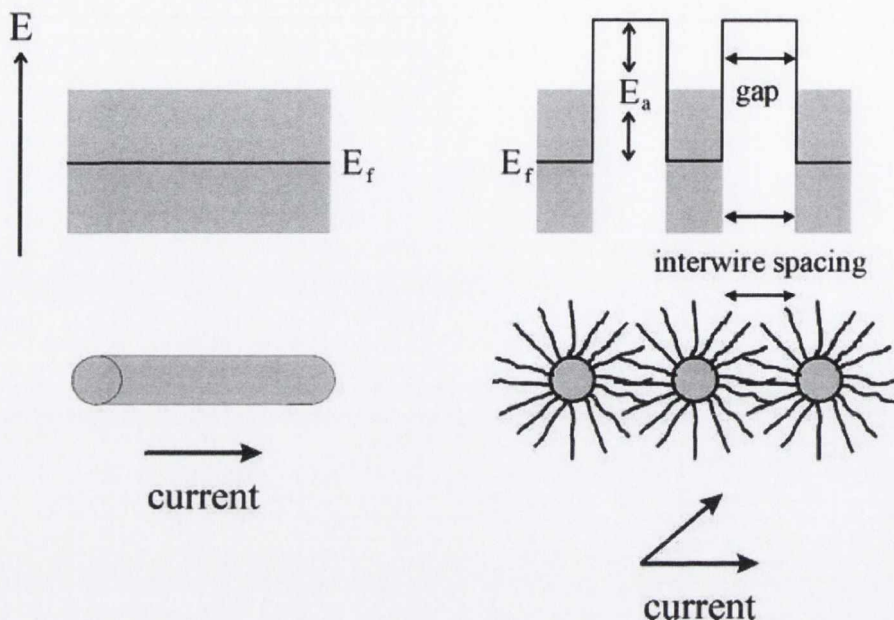


**Figure 8.7:**  $\text{LiMo}_3\text{Se}_3$  nanowires conduct along the wire axis. In the case of ion-exchanged networks (right) the conduction is also influenced by the increased interwire separation due to the positively charged ligands replacing the Li counter ion [1]

Ion-exchanged  $\text{X}^+ \{\text{Mo}_3\text{Se}_3\}^-$  samples were prepared as outlined in section 3.4. The precipitates formed were placed on  $\text{SiO}_2$  substrates with prepatterned Au electrodes (spacing  $\sim 2\text{mm}$ ). These samples were then pumped overnight to remove excess solvent. Figure 8.8 shows a schematic of the configuration used. Measurements were performed using a helium closed cycle cryostat (ARS DE-202NF) and a Keithley 2400 source-measure unit (SMU) as per the temperature dependent conductivity measurement for the  $\text{LiMo}_3\text{Se}_3$  nanowire.

| Name      | Ligand   | Structure   |
|-----------|--|---|
| Surf 3    | 1-H, 1-H, 2-H, 2-H – Perfluorodecyl-pyridiniumchloride               |   |
| Surf 4    | N', N'- dimethyl – N – (perfluorooctansulfonyl)-piperaziniumchloride |   |
| Surf 5    | 1-(1-Adamantyl)-pyridiniumbromide                                    |   |
| Surf 6    | 1-H, 1-H, 2-H, 2-H, Perfluorooctyl-pyridiniumchloride                |   |
| Surf Thio | 2-Aminoethanthiol Hydrochloride                                      | $\text{H}_2\text{N}-\text{CH}_2-\text{CH}_2-\text{SH} \cdot \text{HCl}$ |

**Table 8.2:** Ligands used to form  $X^+ \{ \text{Mo}_3\text{Se}_3 \}^-$  networks

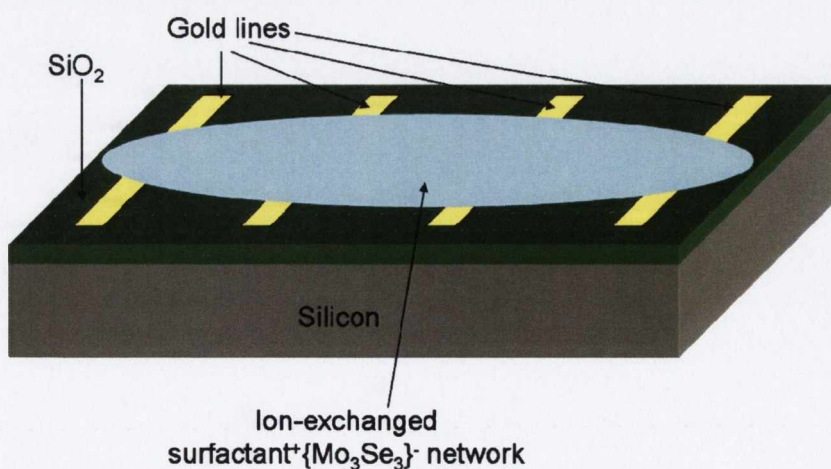


**Figure 8.8:** Schematic of ion-exchanged samples used for resistance vs. temperature measurements

The surfactant ion-exchanged networks conduct via a percolation mechanism.[1, 2] In the case of a macroscopic sample such as investigated here, the constituent  $\{\text{Mo}_3\text{Se}_3\}$  wires are not infinitely long, therefore transport between the wires must take place, figure 8.7. The surfactant ligands are a barrier to interwire transport as they increase the interwire separation and are overcome via a hopping mechanism. The energy barrier can be calculated similarly to the temperature dependence of the pristine  $\text{LiMo}_3\text{Se}_3$  nanowire in section 8.2.2.

$$\ln \sigma = \frac{-E}{2k_B} T^{-1} + \ln \sigma_0 \quad (8.4)$$

A plot of the natural logarithm of the conductivity vs. the inverse temperature for Surf3  $\{\text{Mo}_3\text{Se}_3\}$  is shown in figure 8.9. The inset shows the recorded resistance vs. temperature plot. The resistance increases with decreasing temperature, indicative of thermally activated conduction. In the case of Surf3  $\{\text{Mo}_3\text{Se}_3\}$ , the resistance rises from  $6.4\Omega$  to  $8\Omega$  in the temperature range from 300K to 20K with a noticeable peak at 193K. At temperatures lower than 20K, there is a sharp increase to  $15.4\Omega$  at 7K. Plotting this data as  $\ln \sigma$  vs  $T^{-1}$  there are four clear straight line regions<sup>4</sup>, 300K – 71.9K, 71.9K – 15.3K, 15.3K – 7.9K and 7.9K -7K.

---

<sup>4</sup> It is important to note that the resistivity and conductivity values presented for the ion-exchanged nanowire samples are rough estimates only. It is impossible to measure the thickness of the sample due to the “sea-weed” nature of the ion-exchanged materials. When calculating the resistivities for all used surfactants an estimate of 2 mm is taken for the centre electrode spacing and an estimate of  $5 \times 10^{-7} \text{ m}^2$  is taken for the cross sectional area (2mm x .25mm). Thus the resistivity values are estimates but the energy values obtained from the slopes of  $\ln \sigma$  vs  $T^{-1}$  are accurate as the slope depends on the measured resistance, the resistivity merely scales the plot up or down along the y-axis.

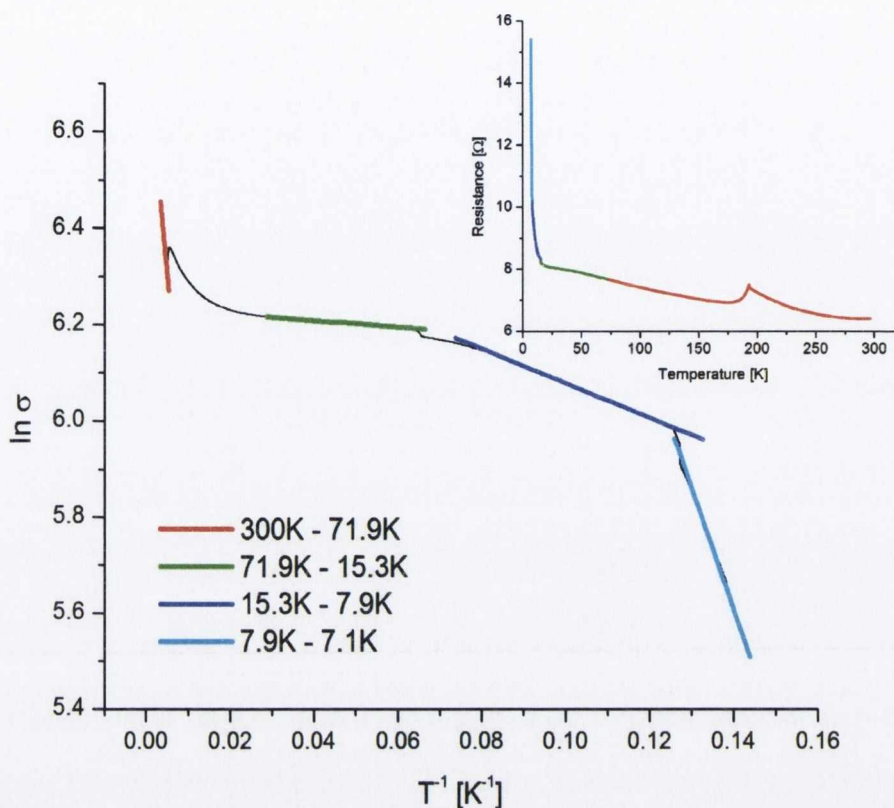


**Figure 8.9:**  $\ln \sigma$  vs  $T^{-1}$  for  $\text{surf3}\{\text{Mo}_3\text{Se}_3\}$  (under vacuum). The colours of the linear plots correspond to the coloured regions of the inset which shows the resistance vs temperature plot.

Similar behaviour is noted for  $\text{Surf4}\{\text{Mo}_3\text{Se}_3\}$ ,  $\text{Surf5}\{\text{Mo}_3\text{Se}_3\}$  and  $\text{Surf6}\{\text{Mo}_3\text{Se}_3\}$  (figure 8.10A, B and C below). In the case of  $\text{SurfThio}\{\text{Mo}_3\text{Se}_3\}$ , (figure 8.10D) the sample displays decreasing resistance with decreasing temperature but at  $\sim 85\text{K}$  the resistance begins to increase. It is worth mentioning that it is quite difficult to get the  $\text{SurfThio}\{\text{Mo}_3\text{Se}_3\}$  sample to adhere to the substrate. In order to prevent the sample from peeling off, a blank piece of  $\text{SiO}_2$  was placed (oxide side down) on top of the sample and sealed in place using Apiezon cryocon N grease (which has a resistivity of  $2 \cdot 10^{16} \Omega\text{m}$  [11]). Given the behaviour at  $< 85\text{K}$  temperature is consistent with the other samples measured, the data is presented with the other samples for comparison. The barrier energies for all  $X^+\{\text{Mo}_3\text{Se}_3^-\}$  systems are calculated and

presented in table 8.3. A representative  $\ln \sigma$  vs.  $T^{-1}$  plot explaining the terms used in table 8.3 is shown in figure 8.11.

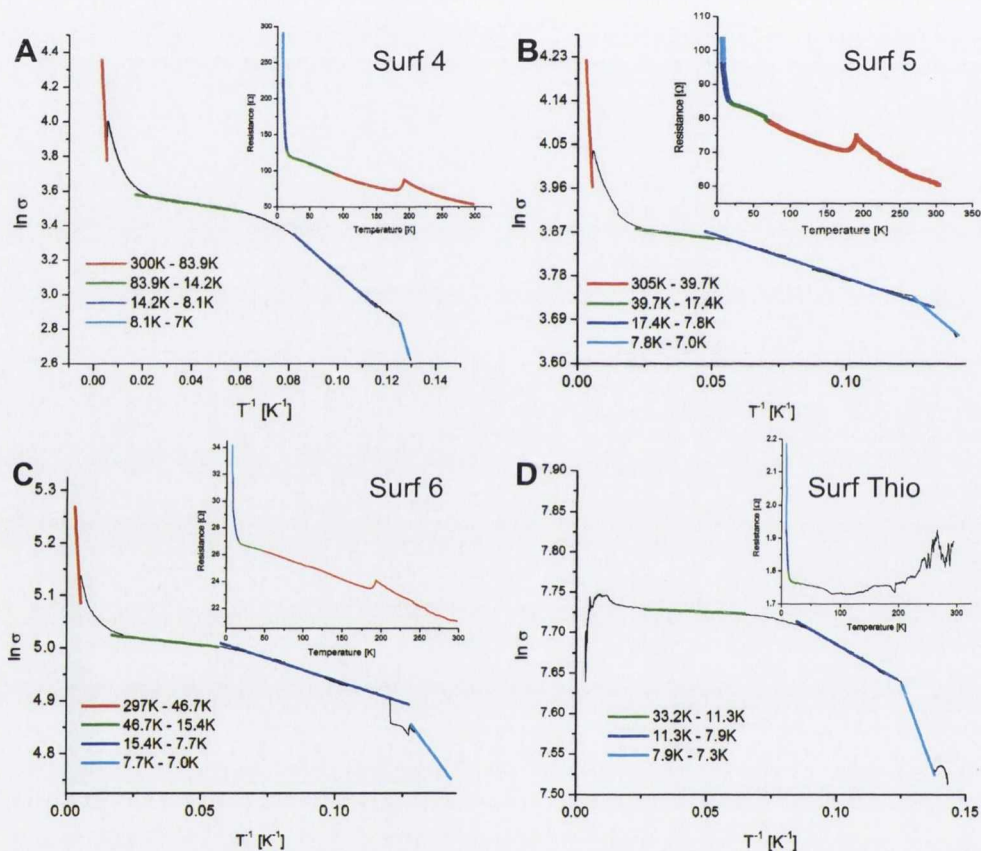


**Figure 8.10:**  $\ln \sigma$  vs  $T^{-1}$  for: **A**;  $\text{surf4}\{\text{Mo}_3\text{Se}_3\}$ , **B**;  $\text{surf5}\{\text{Mo}_3\text{Se}_3\}$ , **C**;  $\text{surf6}\{\text{Mo}_3\text{Se}_3\}$ , **D**;  $\text{surf thio}\{\text{Mo}_3\text{Se}_3\}$ . The colours of the linear plots correspond to the coloured regions of the insets which shows the resistance vs temperature plot. Labels (SurfX etc) refer to  $\text{SurfX}\{\text{Mo}_3\text{Se}_3\}$  in all cases. All measurements carried out under vacuum

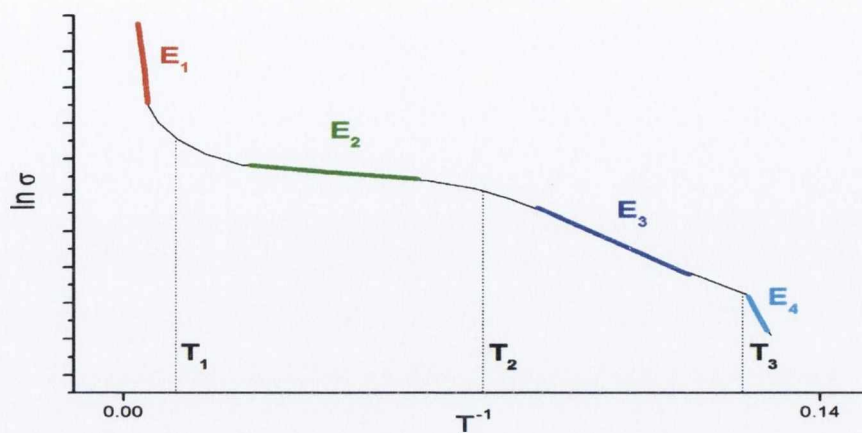


**Figure 8.11:** Representative plot of  $\ln \sigma$  vs.  $T^{-1}$  showing the straight line regions where the barrier energies are calculated and the transition temperatures between these regions (see table 8.3)

| Surf | $E_1$ [eV]            | $T_1$ [K] | $E_2$ [eV]            | $T_2$ [K] | $E_3$ [eV]            | $T_3$ [K] | $E_4$ [eV]            |
|------|-----------------------|-----------|-----------------------|-----------|-----------------------|-----------|-----------------------|
| 3    | $1.603 \cdot 10^{-2}$ | 72        | $1.131 \cdot 10^{-4}$ | 15        | $6.149 \cdot 10^{-4}$ | 8.0       | $4.371 \cdot 10^{-3}$ |
| 4    | $4.597 \cdot 10^{-2}$ | 84        | $3.859 \cdot 10^{-4}$ | 14        | $2.138 \cdot 10^{-3}$ | 8.1       | $8.346 \cdot 10^{-3}$ |
| 5    | $1.803 \cdot 10^{-2}$ | 40        | $1.228 \cdot 10^{-4}$ | 17        | $3.145 \cdot 10^{-4}$ | 7.8       | $7.849 \cdot 10^{-4}$ |
| 6    | $1.332 \cdot 10^{-2}$ | 47        | $9.627 \cdot 10^{-5}$ | 15        | $2.866 \cdot 10^{-4}$ | 7.7       | $1.192 \cdot 10^{-3}$ |
| Thio | n/a                   | 33        | $2.445 \cdot 10^{-5}$ | 11        | $3.182 \cdot 10^{-4}$ | 7.9       | $1.508 \cdot 10^{-3}$ |

**Table 8.3.:** Activation energies for surfactants 3, 4, 5, 6 and thio at each temperature region. Figure 8.11 shows a representative plot of where these regions are located

The shape of the resistance vs. temperature plots for the  $X^+\{Mo_3Se_3\}^-$  samples is generally consistent with the observed R vs. T data obtained for pure  $LiMo_3Se_3$  nanowire bundle (figure 8.4).

The data for Surf3Mo<sub>3</sub>Se<sub>3</sub> (figure 8.9) was fitted to the variable range hopping (VRH) model (equation 8.5) used at the end of section 8.2.2. The data in figure 8.9 ( $\ln \sigma$  vs  $T^{-1}$ ) was replotted as  $\ln \sigma$  vs  $T^{-1/2}$  (1D),  $\ln \sigma$  vs  $T^{-1/3}$  (2D) and  $\ln \sigma$  vs  $T^{-1/4}$  (3D), for the ranges that give straight lines in the  $\ln \sigma$  vs  $T^{-1}$  plot. The findings are summarised in figure 8.12. The description in the legend of each graph is the value of the x-axis for that colour plot. The  $R^2$  values of the linear fits for each data set are displayed on the graph. For 270 – 200 K,  $T^{-1}$  seems to fit best corresponding to thermally activated transport. In the 60 – 20 K range it fits best to  $T^{-1/4}$  (3D). In the 13 – 8 K and 7.8 – 7 K ranges,  $T^{-1/2}$  (1D) behaviour gives the best fit. The trend here indicates that Surf3Mo<sub>3</sub>Se<sub>3</sub> displays thermally activated transport at high temperatures which gives way to a 3D VRH mechanism and ultimately to a 1D VRH mechanism at sub 20 K temperatures.

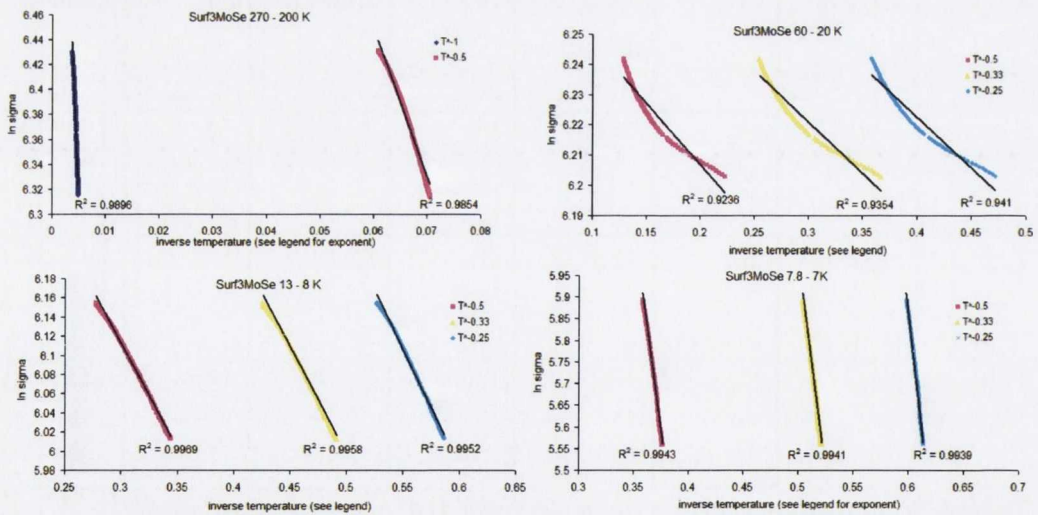


**Figure 8.12:** Surf3MoSe:  $\ln \sigma$  vs  $T^{-1}$  (navy),  $T^{-1/2}$  (magenta),  $T^{-1/3}$  (yellow),  $T^{-1/4}$  (light blue). The temperature ranges are displayed at the top of each plot and the  $R^2$  values each linear fit is displayed beside the trendline

Figure 8.13 shows the activation energy for each  $X^+\{Mo_3Se_3\}^-$  sample plotted against the interwire separation at  $\sim 7K$ . With increasing separation, the activation



energy increases. The exception to this appears to be Surf 5 which may be due to the fact that this is the only surfactant ligand used which does not have a straight chain component and is the most voluminous ligand used.

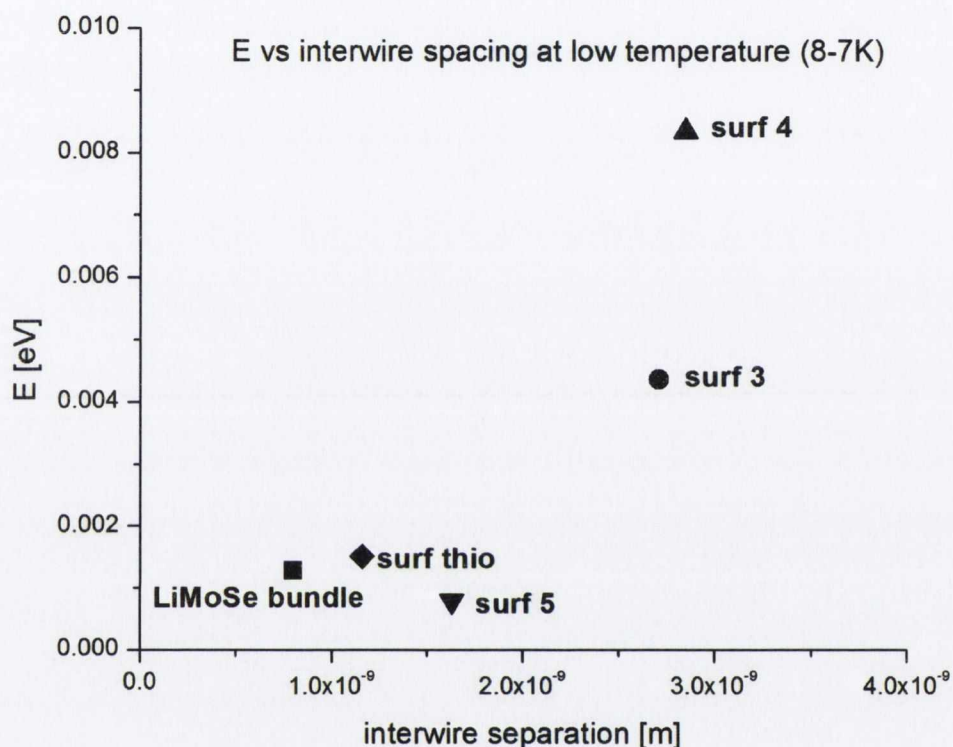


**Figure 8.13:** Activation energy vs interwire separation for LiMoSe bundle and surfX{MoSe} networks at low (< 8 K) temperatures

I-V measurements on each of the ion-exchanged surfactantX{Mo<sub>3</sub>Se<sub>3</sub>} samples were recorded at a variety of temperatures during the cooling cycle. These results are presented in figure 8.14. All I-Vs appear linear throughout the cooling cycles with no indication of a band gap opening over the bias range investigated.

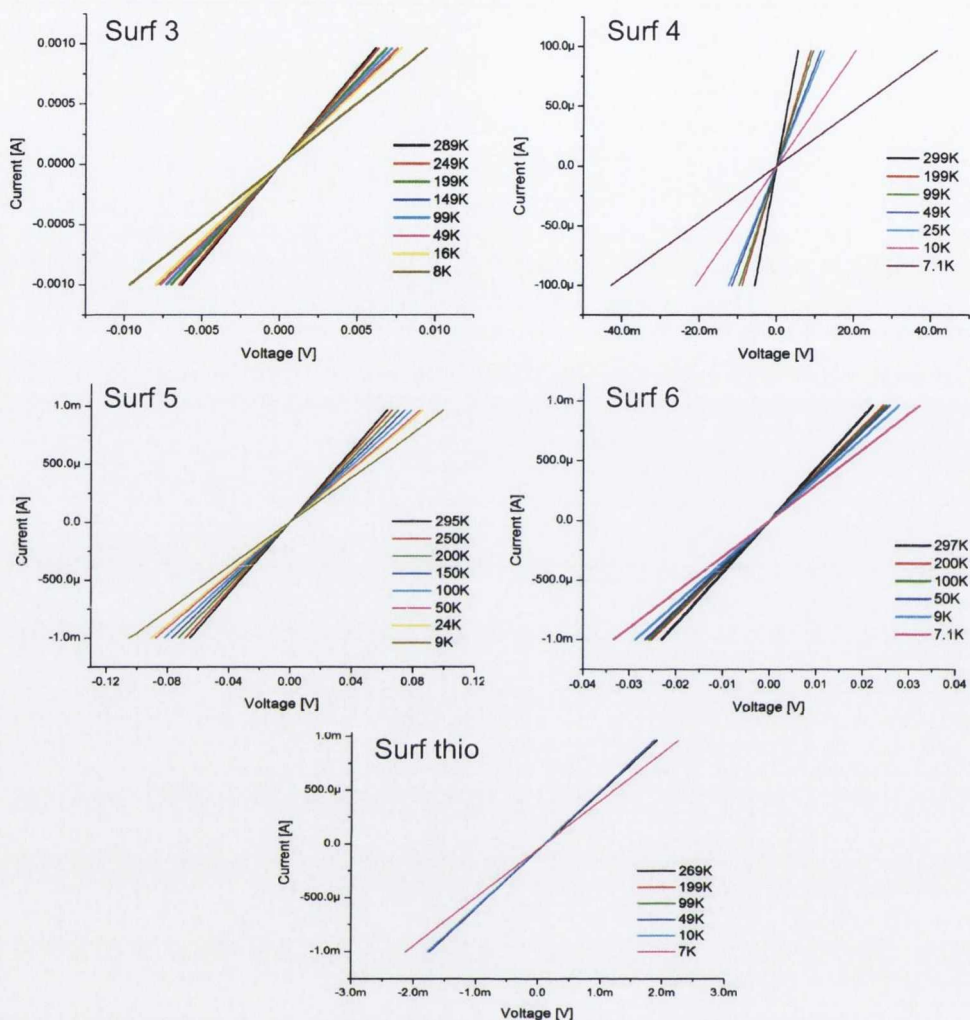


**Figure 8.14:** I-V plots of each of the surfactant  $\{Mo_3Se_3\}$  samples at various temperatures. Labels surf X are shorthand for  $XMoSe$ .

Also of note is the peak that appears in all the surfactant  $\{Mo_3Se_3\}$  R vs. T plots at approximately 192K. Figure 8.15A shows the R vs T plots for all surfX  $\{Mo_3Se_3\}$  samples and the  $LiMo_3Se_3$  bundle normalised on the y-axis. The inset shows a magnified view of the region of the graph about 190 K. Although a Peierls transition in the pure  $LiMo_3Se_3$  phase is unlikely given the fact that a bandgap has not been observed in low temperature STS measurements (Heidelberg[1], down to 85 K, Venkataraman[8] down to 5 K), the presence of the peak at  $\sim 192$  K in all ion-exchanged samples is indicative of Peierls transition behaviour as is the drastic

increase in resistance at low ( $< 25$  K) temperatures. Similar R vs. T behaviour has been noted in the work of Slot et al.[12] on NbSe<sub>3</sub> nanowires, where, at low temperatures, a metallic to insulating transition was observed with decreasing number of NbSe<sub>3</sub> chains in the nanowire. However, unlike that study, the I-V measurements here remain linear over the full temperature range.

Also, the peaks observed here have been observed to move between subsequent measurements (Surf3 {Mo<sub>3</sub>Se<sub>3</sub>}, figure 8.15B), or disappear (Surf4 {Mo<sub>3</sub>Se<sub>3</sub>}, figure 8.15C) indicating this phenomenon may be due to a change within the material, either oxidation resulting in increased resistance values (Surf4 {Mo<sub>3</sub>Se<sub>3</sub>}, figure 8.15C), or perhaps, pumping of any remaining solvent out of the material (Surf3 {Mo<sub>3</sub>Se<sub>3</sub>}, figure 8.15B). During sample preparation, the material is vacuum pumped in the glovebox antechamber (which is pumped on by a scroll pump) whereas the cryostat system utilised a turbo pump system which may draw out more of the solvent.

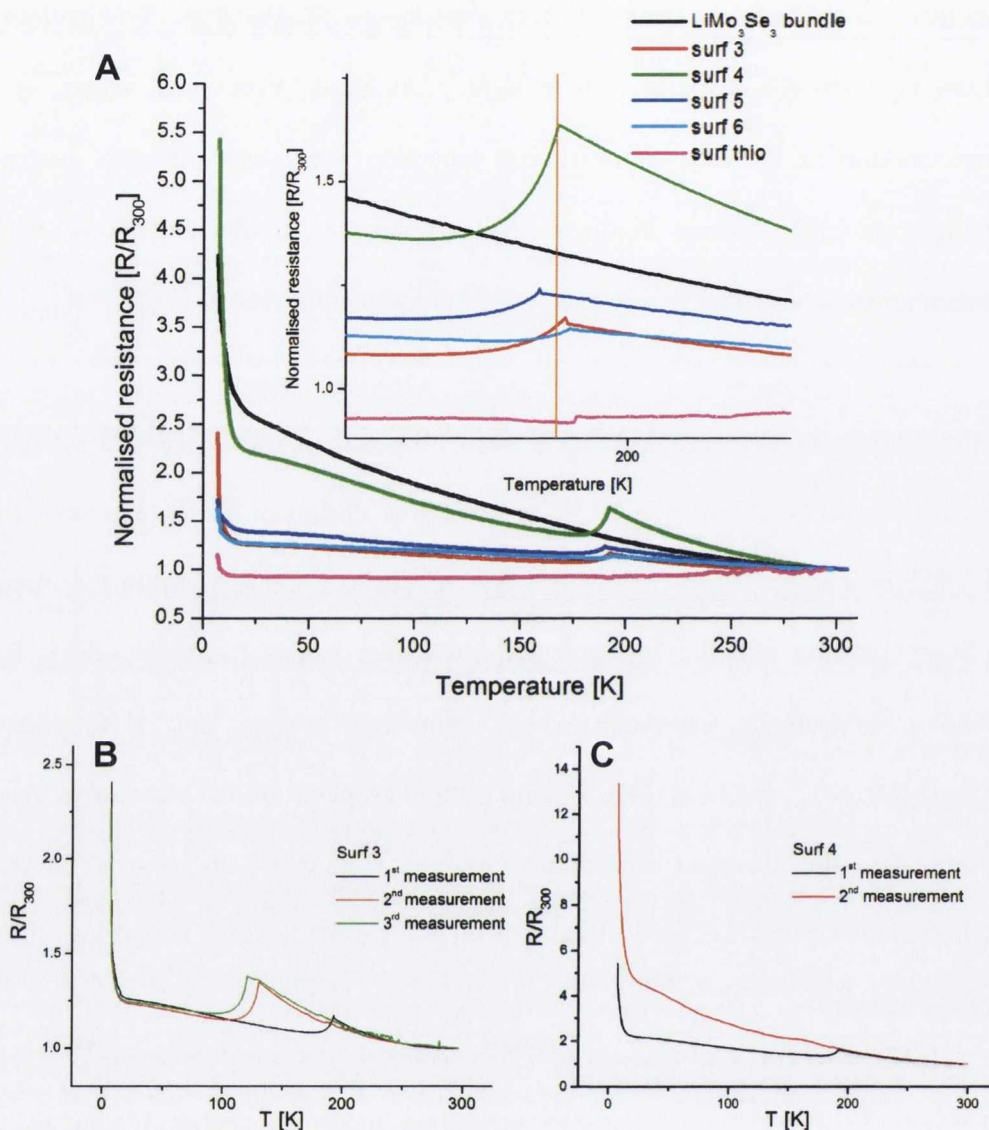


**Figure 8.15:** *A: normalised resistance vs. temperature plots for  $\text{LiMo}_3\text{Se}_3$  bundle and all ion-exchanged samples. Inset shows a close-up of the region about 190K. B and C show subsequent  $R$  vs  $T$  measurements for  $\text{Surf 3}\{\text{Mo}_3\text{Se}_3\}$  and  $\text{Surf 4}\{\text{Mo}_3\text{Se}_3\}$  respectively. In all cases, labels surf  $X$  refer to  $\text{XMo}_3\text{Se}_3$*

### 8.3 Conclusions

Four probe measurements of a  $\text{LiMo}_3\text{Se}_3$  nanowire bundles in air yield a resistivity of  $4.76 \cdot 10^{-5} \Omega\text{m}$ , in good agreement with the literature. As the nanowire bundle oxidised in ambient conditions, the resistance was monitored and the effective (or remaining) conducting core was estimated assuming that the nanowire oxidises from

the outside inwards. A half life of 265.6 hours was obtained. The I-V sweeps of this wire remained linear throughout the course of the oxidation.

Resistance vs. Temperature ( $R(T)$ ) measurements were recorded for a similar nanowire bundle over a range from room temperature to 7 K. The resistivity of the this nanowire bundle was found to be  $9.1 \cdot 10^{-6} \Omega\text{m}$ . The  $R(T)$  data shows a gradual increase in resistance with decreasing temperature to  $\sim 17$  K after which there is a drastic increase in resistance with decreasing temperature. I-V data remained linear over the entire temperature range. Fitting this data to a variable range hopping (VRH) model, it seems the trend would indicate that at higher temperatures the conduction occurs by a 3D VRH mechanism which (at  $< 17$  K temperatures) switches to a 1D VRH system, most likely due to electron localization at low temperatures.

$R(T)$  measurements were also performed on ion-exchanged  $X^+ \{ \text{Mo}_3\text{Se}_3 \}^-$  networks. These display a similar behaviour to the  $R(T)$  data of a pristine  $\text{LiMo}_3\text{Se}_3$  nanowire bundle in that there is a gradual increase in resistance with decreasing temperature until at low ( $< 20$  K) temperatures a drastic increase in resistance with decreasing temperature is noted. Fitting this data to the same VRH model as was used for the pristine  $\text{LiMo}_3\text{Se}_3$  bundles, the trend indicates that  $\text{Surf3Mo}_3\text{Se}_3$  displays thermally activated transport at high temperatures which gives way to a 3D VRH mechanism with decreasing temperature and ultimately to a 1D VRH mechanism at sub 20 K temperatures.

The I-V plots of all the  $X^+\{Mo_3Se_3\}^-$  networks remain linear over all temperatures investigated. Plotting the activation energy at low ( $< 8$  K) temperature vs. observed interwire spacing (from chapter 7) shows that the energy scales well with surfactant used. This is to be expected given that the longer the surfactant used, the greater the interwire separation in these ion-exchanged networks.

## 8.4 References

- [1] A. Heidelberg, H. Bloess, J. W. Schultze, C. J. Booth, E. T. Samulski, J. J. Boland, *Zeitschrift Fur Physikalische Chemie-International Journal of Research in Physical Chemistry & Chemical Physics* **2003**, 217, 573.
- [2] A. Heidelberg, *PhD thesis, Chemistry, Heinrich-Heine University Dusseldorf, Germany* **2004**.
- [3] L. A. Giannuzzi, *Introduction to Focused Ion Beams: Instrumentation, Theory, Techniques and Practice* **2005**, Springer.
- [4] J. M. Tarascon, F. J. DiSalvo, C. H. Chen, P. J. Carroll, M. Walsh, L. Rupp, *Journal of Solid State Chemistry* **1985**, 58, 290.
- [5] J. M. Tarascon, G. W. Hull, F. J. DiSalvo, *Materials Research Bulletin* **1984**, 19, 915.
- [6] J. H. Golden, F. J. Disalvo, J. M. J. Frechet, *Chemistry of Materials* **1995**, 7, 232.
- [7] L. Venkataraman, Y. S. Hong, P. Kim, *Physical Review Letters* **2006**, 96, 76601.
- [8] L. Venkataraman, C. M. Lieber, *Physical Review Letters* **1999**, 83, 5334.
- [9] F. J. RueB, A. P. Micolich, W. Pok, K. E. J. Goh, A. R. Hamilton, M. Y. Simmons, *Applied Physics Letters* **2008**, 92, 052101

- [10] A. N. Aleshin, *Phys. Solid State* **2007**, 49, 2015.
- [11] Apiezon\_Products\_M&I\_Materials, *Technical Data Sheet*,  
<http://www.apiezon.com> **2005**, *APIEZON N cryogenic high vacuum grease*.
- [12] E. Slot, M. A. Holst, H. S. J. van der Zant, S. V. Zaitsev-Zotov, *Physical Review Letters* **2004**, 93, 176602.

## Chapter 9

### Conclusions and Outlook

#### 9.1 Conclusions

Successful synthesis of  $\text{LiMo}_3\text{Se}_3$  (Chapter 3) was confirmed using PXRD and EDX. The ability of the synthesised product to form stable solutions in inert atmospheres also indicated a successful synthesis. The formation of  $\text{X}^+\{\text{Mo}_3\text{Se}_3\}^-$  networks by complexing the  $\text{Li}^+$  ion in solution using a crown-ether and replacing its position on the  $\{\text{Mo}_3\text{Se}_3\}^-$  strand with a positively charged organic ligand.

These  $\text{X}^+\{\text{Mo}_3\text{Se}_3\}^-$  were investigated using STEM and EELS (Chapter 7). The interwire separation was seen to scale well with the estimated physical size of the organic ligand used, in all cases the interwire separation was greater than that of a pristine  $\text{LiMo}_3\text{Se}_3$  nanowire.

$R(T)$  measurements of these  $\text{X}^+\{\text{Mo}_3\text{Se}_3\}^-$  networks show a thermally activated conduction mechanism, in that the measured resistance increases gradually with decreasing temperature until low temperatures ( $\sim 20$  K) where the resistance drastically increases with decreasing temperature. I-V plots of the samples over the entire temperature range remained ohmic. Fitting a variable range hopping model to this data yields a trend that indicates that  $\text{Surf3Mo}_3\text{Se}_3$  displays thermally activated transport at high temperatures which gives way to a 3D VRH mechanism with decreasing temperature and ultimately to a 1D VRH mechanism at sub 20 K



temperatures. The activation energies of the  $X^+ \{Mo_3Se_3\}^-$  networks in the low ( $< 8$  K) temperature region scale well with measured interwire spacing.

Drop or spin casting  $LiMo_3Se_3$  solutions onto substrate surfaces results in crystalline nanowire bundles and 2D nanowire networks. These features can occur side by side and the network is noted to span over the large bundles (chapter 3). High resolution STEM imaging shows that networks are not formed from overlapping nanowires but are rather formed by nanowires splaying out into their constituent  $\{Mo_3Se_3\}^-_{\infty}$  strands which join up with the constituent strands of similar nanowires ultimately forming a  $LiMo_3Se_3$  nanowire “interexchange”. AFM measurements of network junctions on substrate surfaces show no overall height increases through these junctions, further evidence that junctions are not formed from overlapping wires. STEM comparisons of  $LiMo_3Se_3$  crystalline bundles and networks show that the crystalline bundles have interwire separations matching the parent materials (they are “chips off the old block”) while the interwire separation of the networks is slightly larger. EELS comparisons show that the larger crystalline bundles are In “rich”, indicating a quaternary  $In_xLi_{1-x}Mo_3Se_3$  phase. Quenching the nanowire network formation was achieved by rapid vacuum pumping of the solvent upon application to a substrate surface. This resulted in small (100 nm long, 1 nm high) nanowire fragments aligning themselves on a network scaffold.

Chapters 5 and 6 dealt with characterisation of the  $LiMo_3Se_3$  solutions primarily by dynamic light scattering and cryo TEM imaging. The upshot of this work being that filtered  $LiMo_3Se_3$  solutions will always produce network on substrate surfaces regardless of age (assuming they are not exposed to moisture or oxygen) and large

scale networks are not observed in solution. These data indicate that solvent evaporation drives network assembly.

## 9.2 Outlook and Future Work

Future work on this nanowire system might include characterisation of the electrical properties of  $\text{LiMo}_3\text{Se}_3$  nanowire networks, investigation of the mesostructure of the ion-exchanged ( $\text{X}^+(\text{Mo}_3\text{Se}_3)^-$ ) materials and investigation of the effects different surfactant moieties on these ion-exchanged materials.

### 9.2.1 Nanowire Networks

An interesting topic for study would be the conductivity of  $\text{LiMo}_3\text{Se}_3$  networks. An ideal method to examine this is conductive AFM. Firstly, a  $\text{LiMo}_3\text{Se}_3$  network would be deposited on an insulating substrate. Then, as illustrated in figure 9.1(a) (an image from the work of Nirmalraj et al.<sup>[1]</sup>), an electrode would be deposited on top of a section of the nanowire network and a conducting AFM tip used as a mobile electrical nanocontact to examine the electrical characteristics of the network as a function of distance from the deposited electrode. In the case of Nirmalraj et al. networks of single wall carbon nanotubes were studied, however this set up could easily be used to examine networks of  $\text{LiMo}_3\text{Se}_3$ . As junctions within  $\text{LiMo}_3\text{Se}_3$  networks are formed from bundles whose ends splay out and join up with other bundles, one would expect that the voltage drops at these junctions to be less than voltage drops at similarly sized junctions within networks formed of overlying nanowires as there should be a significant contact resistance between the two

overlying nanowires which should not be as pronounced in the case of  $\text{LiMo}_3\text{Se}_3$  nanowire networks.

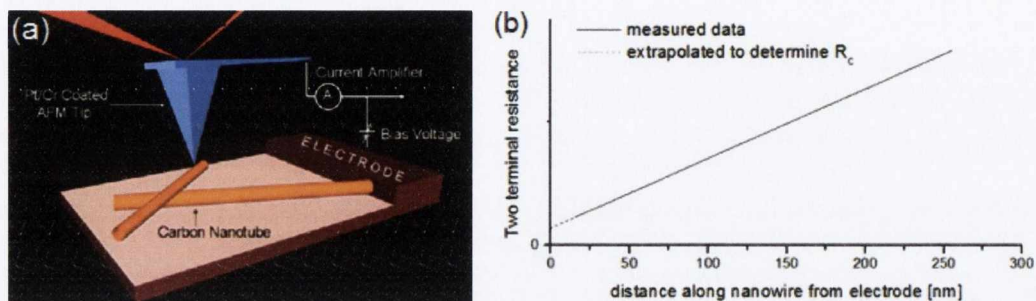


**Figure 9.1** (a) Schematic of conductive AFM being used to examine the electrical properties of a nanowire network (in this case carbon nanotubes. From the work of Nirmalraj et al.[1]) (b) Artificial graph of 2 point resistance vs electrode separation for CAFM measurements along a nanowire. Extrapolating the plot back to the y-axis (dashed line) should yield the contact resistance of the setup.

Another interesting experiment would be to examine the conduction characteristics of a  $\text{LiMo}_3\text{Se}_3$  bundle using the CAFM setup. In this case an isolated  $\text{LiMo}_3\text{Se}_3$  nanowire bundle protruding from a deposited electrode would be examined. As CAFM is a two terminal measurement there will be significant contributions from the contact resistance to the measurement. By plotting the resistance between tip and electrode as a function of distance along the wire from the electrode, the projected intercept of the line with the y-axis (resistance) at a separation of 0 nm should reveal the contact resistance ( $R_c$ ) of the experimental setup (figure 9.1(b)). The plotted line (resistance vs. separation) should remain linear as the separation between the AFM tip and the electrode increases as the resistance ( $R$ ) is directly proportional to the separation between the electrodes ( $l$ ) when the resistivity ( $\rho$ ) and the cross-sectional area ( $A$ ) remain constant.

$$R = \frac{\rho l}{A}$$

However any discrepancy from this linear behaviour would indicate that either the geometry of the nanowire is changing along its length or that the resistivity has changed (most likely due to defects). For the greatest sensitivity a small height  $\text{LiMo}_3\text{Se}_3$  nanowire should be chosen.

### 9.2.2 Ion exchanged $\text{X}^+\{\text{Mo}_3\text{Se}_3\}^-$ materials

As mentioned in this thesis, a major drawback to  $\text{LiMo}_3\text{Se}_3$  is its susceptibility to oxidation and the increase in resistance of the material as a result of this. Messer et al.[2] demonstrated that by complexing the  $\text{Li}^+$  ion in a solution of  $\text{LiMo}_3\text{Se}_3$  using a crown ether, the  $\text{Mo}_3\text{Se}_3$  wires in solution can be coated with a positively charged organic ligand. Heidelberg et al.[3] demonstrated that by using a perfluorinated ligand to replace the Li ion, the corrosion stability (that is, its susceptibility to oxidation) of the material is increased compared to pristine  $\text{LiMo}_3\text{Se}_3$ . In the work presented here the ligands used were investigated in terms of their effect on the interwire separation and the conductivity mechanism of the material. Further work on this material should include a X-ray diffraction (PXR) study of the formed  $\text{X}^+\{\text{Mo}_3\text{Se}_3\}^-$  materials to determine their mesoscopic structure. At low angles, ( $2^\circ - 10^\circ$ ), a hexagonal mesostructure should show peaks such as (100), (110) and (200) and a lamellar mesostructure should show (001) and (002) peaks in the diffraction pattern as was the case for the  $\omega\text{-UTAB}\{\text{Mo}_3\text{Se}_3\}^-$  and  $\text{CTAB}\{\text{Mo}_3\text{Se}_3\}^-$  materials investigated in the work of Messer et al.[2]. Comparing the results from a PXR study to the STEM images presented in this thesis may prove insightful.

In addition to a PXRD study, further experimentation with different surfactant ligands may prove fruitful. In the work presented herein, two pyridinium chloride ligands differed only in the length of the perfluorinated chain attached to the headgroup. A detailed comparison of the length of the perfluorinated alkyl chain (when the same headgroup is used for all ligands) on the corrosion stability of the material would be interesting. A detailed TEM and PXRD study of these materials may also yield information on the degree of interdigitation of these ligands in the ion-exchanged material and on the mesostructure (hexagonal vs. lamellar) of these materials.

### 9.2.3 Outlook

Despite their susceptibility to oxidation  $\text{LiMo}_3\text{Se}_3$  may prove to have useful future applications. There is currently much interest in dispersed 2D nanoparticle arrays for thin film displays. A  $\text{LiMo}_3\text{Se}_3$  nanowire network embedded in a protective transparent layer (to limit the exposure to oxygen) may have possibilities as a transparent electrode for flexible displays, however this would be dependent the nanowire network having a sufficiently high conductivity and sufficiently high optical transmittance.

The group of Osterloh at U.C. Davis have had much success using  $\text{LiMo}_3\text{Se}_3$  as a sensor for a variety of analytes (including methanol, THF, acetonitrile, hexane, DMSO) where the resistance of a  $\text{LiMo}_3\text{Se}_3$  film changed with exposure to these species.[4-6] The proposed mechanism for this chemiresistance is the formation of

break junctions in the material upon exposure to the analyte which causes swelling in the  $\text{LiMo}_3\text{Se}_3$  film. Using an ion exchanged material,  $\text{X}^+\{\text{Mo}_3\text{Se}_3\}^-$ , might prove useful in preparing a sensor which can be used in ambient conditions without concern for the oxidative increase in resistance of the material.

### 9.3 References

- [1] P. N. Nirmalraj, P. E. Lyons, S. De, J. N. Coleman, J. J. Boland, *Nano Letters* **2009**, *9*, 3890.
- [2] B. Messer, J. H. Song, M. Huang, Y. Y. Wu, F. Kim, P. D. Yang, *Advanced Materials* **2000**, *12*, 1526.
- [3] A. Heidelberg, H. Bloess, J. W. Schultze, C. J. Booth, E. T. Samulski, J. J. Boland, *Zeitschrift Fur Physikalische Chemie-International Journal of Research in Physical Chemistry & Chemical Physics* **2003**, *217*, 573.
- [4] X. B. Qi, F. E. Osterloh, *Journal of the American Chemical Society* **2005**, *127*, 7666.
- [5] X. B. Qi, F. E. Osterloh, S. A. Barriga, J. A. Giacomo, S. Chiang, *Analytical Chemistry* **2006**, *78*, 1306.
- [6] X. B. Qi, F. E. Osterloh, J. A. Giacomo, S. Chiang, *Langmuir* **2006**, *22*, 8253.